Carnegie Mellon University

CARNEGIE INSTITUTE OF TECHNOLOGY

THESIS

SUBMITTED IN PARTIAL FULFILLMENT OF THE REQUIREMENTS

FOR THE DEGREE OF Doctor of Philosophy

TITLE Transient Electrohydrodynamics of Low-conductivity Drops

PRESENTED BY Javier Lanauze

ACCEPTED BY THE DEPARTMENT OF

Chemical Engineering

ADITYA KHAIR	4/21/16
ADITYA KHAIR, CO-ADVISOR	DATE
LYNN WALKER	4/2116
LYNN WALKER, CO-ADVISOR	DATE
LORENZ BIEGLER	4/21/16
LORENZ BIEGLER, DEPARTMENT HEAD	DATE

APPROVED BY THE COLLEGE COUNCIL

VIJAYAKUMAR BHAGAVATULA	4/21/16
DEAN	DATE

Transient electrohydrodynamics of low–conductivity drops

Submitted in partial fulfillment
of the requirements for the degree of

Doctor of Philosophy
in
Chemical Engineering

Javier A. Lanauze

B.S. Chemical Engineering
University of Florida

Carnegie Mellon University
Pittsburgh, Pennsylvania

May, 2016

1. Acknowledgments

I am grateful to my thesis advisors Dr. Lynn Walker and Dr. Aditya Khair. Their patience, guidance, enthusiasm, and continued support made the process of working on open–ended research problems pleasing and exciting. Their approach on planning, conducting, and communicating research is one that I hope to practice for the rest of my life. I look forward to conducting research elsewhere using the tools that they helped me develop during my time at Carnegie Mellon. Thanks to Dr. Petia Vlahovska for keeping in touch since we met in 2013; our conversations were enjoyable and valuable to develop some of the work in this thesis, and (hopefully) future work. I thank my thesis committee, composed of Dr. Shelley Anna, Dr. Bob Tilton, and Dr. Steve Garoff, for their useful and insightful comments regarding my thesis proposal and thesis defense.

I would also like to thank Melissa, Sarah, Stephanie, Toni, Chris, Ben, Blake, Anthony, Nick, Rob, Steve, Mike, Charles, and Raj for making the third–floor Complex Fluids office an enjoyable place to work, discuss research, and talk about random topics. In particular, thanks to Ben, Blake, and Anthony for discussions regarding electrokinetics, colloidal stability, and interfacial mechanics throughout the years. Thanks to all of my friends inside and outside of Carnegie Mellon for making Pittsburgh feel like home: my interac-

tions with you helped develop my character and provided balance in my life.

Thanks to my parents Edith Torres and José Lanauze. Your love, support, and dedication make me strive to grow both personally and professionally.

The work in this thesis was supported by the National Science Foundation grant number CBET–1066853.

2. Abstract

Interfaces are subjected to electric fields in a variety of applications. To tune the system in a given application to yield a desired electric–field–induced interfacial response, knowledge of the system timescales and resulting transport at a given set of conditions is advantageous. In this thesis, we consider the time–dependent dynamics of a weakly conducting drop subjected to a uniform DC electric field. The impact is an assessment of the importance of surface charge transport on the ability to predict experimental measurements for drop response under electric fields.

First, we develop a linear theory, valid in the limit of slight drop deformation, in which we account for timescales that quantify transient fluid inertia and transient charging of the interface. We demonstrate that either timescale can yield a nonmonotonic development in the drop shape before reaching steady–state. The theory is extended to model large drop deformation through the boundary integral method. We demonstrate that the fluid charging timescale yields two distinct forms of charge transport: charge relaxation and surface charge convection. These two mechanisms of interfacial charge transport are crucial to determine the transient oblate deformation of an oil drop measured experimentally.

We proceed to quantify the dynamics of a low–conductivity prolate drop upon removal of a uniform DC electric field via computation and experiment. We find that counterintuitively, a large fluid charging timescale yields a fast drop relaxation due to the simultaneous action of the interfacial electrical stress and the capillary stress. Finally, we examine the electric–field–induced breakup of an oil drop containing a colloidal suspension of carbon black particles and varying amounts of surfactant. Depending on the amount of added dispersant, the drop achieves radically different breakup conformations under the applied field.

Contents

List of Figures

List of Tables

3. Introduction

Deformable interfaces under electric fields are of interest in applications including electrospinning,[1] inkjet printing,[2] oil recovery,[3] and cell membrane electroporation.[4] Here, an interface may undergo a variety of dynamics such as deformation, breakup, coalescence, or a change in a given property. To yield a desired electric–field–induced interfacial response, knowledge of the system timescales and resulting transport at a given set of conditions is advantageous.

The field of electrohydrodynamics is concerned with the dynamics of an interface separating low–conductivity fluids under an electric field. For these systems, the applied field animates a flow throughout the drop and medium, which in turn may yield a variety of drop responses such as deformation, breakup, and rotation. We elaborate on the variety of drop dynamics throughout this thesis. Although the field of electrohydrodynamics has recently undergone a fair share of advances,[5–10] we find that significant questions regarding the transient behavior of an isolated low–conductivity drop under a uniform DC electric field remain unanswered. *The objective of this thesis is to quantify the time–dependent response of a weakly conducting ("leaky dielectric") drop exposed to a uniform DC electric field via theory, computation, and experiment.* The impact is an assessment of the importance and influence of surface charge transport on the ability to predict experimental measurements.

3.1 Background

The fluid–fluid systems under electric fields most commonly implemented in applications[1–4] are conductors suspended in insulators (a conductor–insulator system) and insulators suspended in insulators (an insulator–insulator system), respectively. Conductor–insulator systems under electric fields are relevant in processes such as the demulsification of water–in–oil emulsions for enhanced oil recovery;[3] insulator–insulator systems are relevant in processes such as electrospinning of polymeric solutions or melts for the production of thin fibers.[1] For simplicity, we will consider a conducting drop suspended in a dielectric medium as the base case for a conductor–insulator system, and dielectric drop suspended in a dielectric medium as the base case for an insulator–insulator system throughout the rest of this section.

We consider a uniform DC electric field, given by $\boldsymbol{E}_\infty$, applied across a conductor–insulator or insulator–insulator system. When placed under an electric field, the drops pertaining to these two systems will undergo a deformation, which we parametrize by the expression $D = \frac{r_1 - r_2}{r_1 + r_2}$, where r_1 and r_2 denote the semi–axes along and normal to the applied field, respectively (figure 3.1). In spherical coordinates attached to the instantaneous center of the drop, the radial component of the applied electric field is given by $E_{\infty,r} = E_\infty \cos\theta$, where $E_\infty = |\boldsymbol{E}_\infty|$ and θ represents the polar angle measured from the positive z–axis. The stress exerted by the applied field on an interface is obtained by evaluating the jump in electrical stress across the drop surface $[\boldsymbol{\tau}_e \cdot \boldsymbol{n}]$, where $\boldsymbol{\tau}_e$ is the Maxwell stress tensor and $\boldsymbol{n} = \frac{\boldsymbol{r}}{|\boldsymbol{r}|}$ is a unit normal vector that acquires a positive sign when pointing in the positive (outward) direction of the radial coordinate $\boldsymbol{r}$. The radial component of the jump in electrical

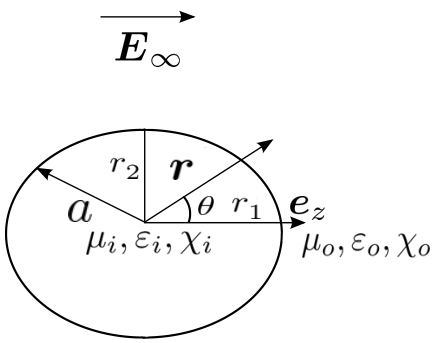

Figure 3.1: Schematic of a drop with permittivity ε_i, resistivity χ_i, and viscosity μ_i suspended in a medium with permittivity ε_o, resistivity χ_o, and viscosity μ_o. A uniform DC electric field, given by $\boldsymbol{E}_\infty$, is applied across the system, which causes the drop to undergo a deformation $D = \frac{r_1 - r_2}{r_1 + r_2}$, where r_1 and r_2 represent the major and minor semi–axes, respectively. In this figure, the drop deformation is along the applied field ($r_1 > r_2$, $D > 0$); i.e. the drop experiences a prolate deformation. Note that $\boldsymbol{e}_z$ is a unit vector in the z–direction (horizontal). Furthermore, θ denotes the polar angle and $\boldsymbol{r}$ denotes the radial position in spherical coordinates.

stress scales quadratically with the radial component of the applied field, i.e. $[\boldsymbol{\tau}_e \cdot \boldsymbol{n}]_r \sim E_{\infty,r}^2 \sim E_\infty^2 \cos^2\theta$. This entails that the normal electrical stress will attain a maximum at the poles of the drop, located at $\theta = 0$ and $\theta = \pi$. These stresses are balanced by the capillary stress $\gamma \nabla_s \cdot \boldsymbol{n}$, and the induced drop deformation will be along the applied field ($r_1 > r_2$): the drop undergoes a prolate deformation. Here, γ denotes the interfacial tension and ∇_s denotes the surface gradient operator.

In 1962, Allan and Mason derived expressions for the steady–state deformation attained by a conducting drop and a dielectric drop exposed to a uniform DC electric field.[11] For a conducting drop suspended in a dielectric medium, the expressions reads

$$D_{\text{conductor}} = \frac{9}{16} Ca_o. \tag{3.1}$$

For a dielectric drop suspended in a dielectric medium, the steady field–

induced deformation is given by

$$D_{\text{dielectric}} = \frac{9}{16}\frac{(S-1)^2}{(S+2)^2}\,Ca_o. \tag{3.2}$$

Here, $Ca_o = \varepsilon_o E_\infty^2 a/\gamma$ is the electric capillary number based on the medium properties. This dimensionless group represents a ratio of electrical stress, which scales as $\varepsilon_o E_\infty^2$, to capillary stress, which scales as γ/a. Note that the subscripts i and o are implemented to distinguish the drop (inner phase, i) from the medium (outer phase, o). Furthermore, ε is the electric permittivity, a is the radius of a spherical drop, and the dimensionless parameter $S = \varepsilon_i/\varepsilon_o$. Equation (3.1) and (3.2) require the following assumptions:

1. The bulk fluid phases are electrically neutral.

2. The normal interfacial electrical stress is balanced by the capillary stress.

Since the electric field is irrotational, it may be expressed as the gradient of a scalar electrostatic potential ϕ. The first assumption conveniently reduces Gauss's law from Poisson's equation $\nabla^2\phi = \rho_e$ to Laplace's equation $\nabla^2\phi = 0$ for the drop and medium, where ρ_e is the volumetric free charge density. Furthermore, the second assumption eliminates the need to solve a momentum balance to obtain the resulting drop deformation under the applied electric field. Equations (3.1) and (3.2) were derived in the limit of $Ca_o \ll 1$, in which the drop is slightly perturbed away from its spherical equilibrium shape and the deformation scales linearly with the capillary number; i.e. $D \sim Ca_o$. These two expressions are only capable of predicting slight prolate deformations ($r_1 > r_2$, $D > 0$). When comparing the theoretical predictions (3.1) and (3.2) against experimental measurements, Allan and Mason confirmed the field–induced prolate deformation of a conducing drop. However a surprising result was encountered for dielectric drops: deformations normal to the

electric field, oblate deformations ($r_1 < r_2$, $D < 0$), were measured for some of the systems examined.[11] This observation was puzzling at the time, since none of the existing theory[11,12] was capable of predicting the oblate deformations measured in some experiments.

Since the existing theory at the time did not require solving a momentum balance or predict any fluid flow at steady–state, it is often referred to as an *electrohydrostatic* theory. To understand the missing link that will yield a qualitative prediction of the unexpected oblate deformations measured experimentally, we examine the jump in tangential electrical stress across the drop surface $[\boldsymbol{\tau}_e \cdot \boldsymbol{n}]_t = q\boldsymbol{E}_t$. Here, q denotes the amount of free charge per unit area of the drop, $\boldsymbol{E}_t = (\boldsymbol{E} \cdot \boldsymbol{t})\,\boldsymbol{t}$ denotes the tangential component of the electric field evaluated at the interface, and $\boldsymbol{t}$ denotes a unit tangent vector that is positive when pointing in the positive θ–direction along the interface. If one considers a conducting drop suspended in a dielectric medium under an electric field, any free charge throughout the conducting phase will distribute itself throughout the drop surface in such a way that the interfacial electric field is purely normal: $\boldsymbol{E}_t = 0$ yields $[\boldsymbol{\tau}_e \cdot \boldsymbol{n}]_t = 0$. Furthermore, if one considers a dielectric drop suspended in a dielectric medium under an electric field, no free charge is expected to reside throughout the drop, medium, and interface: $q = 0$ yields $[\boldsymbol{\tau}_e \cdot \boldsymbol{n}]_t = 0$. Thus, it seems that the tangential electrical stress is continuous across the drop surface. Moreover, $q = 0$ yields a continuous electric displacement across the interface $[\varepsilon E_n] = 0$, where $E_n = \boldsymbol{E} \cdot \boldsymbol{n}$ denotes the normal component of the electric field evaluated at the interface.

In 1966, G.I. Taylor published a seminal manuscript[13] in which he extended the existing *electrohydrostatic* theory for a dielectric drop suspended in a di-

electric medium. His main insight was the following: although the bulk fluid phases are expected to remain electroneutral, a finite amount of charge will reach the interface under the action of an applied electric field. Thus, the drop and medium are not perfect insulators, but rather weak conductors. The nonzero surface charge q gives rise to a jump in the interfacial tangential electrical stress $[\boldsymbol{\tau}_e \cdot \boldsymbol{n}]_t = q\boldsymbol{E}_t$. These shear electrical stresses are balanced by shear viscous stresses, and fluid flow is induced inside of the drop and throughout the medium. Here, assumption 1 still allows implementation of the solution to Laplace's equation to quantify the interfacial stresses exerted by the electric field. However, assumption 2 breaks down, as a solution to a momentum balance is now required to calculate the resulting drop deformation; Taylor solved the Stokes equations (of inertialess flow) for the drop and medium. Furthermore, the boundary conditions applied at the drop surface must be modified to impose a continuity in current across the interface $[\frac{1}{\chi}E_n] = 0$, and a tangential stress balance between electrical and viscous stresses $[\boldsymbol{\tau}_e \cdot \boldsymbol{n}]_t + [\boldsymbol{\tau}_h \cdot \boldsymbol{n}]_t = 0$. Note that χ represents the electrical resistivity and $\boldsymbol{\tau}_h$ represents the hydrodynamic stress tensor. Taylor derived the following expression for the linear deformation of a weakly conducting drop under a uniform DC electric field:

$$D_{\text{Taylor}} = \frac{9}{16(2R+1)^2}\left[\frac{3R(3M+2)(1-SR)}{5(M+1)} + R^2(1-2S) + 1\right] Ca_o, \quad (3.3)$$

where $R = \chi_i/\chi_o$, $M = \mu_i/\mu_o$, and μ is the fluid viscosity, respectively. This expression was able to predict both the prolate and oblate drop deformations measured in the experiments of Allan and Mason.[11] Furthermore, since Taylor's theory predicts steady–state recirculating toroidal flows inside and outside of the drop, it is often referred to as an *electrohydrodynamic* theory. The mathematical model Taylor followed to arrive to equation (3.3) is known

as the "leaky dielectric model."[13–15] Despite the very low, $O(10^{-10}\,\mathrm{S/m})$, conductivity of many systems, mainly composed of oils, there is no such thing as a perfect dielectric fluid–fluid system; impurities such as trace amounts of water will always induce charge at the interface, and a weak or strong fluid flow will arise in conjunction with a prolate or oblate drop deformation. These field–induced flows, which help drive a prolate or oblate drop deformation depending on the material properties of each phase, is a unique feature of low–conductivity fluids under electric fields.

Taylor's model[13] has proven to be successful in predicting the slight field–induced drop deformation and direction of fluid flow for experimental systems characterized by different sets of dimensionless parameters $\{S, M, R\}$.[16–18] However, despite the fact that many studies have implemented Taylor's approach in quantifying the deformation of low–conductivity drops under electric fields, the interpretation of the surface charge density q has remained ambiguous. Recently, an article addressing this issue was published by Schnitzer and Yariv.[10] By employing a matched asymptotic analysis valid in the limit of thin Debye length and strong electric field, they successfully derived Taylor's model from the more fundamental electrokinetic (Poisson–Nernst–Planck) equations. The physical interpretation of the surface charge q is as follows: when a weakly conductive drop is placed in a weakly conductive medium, ions will adsorb to the interface even in the absence of an applied field. This adsorbed charge is screened by diffuse layers of counterions at either side of the drop surface; a triple–layer structure forms at the interface. The action of the electric field on this triple layer perturbs it and gives rise to an apparent local charge per unit area q (figure 3.2). Thus, q is not confined to the genuine interface, but rather encompasses the ions adsorbed to the interface and corresponding screening

layers once the field is applied. This perturbed triple layer gives rise to the dominant interfacial tangential electrical stresses and resulting toroidal fluid flow predicted by Taylor.[13] Although Schnitzer and Yariv's model[10] predicts electrophoretic drop motion under a uniform DC electric field, this effect is small compared to the dynamics that result from the apparent surface charge density q. Remarkably, Taylor's model, which was published 50 years ago, captures the essential field–induced response of low–conductivity systems without requiring the explicit modeling of transport of ionic species: it is considered a "lumped parameter" model. We make use of Taylor's coarse–grained interpretation of the interfacial charge q throughout the work presented in this thesis.

3.2 Structure of thesis

In chapter 4, we develop a linear, $O(Ca)$ theory to describe the transient electrohydrodynamic deformation of a drop upon application of an electric field. Previous analytical work has suggested that the capillary timescale $\tau_c = \mu a/\gamma$ is the only relevant timescale required to correctly quantify the slight field–induced transient deformation of a low–conductivity drop.[19] Here, the drop acquires its final deformation in a monotonic fashion, which may be modeled by a simple exponential decay in time that yields Taylor's expression (3.3) at steady–state; $D(t) = D_{\text{Taylor}}\left(1 - e^{-\frac{t}{\tau_c}}\right)$. In this chapter, we account for two additional fluid timescales: first, we account for a timescale for diffusion of momentum throughout the drop and medium $\tau_m = a^2\rho/\mu$, where ρ denotes the fluid density. This leads to the consideration of transient (or linear) fluid inertia via the unsteady Stokes equations. Furthermore, we account for an electrical relaxation time $\tau_e = \varepsilon\chi$ over which the drop interface charges. The temporal drop deformation is governed by two dimensionless groups: (i)

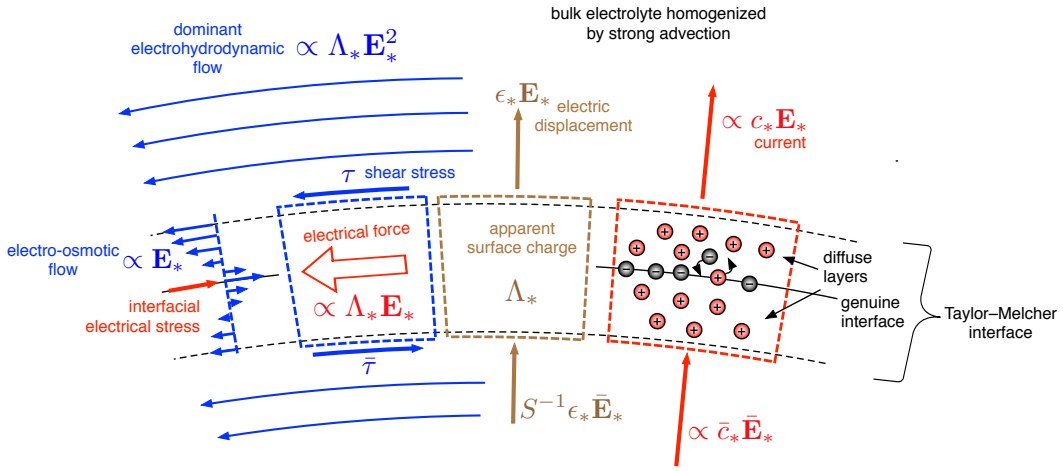

Figure 3.2: Electrokinetic interpretation of the surface charge density q (image extracted from Schnitzer and Yariv[10]). Ions adsorb to the interface in the absence of a uniform applied field; they are screened by diffuse layers at either side of the drop surface. When the electric field is applied, the triple–layer structure, which is composed of the adsorbed charge and corresponding screening layers, locally deviates from electroneutrality. This gives rise to an apparent charge per unit area q (Λ_* in this figure), as predicted by Taylor,[13] which is responsible for animating the dominant tangential electrical stress that drives a flow which scales quadratically with the applied field. Although there is a local electroosmotic flow at the drop surface, it is counteracted by an electrical stress exerted at the genuine interface. This results in electrophoretic drop migration that is asymptotically small compared the the strong tangential fluid flow driven by the apparent surface charge q. In this figure, the subscripts $*$ are implemented to denote a dimensional quantity and the overbars are implemented to denote a variable that corresponds to the drop phase. Furthermore, E_* is the local electric field, ϵ_* is the electric permittivity, and c_* is the ionic concentration.

the ratio of capillary to momentum diffusion timescales: an Ohnesorge number Oh; and (ii) the ratio of charge relaxation to momentum diffusion timescales, which we denote by a Saville number[15] Sa. If charge and momentum relaxation occur quickly compared to interface deformation, $Sa \ll 1$ and $Oh \gg 1$ for the drop and medium, and a monotonic deformation is acquired. In contrast, $Sa > 1$ and $Oh < 1$ for either phase can lead to a non–monotonic development in the deformation. The drop and medium behave as perfect dielectrics at early times, which always favors an initial prolate (parallel to the applied field) deformation. As a consequence, for a final oblate (normal to the applied field) deformation, there is a shape transition from prolate to oblate at intermediate times. This transition is caused by the accumulation of sufficient charge at the interface to generate electrical and viscous shear stresses. Notably, after the transition, there may be an "overshoot" in the deformation, i.e. the magnitude exceeds its steady–state value, which is proceeded by an algebraic tail describing the arrival towards the final, steady deformation. Our work demonstrates that transient inertia or the electrical relaxation time can yield nonmonotonic electrohydrodynamic drop deformation in the linear regime, which has not been shown previously in the literature. This chapter has been published as an article in the Physics of Fluids journal.

In chapter 5, we extend the theory developed in chapter 4, and compute the the transient deformation of a leaky dielectric drop under a uniform DC electric field via an axisymmetric boundary integral method, which accounts for surface charge convection and transient charging of the drop interface. The boundary integral method enables the computation of large drop deformation. The effect of surface charge convection is quantified through an electric Reynolds number[14] Re, which represents a ratio of the interfacial charging

timescale τ_e to a flow timescale $\tau_f = a/U$, where U is a characteristic flow strength. The effect of transient charging of the drop surface is quantified through the previously–defined Saville number[15] Sa, which in this chapter represents a ratio of the electrical relaxation timescale τ_e to the capillary timescale τ_c. We focus on drops that attain an ultimate oblate (major axis normal to the applied field) steady–state configuration. The computations predict that as the timescale for interfacial charging increases, a shape transition from prolate deformation (major axis parallel to the applied field) to oblate deformation occurs at intermediate times due to the slow buildup of charge at the surface of the drop. Convection of surface charge towards the equator of the drop is shown to weaken the steady–state oblate deformation. Additionally, convection results in sharp, shock–like variations in surface charge density near the equator of the drop. Our numerical results are then compared with an experimental system consisting of a millimeter–sized silicone oil drop suspended in castor oil. Agreement in the transient deformation is observed between our numerical results and experimental measurements for moderate electric field strengths. This suggests that both charge relaxation and charge convection are required, in general, to quantify the time–dependent deformation of leaky dielectric drops. Importantly, accurate prediction of the observed modest deformation requires a nonlinear model. Discrepancies between our numerical calculations and experimental results arise as the field strength is increased. We believe that this is due to the observed onset of rotation and three–dimensional flow at such high electric fields in the experiments,[17,18] which an axisymmetric boundary integral formulation naturally cannot capture. This work is the first to examine the effect of surface charge transport on the transient deformation of a low–conductivity drop via comparison between computation and experiment. This chapter has been published

as an article in the Journal of Fluid Mechanics.

In chapter 6, we quantify the dynamics of a prolate leaky dielectric drop upon removal of a uniform DC electric field. Experiments consisting of a castor oil drop suspended in silicone oil are compared against axisymmetric boundary integral computations that account for transient charging, or charge relaxation, of the interface. A temporal asymmetry between the drop deformation and relaxation processes is observed in the experiments and computations: the drop relaxes back to its spherical equilibrium shape faster than the time taken to achieve its steady–state deformation. During the deformation process, the electrical (Maxwell) stress deforms the drop along the direction of the applied field; it is counteracted by the capillary stress. During the relaxation process, i.e. after the field is removed, the electrical stress now acts together with the capillary stress to quickly restore the drop back to equilibrium. This change in action of the electrical stress is responsible for the asymmetry between the drop deformation and relaxation. Notably, the electrical stress acts over the charge relaxation timescales of the fluids: thus, counterintuitively, longer charging timescales yield faster drop relaxation. That is, the longer it takes for the interface to discharge, the faster the drop shape relaxes. We also present computational results for a drop that does not relax back to its initial spherical shape upon removal of the electric field; rather, the drop breaks up via an end–pinching mechanism.[20] This work is the first to quantify the relaxation of a low–conductivity drop upon removal of an applied electric field. This chapter has been accepted for publication in the Physical Review Fluids journal.

In chapter 7, we examine the breakup of an oil drop containing a colloidal

suspension of carbon black particles under a uniform DC electric field. A drop of squalane containing a fixed concentration 3.3 g/L of carbon black particles and varying amounts of polyisobutylene succinimide surfactant (OLOA) is exposed to a field strength $E_\infty = 2.5\,\mathrm{kV/cm}$ that yields drop breakup. When the concentration of OLOA is appreciable (30 parts OLOA per 100 parts carbon black, pph OLOA), the drop exhibits breakup via the formation of bulbous ends. Here, the added dispersant stabilizes the colloidal suspension of carbon black particles, which yields homogeneous field–induced drop breakup at this applied field strength. When the concentration of surfactant is decreased to a value of 2 pph OLOA, the suspension becomes unstable within the timescale of the experiment, and achieves breakup via the formation of lobes that turn into fingers and eventually disintegrate. Furthermore, we find that the stable 30 pph system may be destabilized at a higher field strength $E_\infty = 5.3\,\mathrm{kV/cm}$, which we believe is due to the direct action of the electric field on the colloidal suspension. The experimental systems in this study are modeled using the boundary integral method, which assumes that both the drop and medium phases are homogeneous. We implement our computations to assess the importance of surface charge transport and the heterogeneity of the particle–loaded drop. The method depicted in this chapter may be implemented to deduce the colloidal stability of drops containing particles.

4. The influence of inertia and charge relaxation on electrohydrodynamic drop deformation

4.1 Introduction

We restate Taylor's expression[13,14] for the final, steady–state slight drop deformation D_T achieved under a weak applied electric field of magnitude E_∞, given as

$$D_T \equiv \frac{r_1^* - r_2^*}{r_1^* + r_2^*} = \frac{9}{16(R+2)^2}\,\Phi_T\,Ca_i, \tag{4.1}$$

where

$$\Phi_T = \frac{3(2M+3)(SR-1)}{5(M+1)} + S(R^2+1) - 2. \tag{4.2}$$

In (4.1) and (4.2), $S = \varepsilon_o/\varepsilon_i$, $M = \mu_o/\mu_i$, and $R = \chi_o/\chi_i$, are the permittivitiy (ε), viscosity (μ), and resistivity (χ) ratios of the outer fluid (subscript o) to that of the droplet (subscript i). The electric capillary number $Ca_i = \varepsilon_i E_\infty^2 a/\gamma$ represents a ratio of electrical stress $\varepsilon_i E_\infty^2$ to capillary stress γ/a, where γ is the interfacial tension between the two liquids, and a is the radius of the un-

deformed droplet. Finally, r_1^* and r_2^* denote the semi-axes along and normal to the applied field, respectively (figure 4.1). The superscript $*$ is used to represent a dimensional variable; dimensional material properties and characteristic process time scales contain no superscript. Taylor's theory requires Ca_i to be small so that the deformation is slight and linear in Ca_i. The steady shape of the deformed drop is determined by the sign of Taylor's so-called discriminating function Φ_T.[13,14] A positive Φ_T represents a prolate deformation ($r_1^* > r_2^*$), while $\Phi_T < 0$ represents an oblate deformation ($r_1^* < r_2^*$). Note that this is the only chapter in which we implement Taylor's notation to conduct our analysis and nondimensionalization in terms of the inner fluid (drop) variables.

Although steady electrohydrodynamic droplet deformation is relatively well-understood[15] for two Newtonian liquids with a clean interface, the manner in which this steady-state is attained has received continued attention. Recent numerical studies that employ the Navier-Stokes equations have presented an "overshoot" (i.e., the magnitude of the deformation exceeds its final value) in the transient deformation of leaky dielectric drops exposed to DC fields, which can display oscillations before settling to the steady-state value. For example, Supeene *et al.*[21] accounted for charge convection at the interface and used the finite element method with a moving mesh to obtain numerical values for deformation versus time. Fernández *et al.*[22] considered the deformation of an emulsion of multiple drops and used a front-tracking – finite volume technique to solve the momentum balance. Before presenting their main results, they performed a sample calculation for a single oblate droplet. These two works presented an overshoot in the deformation profile. Moreover, Haywood *et al.*[23] used the finite volume method with an adaptive grid to study liquid – liquid and liquid – air systems. Despite the fact that these were combina-

tions of perfect conductors and insulators, they reported an overshoot for a liquid – air system (corresponding to a dielectric drop and medium), which they claimed was due to fluid inertia. Paknemat *et al.*[24] also analyzed the response of conducting and perfectly insulating droplets in dielectric media, and leaky dielectric droplets in weakly conductive media. They used the level set method together with the ghost fluid method to calculate drop deformation and breakup under a DC electric field. To check that their calculated deformation converged to known analytical results for dielectric drops exposed to weak fields,[11] they performed a grid resolution test which displayed an overshoot before arriving to the steady (prolate) deformation. These last two studies describing perfect conductive and dielectric droplet response suggest that steady-state fluid recirculation is not necessary for an overshoot to manifest itself. In addition, overshoots can sometimes take on relatively large values, such as that presented in figure 6 of Supeene *et al.*,[21] which depicts a normalized transient deformation profile for a dielectric droplet. Here, an overshoot that is approximately 1.4 times the steady value is observed, which is followed by a decaying oscillation before the steady deformation is attained.

Analytical models have also been developed to describe the transient deformation of perfectly conducting[23,25] droplets subjected to DC fields, and weakly conducting droplets subjected to DC[19] and AC[26] fields. (The latter of which also contains an oscillatory component in the total deformation.) Aside from Nishiwaki *et al.*,[26] these studies have assumed instantaneous interfacial charging, and all have made use of the quasi-steady Stokes equations. For example, Esmaeeli and Sharifi[19] considered a leaky dielectric droplet and medium under a suddenly-applied DC field. They obtained the following expression for the

deformation:

$$D_{ES}(t) = D_T \left(1 - e^{-t^*/\tau}\right), \tag{4.3}$$

where D_T is the steady deformation (4.1), t^* denotes time, and τ is a characteristic capillary time scale (equation 23 in their paper). Equation (4.3) monotonically settles towards Taylor's classic result as $t^* \to \infty$. This result is clearly unable to predict an overshoot as observed in the numerical works of Supeene *et al.*[21] and Fernández *et al.*[22] for leaky dielectrics. A goal of the present work is to resolve this discrepancy and determine under which conditions an overshoot occurs.

As we shall show, the appearance of an overshoot is linked to the value of a particular dimensionless group: the Ohnesorge number $Oh_{i,o} = \mu_{i,o}/\sqrt{\gamma a \rho_{i,o}}$, where $\mu_{i,o}$ and $\rho_{i,o}$ represent the viscosity and density of either phase, respectively. This equality defines Oh as a material property, which can acquire a wide range of values in practice. This parameter evaluates the importance of transient fluid inertia: when it is considerably less than unity, the overshoot is most apparent. Not surprisingly, the plots generated by Supeene *et al.*[21] and Fernández *et al.*[22] displayed an overshoot when $Oh_{i,o} \approx 0.2$. Additionally, the work by Paknemat *et al.*[24] depicted an overshoot when $Oh_{i,o} \approx 0.02$, while Haywood *et al.*[23] reported an overshoot when $Oh_i = 1.37 \times 10^{-3}$ and $Oh_o \approx 7.8 \times 10^{-4}$. Haywood *et al.*[23] also compared numerical results for a liquid – liquid system with an analytical model that assumed quasi-steady Stokes flow: the two displayed a monotonic deformation for various Oh_i greater than unity, although there was a lag in the deformation predicted by numerics when $Oh_i = 2$ and $Oh_o = 0.2$. The analytical quasi-steady Stokes flow models[19,23,25,26] that predict monotonic deformation profiles effectively assume that $Oh_{i,o} \to \infty$; that is, the flow is established instantaneously on the timescale

that the interface deforms.

Sozou[27] first explored the validity of neglecting inertial terms in the momentum balance when describing the deformation of a droplet exposed to an AC electric field. Specifically, Sozou retained only the linear inertial term $\rho\,\partial \boldsymbol{u}^*/\partial t^*$, where $\boldsymbol{u}^*$ denotes the fluid velocity, as opposed to Torza *et al.*,[28] who assumed a quasi-steady flow. Retaining this term was found to yield results substantially different from Torza *et al.*[28] when the time scale for momentum diffusion of either phase $a^2/\nu_{i,o}$ was the same order of magnitude as the reciprocal of the frequency of oscillation ω (here, $\nu_{i,o} = \mu_{i,o}/\rho_{i,o}$ is a kinematic viscosity). Notably, taking the limit $\omega \to \infty$ provided a time-dependent deformation and fluid velocity profiles with a frequency dependence different from that obtained by Torza *et al*. Souzou also considered the development of deformation and flow for a leaky dielectric droplet in response to a suddenly-applied, uniform DC field.[29] Sozou solved the unsteady Stokes equations via Laplace transforms, although only few numerical values for the deformation throughout time were reported, all of which suggest a monotonic development towards the steady-state (i.e., no overshoot). Our work re-examines the transient deformation of a drop under a uniform DC field. The technical approach accounting for fluid inertia via the unsteady Stokes equations is analogous to Sozou.[29] However, unlike Sozou, we consider the electric field to not be established instantaneously, in which case the charging of the interface must be accounted for. Two recent analytical works that have accounted for finite electrical relaxation times are those of Xu[30] and Zhang *et al.*[31] Zhang *et al.* employed prolate spherical coordinates to describe the large unsteady deformation of a weakly conductive droplet, while Xu solved for the interfacial flow field in the small-deformation regime for a leaky dielectric drop. However,

both of these studies neglect fluid inertia. Therefore, unlike Sozou,[29] Xu,[30] and Zhang *et al.*,[31] we consider the influence of both charge relaxation and momentum diffusion.[21] The ratio of charge relaxation to momentum diffusion time scales may acquire an $O(1)$ number in practice, as discussed by Saville;[14,15] we label the ratio of these time scales as Sa. The parameters Oh and Sa dictate the transient deformation; the former determines the appearance (or absence) of an overshoot, and the latter may provide a prolate-oblate shape transition preceding the overshoot. Asymptotic approximations for the deformation at early and late times are derived, which are bridged by the numerical inversion of an analytical result for the deformation obtained in the Laplace domain. Finally, we discuss under which conditions the neglect of transient fluid inertia and interfacial charging are valid.

4.2 Problem formulation and solution

A droplet is suspended in a weakly conductive medium with differing viscosity, permittivity, and resistivity (figure 4.1). A uniform DC electric field is suddenly imposed around the drop, which causes it to deform due to the mismatch in electrical permittivity and resistivity between the two phases. We consider a slight spheroidal deformation of the surface (small capillary number). This permits treatment of the drop as spherical during the implementation of boundary conditions,[19] and ultimately results in Taylor's expression (4.1) once the steady-state is reached. Hence, spherical coordinates are employed, and the symmetry axis is taken along the applied field.

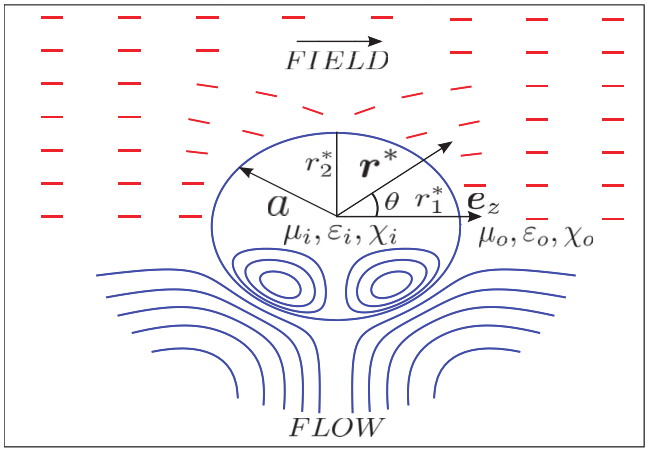

Figure 4.1: Definition sketch for electrohydrodynamic drop deformation. Prolate droplet of radius a, viscosity μ_i, permittivity ε_i, and resistivity χ_i suspended in a medium with viscosity, permittivity, and resistivity μ_o, ε_o, and χ_o, respectively. The upper half depicts electric field lines, while the lower half displays fluid streamlines. Both are symmetric with respect to the equator of the drop ($\theta = \pi/2$), and are also axisymmetric about the applied field. For clarity, field lines are omitted from the top half of the drop. The major and minor semi-axes r_1^* and r_2^* are also shown. Here, $\boldsymbol{r}^*$ denotes the position vector, while $\boldsymbol{e}_z$ and θ represent a unit vector in the direction along the applied field and the polar angle, respectively.

The electric field is expressed as the gradient of a scalar electrostatic potential ϕ^*. Due to the negligible amount of net free charge density, the potential satisfies Laplace's equation inside and outside of the droplet,

$$\nabla^{*2}\phi_{i,o}^* = 0. \tag{4.4}$$

The inner potential ϕ_i^* is bounded at the origin, and the outer field $-\nabla^*\phi_o^*$ approaches the applied field $E_\infty \boldsymbol{e}_z$ at large distances from the drop. The

boundary conditions at the surface of the droplet $r^* = \sqrt{\boldsymbol{r}^* \cdot \boldsymbol{r}^*} = a$ are:

$$\phi_i^* = \phi_o^* \tag{4.5}$$

and

$$[-\varepsilon \, \nabla^* \phi^* \cdot \boldsymbol{n}] = q^*(t^*, \theta), \tag{4.6}$$

respectively, where the square brackets in (4.6) denote a difference between the outer and inner quantities, and $\boldsymbol{n}$ is a normal vector which points in the positive (outwards) radial direction. Equation (4.5) represents the continuity of potential, while (4.6) accounts for a surface charge density $q^*(t^*, \theta)$ that causes a jump in the electric displacement. Since $q^*(t^*, \theta)$ is an unknown time-dependent quantity, we seek an additional equation describing the Ohmic transport of charge to the interface, which may be expressed as[14,15]

$$\left[\frac{1}{\chi} \, \nabla^* \phi^* \cdot \boldsymbol{n}\right] = \frac{\partial q^*}{\partial t^*}, \tag{4.7}$$

where we have neglected surface charge convection[30,31] (see Appendix B for justification). Taking the Laplace transform of (4.6) and (4.7), eliminating the transform of $q^*(t^*, \theta)$, and imposing an initially uncharged interface, $q^*(0, \theta) = 0$, provides the more useful boundary condition

$$\frac{\partial \widetilde{\phi}_i^*}{\partial r^*}(1 + Sa_i \, \tau_{m,i} \, s^*) = \frac{\partial \widetilde{\phi}_o^*}{\partial r^*} \left(\frac{1}{R} + Sa_i \, S \, \tau_{m,i} \, s^*\right), \tag{4.8}$$

where $\widetilde{\phi}_{i,o}^*(r^*, \theta, s^*)$ represents the Laplace transform of $\phi_{i,o}^*(r^*, \theta, t^*)$, i.e., $\widetilde{\phi}_{i,o}^* = \int_0^\infty e^{-s^* t^*} \phi_{i,o}^* \, dt^*$. Here, $Sa_i = \varepsilon_i \chi_i \nu_i / a^2 = \tau_{e,i} / \tau_{m,i}$ is a dimensionless quantity introduced by Saville,[15] $\nu_i = \mu_i / \rho_i$ is the kinematic viscosity of the droplet, and $\tau_{e,i} = \varepsilon_i \chi_i$ and $\tau_{m,i} = a^2 / \nu_i$ represent the characteristic time scales for charge relaxation and diffusion of momentum within the drop, respectively.

The retainment of the terms that multiply Sa_i in (4.8) indicates that the electrical relaxation time may take on finite values. That is, the electric field is not established instantaneously, and the surface charge $q^*(t^*, \theta)$ accumulates at the interface to give rise to tangential electrical stresses. The remaining steps to solve for the potentials are implemented in the Laplace domain and are presented in Appendix A. After inversion back to the time domain, the tangential and radial jump in electrical stress at the interface are given by

$$\begin{aligned}[\boldsymbol{\tau}_e^* \cdot \boldsymbol{n}]_\theta &= \frac{\varepsilon_i E_\infty^2}{(R+2)^2(2S+1)}\Bigg[9(RS-1)\left(e^{-\frac{R+2}{Sa_i R(2S+1)}\frac{t^*}{\tau_{m,i}}}-1\right) \\ &\quad \times\left((RS-1)e^{-\frac{R+2}{Sa_i R(2S+1)}\frac{t^*}{\tau_{m,i}}}+2S+1\right)\Bigg]\sin\theta\cos\theta \qquad (4.9)\end{aligned}$$

and

$$\begin{aligned}[\boldsymbol{\tau}_e^* \cdot \boldsymbol{n}]_r &= -\frac{9\,\varepsilon_i E_\infty^2}{2(R+2)^2(2S+1)^2}\Bigg[-\frac{1}{2}(RS-1)^2\Big((5S-2)\cos 2\theta+3S\Big)e^{-\frac{2R+4}{Sa_i R(2S+1)}\frac{t^*}{\tau_{m,i}}} \\ &\quad +2(2S+1)(RS-1)\Big((2RS+1)\cos^2\theta+(S-1)\sin^2\theta\Big)e^{-\frac{R+2}{Sa_i R(2S+1)}\frac{t^*}{\tau_{m,i}}} \\ &\quad +(2S+1)^2\Big(-(R^2S-1)\cos^2\theta+(S-1)\sin^2\theta\Big)\Bigg], \qquad (4.10)\end{aligned}$$

respectively, where the subscripts r and θ represent the normal and tangential components of the jump in stress, $\boldsymbol{\tau}_e^* = \varepsilon\left(\nabla^*\phi^*\nabla^*\phi^* - \frac{1}{2}\nabla^*\phi^*\cdot\nabla^*\phi^*\,\boldsymbol{I}\right)$ is the Maxwell stress tensor, and $\boldsymbol{I}$ is the identity tensor.

The electrical shear stress (4.9) is balanced by viscous forces for the drop to remain in mechanical equilibrium; this entails fluid flow. The Navier-Stokes equations (NSE) inside and outside of the droplet are

$$\rho_{i,o}\left(\frac{\partial \boldsymbol{u}_{i,o}^*}{\partial t^*}+\boldsymbol{u}_{i,o}^*\cdot\nabla^*\boldsymbol{u}_{i,o}^*\right)=-\nabla^* p_{i,o}^*+\mu_{i,o}\nabla^{*2}\boldsymbol{u}_{i,o}^* \qquad \text{and} \qquad \nabla^*\cdot\boldsymbol{u}_{i,o}^*=0, \qquad (4.11)$$

where $\rho_{i,o}$, $\boldsymbol{u}^*_{i,o}$, and $p^*_{i,o}$ denote the density, velocity, and pressure within the drop and medium, as appropriate. The two phases are assumed to be density-matched ($\rho_i = \rho_o$) so that sedimentation is negligible. Balancing electrical stress $\varepsilon_i E_\infty^2$ and viscous stress $\mu_i U/a$ inside the drop yields the velocity scale $U \sim \varepsilon_i E_\infty^2 a/\mu_i$. The pressure is normalized by the inner electrical stress $\varepsilon_i E_\infty^2$. We non-dimensionalize time with the characteristic time for momentum diffusion within the droplet $\tau_{m,i} = a^2/\nu_i$, and distance with the radius of the undeformed drop a. These scalings lead to the dimensionless NSE,

$$\frac{\partial \boldsymbol{u}_{i,o}}{\partial t} + Re_i\, \boldsymbol{u}_{i,o} \cdot \nabla \boldsymbol{u}_{i,o} = -\nabla p_{i,o} + \alpha\, \nabla^2 \boldsymbol{u}_{i,o} \qquad \text{and} \qquad \nabla \cdot \boldsymbol{u}_{i,o} = 0, \quad (4.12)$$

where the lack of superscripts represents a dimensionless variable, and the constant $\alpha = 1$ for the inner phase, while $\alpha = M = \mu_o/\mu_i$ for the outer phase. Here, $Re_i = \rho_i U a\,/\mu_i = \rho_i \varepsilon_i E_\infty^2 a^2/\mu_i^2$ is the Reynolds number based on the drop. As the model to be derived will describe low-Reynolds-number flows, we neglect the convective inertial term in (4.12). Thus, we obtain the unsteady Stokes equations for both fluids,

$$\frac{\partial \boldsymbol{u}_{i,o}}{\partial t} = -\nabla p_{i,o} + \alpha\, \nabla^2 \boldsymbol{u}_{i,o} \qquad \text{and} \qquad \nabla \cdot \boldsymbol{u}_{i,o} = 0. \quad (4.13)$$

Note that normalizing time by $\tau_{m,i}$ automatically preserves the transient inertial contribution in (4.13). Symmetry permits the use of a stream function ψ that automatically satisfies the incompressibility constraint in (4.13), such that[32]

$$\boldsymbol{u}_{i,o} = \nabla \wedge \left[\frac{\psi_{i,o}(r,\theta,t)\boldsymbol{e}_\phi}{r \sin\theta} \right], \quad (4.14)$$

where $\boldsymbol{e}_\phi$ is a unit vector in the azimuthal direction. To solve for $\psi_{i,o}$, we choose the angular form needed to balance the tangential electrical stress in

(4.9), which is

$$\psi_{i,o}(r,\theta,t) = f_{1(i,o)}(r,t)\sin^2\theta\cos\theta. \tag{4.15}$$

Similarly, to match the normal electrical stress (4.10), the pressure takes the form

$$p_{i,o}(r,\theta,t) = f_{2(i,o)}(r,t)(1-3\cos^2\theta). \tag{4.16}$$

Since the flow is unsteady, the functions $f_{1(i,o)}(r,t)$ and $f_{2(i,o)}(r,t)$ depend on distance r and time t. There are four unknown functions in (4.15) and (4.16): $f_{1,i}(r,t)$, $f_{1,o}(r,t)$, $f_{2,i}(r,t)$, and $f_{2,o}(r,t)$; the radial and angular components of (4.13) provide four equations, yielding a well-posed system. Taking the Laplace transform of (4.13) – (4.16), substituting (4.14) into (4.13), using (4.15) and (4.16), and eliminating the transform of $f_{2(i,o)}$ leads to the following ordinary differential equation (ODE):

$$\alpha r^4\frac{d^4\widetilde{f}_{1(i,o)}(r,s)}{dr^4}-(sr^4+12\alpha r^2)\frac{d^2\widetilde{f}_{1(i,o)}(r,s)}{dr^2}+24\alpha r\frac{d\widetilde{f}_{1(i,o)}(r,s)}{dr}+6sr^2\widetilde{f}_{1(i,o)}(r,s)=0, \tag{4.17}$$

where $\widetilde{f}_{1(i,o)}(r,s)$ indicates the dimensionless Laplace transform of $f_{1(i,o)}(r,t)$. As $\widetilde{f}_{2(i,o)}(r,s)$ was eliminated to arrive at (4.17), an expression for it may be written in terms of $\widetilde{f}_{1(i,o)}(r,s)$ as

$$\widetilde{f}_{2(i,o)}(r,s) = \frac{s}{6}\frac{d\widetilde{f}_{1(i,o)}(r,s)}{dr}+\frac{\alpha}{6}\left[-\frac{d^3\widetilde{f}_{1(i,o)}(r,s)}{dr^3}+\frac{6}{r^2}\frac{d\widetilde{f}_{1(i,o)}(r,s)}{dr}-\frac{12}{r^3}\widetilde{f}_{1(i,o)}(r,s)\right]. \tag{4.18}$$

The general solution to (4.17) is

$$\begin{aligned}\widetilde{f}_{1(i,o)}(r,s) &= c_{(1,5)}\,r^3+\frac{c_{(2,6)}}{r^2}+c_{(3,7)}\,e^{r\sqrt{\frac{s}{\alpha}}}\left(s-\frac{3\sqrt{\alpha s}}{r}+\frac{3\alpha}{r^2}\right)\\ &\quad +c_{(4,8)}\,e^{-r\sqrt{\frac{s}{\alpha}}}\left(s+\frac{3\sqrt{\alpha s}}{r}+\frac{3\alpha}{r^2}\right),\end{aligned} \tag{4.19}$$

where c_1 through c_8 are functions of s. To reiterate, this expression applies for both the droplet and medium, thereby yielding a total of eight integration constants.

We now proceed to find solutions for $\widetilde{f}_{1(i,o)}$ that are well-behaved throughout the domain of interest. First, the stream function $\psi_i(r,\theta,t)$ must vanish at the origin $r = 0$. Additionally, $\psi_o(r,\theta,t)$ must approach a spatially independent (yet possibly time-dependent) value as $r \to \infty$. The implementation of these conditions is discussed in detail in Appendix C, which eliminates four of the integration constants in (4.19). The solution of (4.19) inside of the drop is then

$$\widetilde{f}_{1,i}(r,s) = C_1 r^3 + C_2 \sqrt{r}\, I_{\frac{5}{2}}(r\sqrt{s}), \tag{4.20}$$

and outside of the droplet,

$$\widetilde{f}_{1,o}(r,s) = \frac{C_3}{r^2} + C_4 \sqrt{r}\, K_{\frac{5}{2}}\left(r\sqrt{\frac{s}{M}}\right), \tag{4.21}$$

where

$$I_{\frac{5}{2}}(x) = \frac{1}{\sqrt{2\pi x}}\left[e^x\left(1 - \frac{3}{x} + \frac{3}{x^2}\right) - e^{-x}\left(1 + \frac{3}{x} + \frac{3}{x^2}\right)\right] \tag{4.22}$$

and

$$K_{\frac{5}{2}}(x) = \sqrt{\frac{\pi}{2x}}\; e^{-x}\left(1 + \frac{3}{x} + \frac{3}{x^2}\right) \tag{4.23}$$

are modified Bessel functions of order $\frac{5}{2}$, $C_1 = c_1$, $C_2 = c_3\, s^{\frac{5}{4}}\sqrt{2\pi}$, $C_3 = c_6$, and $C_4 = c_8\, s^{\frac{5}{4}}\sqrt{2}\Big/ M^{\frac{1}{4}}\sqrt{\pi}$. Note that (4.20) and (4.21) were presented in dimensional form by Sozou[29] (equations (19) and (20) in that paper). To determine $C_1 - C_4$, the subsequent interfacial boundary conditions are applied at $r = 1$:

$$u_{\theta,i} = u_{\theta,o}, \tag{4.24}$$

$$u_{r,i} = u_{r,o} = \frac{1}{Re_i}\frac{\partial \xi}{\partial t}, \tag{4.25}$$

$$[\boldsymbol{\tau}_e \cdot \boldsymbol{n}]_\theta + [\boldsymbol{\tau}_h \cdot \boldsymbol{n}]_\theta = 0, \tag{4.26}$$

and

$$[\boldsymbol{\tau}_e \cdot \boldsymbol{n}]_r + [\boldsymbol{\tau}_h \cdot \boldsymbol{n}]_r = \frac{1}{Ca_i}\nabla \cdot \boldsymbol{n}, \tag{4.27}$$

where $u_{r(i,o)}$ and $u_{\theta(i,o)}$ denote the radial and tangential velocities, respectively, and $\boldsymbol{\tau}_h = -p\boldsymbol{I} + \mu\left[\nabla \boldsymbol{u} + (\nabla \boldsymbol{u})^T\right]$ is the hydrodynamic stress tensor. Equation (4.24) represents the no-slip condition, while (4.25) represents the no-flux condition, with $\xi(t,\theta)$ as the instantaneous material surface of the drop. Finally, the balance between electrical and hydrodynamic shear stresses is imposed through (4.26), while (4.27) balances the jump in electrical and hydrodynamic normal stresses with the interfacial stress that the droplet exerts to resist deviation from a spherical shape. At small field strengths, $Ca_i \ll 1$, the drop is only slightly distorted. Hence, we may write $\xi(t,\theta) = 1 + \frac{2}{3}D(t)(3\cos^2\theta - 1)$,[19] where $D(t)$ is a time-dependent deformation. Furthermore, we let

$$D(t) = \frac{\Phi(t)}{8}\,Ca_i, \tag{4.28}$$

where $\Phi(t)$ is a time-dependent discriminating parameter, whose sign will determine the droplet configuration (prolate versus oblate) at all times, and may be computed by collecting the terms that multiply $\cos^2\theta$ in the normal stress balance (4.27). This assumes that the only mode of deformation that evolves is that which results in Taylor's steady deformation (4.1) as $t \to \infty$. That is, we do not allow for higher order modes that grow and then ultimately decay to zero as $t \to \infty$. Inserting the expression for the surface $\xi(t,\theta)$ and (4.28)

into (4.25) yields

$$u_{r,i} = u_{r,o} = \frac{1}{12}\frac{Ca_i}{Re_i}\frac{d\Phi(t)}{dt}(3\cos^2\theta - 1), \tag{4.29}$$

where the ratio Ca_i/Re_i is the square of an Ohnesorge number based on the drop properties $Oh_i = \mu_i/\sqrt{\gamma a \rho_i}$ (recall $\rho_i = \rho_o$ in our analysis). This expression may be recast as $Oh_i = \sqrt{\tau_{c,i}/\tau_{m,i}}$, where $\tau_{c,i} = \mu_i a/\gamma$ is a characteristic time scale for droplet relaxation due to capillary forces, which is related to the capillary time scale τ in (4.3) of Esmaeeli and Sharifi.[19] As $Oh_i \to \infty$, this capillary time-scale dictates the dynamics as the flow is established in a quasi-steady manner. The Laplace transforms of (4.15) and (4.16) (using (4.14)) are substituted into the transforms of (4.24), (4.26), and (4.29) to obtain the following expressions that relate the unknown functions $\widetilde{f}_{1,i}(r,s)$ and $\widetilde{f}_{1,o}(r,s)$ ((4.20) and (4.21)):

$$\frac{d\widetilde{f}_{1,i}(1,s)}{dr} = \frac{d\widetilde{f}_{1,o}(1,s)}{dr}, \tag{4.30}$$

$$\widetilde{f}_{1,i}(1,s) = \widetilde{f}_{1,o}(1,s) = \frac{Oh_i^2}{12}\, s\, \widetilde{\Phi}(s), \tag{4.31}$$

and

$$\frac{d^2\widetilde{f}_{1,i}(1,s)}{dr^2} - 2\frac{d\widetilde{f}_{1,i}(1,s)}{dr} + 6\widetilde{f}_{1,i}(1,s) - M\left[\frac{d^2\widetilde{f}_{1,o}(1,s)}{dr^2} - 2\frac{d\widetilde{f}_{1,o}(1,s)}{dr} + 6\widetilde{f}_{1,o}(1,s)\right]$$
$$-\frac{9(RS-1)(Sa_iRSs+2)}{s\Big[Sa_iRs(2S+1)+R+2\Big]\Big[Sa_iRs(2S+1)+2R+4\Big]} = 0, \tag{4.32}$$

where

$$
\begin{aligned}
\widetilde{\Phi}(s) \;=\; & -6\frac{d\widetilde{f}_{1,i}(1,s)}{dr} + 12\widetilde{f}_{1,i}(1,s) - M\left[-6\frac{d\widetilde{f}_{1,o}(1,s)}{dr} + 12\widetilde{f}_{1,o}(1,s)\right] \\
& -3\left[\frac{s}{6}\frac{d\widetilde{f}_{1,i}(1,s)}{dr} + \frac{1}{6}\left(-\frac{d^3\widetilde{f}_{1,i}(1,s)}{dr^3} + 6\frac{d\widetilde{f}_{1,i}(1,s)}{dr} - 12\widetilde{f}_{1,i}(1,s)\right)\right] \\
& +3\left[\frac{s}{6}\frac{d\widetilde{f}_{1,o}(1,s)}{dr} + \frac{M}{6}\left(-\frac{d^3\widetilde{f}_{1,o}(1,s)}{dr^3} + 6\frac{d\widetilde{f}_{1,o}(1,s)}{dr} - 12\widetilde{f}_{1,o}(1,s)\right)\right] \\
& +\frac{9}{2s(2S+1)\Big[Sa_iRs(2S+1)+R+2\Big]\Big[Sa_iRs(2S+1)+2R+4\Big]} \\
& \times\Bigg[S\Bigg(R^2\Bigg(Sa_is\Big(Sa_is(2S+1)(S-1)^2+S(S+2)+3\Big)+4S+2\Bigg) \\
& +2Sa_iRs\Big(S(3S-5)-1\Big)+4S-6\Bigg)-4\Bigg], \qquad (4.33)
\end{aligned}
$$

and $\widetilde{\Phi}(s)$ indicates the Laplace transform of the discriminating function $\Phi(t)$. Substituting $\widetilde{f}_{1,i}$ and $\widetilde{f}_{1,o}$ from (4.20) and (4.21) indicates that the only unknowns in (4.30) – (4.33) are $C_1 - C_4$, which are solved for analytically.

4.3 Results

To obtain the time-dependent deformation $D(t)$, the expressions for $f_{1,i}(1,t)$ and $f_{1,o}(1,t)$ are required. We perform the necessary calculations in the Laplace domain and solve for the unknown constants $C_1 - C_4$ in (4.20) and (4.21). These constants are too lengthy to present here; however, Mathematica files with expressions for $C_1 - C_4$ are available upon request. It is then straightforward to calculate the Laplace transform of the deformation (4.28) through the expression for $\widetilde{\Phi}(s)$ in (4.33). The initial rest condition $D(t=0) = 0$ is imposed, and the Laplace-space deformation $\widetilde{D}(s)$ is inverted numerically via an open source Laplace-inversion program.[33] The final expression for the deformation in the Laplace domain is in Appendix D (A24). Validation of

(A24) is presented in Appendix E. Expanding $\widetilde{D}(s)$ about $s = 0$ and $s \to \infty$ offers useful insight into the physics at late and early times, respectively. An expansion about $s = 0$ yields

$$\widetilde{D}(s) = \frac{D_T}{s} + \beta + \gamma\, Ca_i \sqrt{s} + O(s^{\frac{3}{2}}), \tag{4.34}$$

where the first term is Taylor's steady deformation D_T divided by s, and β and γ are time-independent constants, which depend on the ratios S, M, and R, and are presented in Appendix D. Inverting (4.34) gives

$$D(t) = D_T + \beta\, \delta(t) - \gamma\, \frac{Ca_i}{2\sqrt{\pi}}\, \frac{1}{t^{\frac{3}{2}}} + O\left(\frac{1}{t^{\frac{5}{2}}}\right), \tag{4.35}$$

where $\delta(t)$ is the Dirac-delta function centered at zero. Since (4.35) considers late times, the second term $\beta\, \delta(t)$ in this series may be discarded. Thus, the drop approaches its steady deformation with a long-time (algebraic) tail, scaling as $t^{-\frac{3}{2}}$. This should be contrasted against (4.3), which neglects fluid inertia and charge relaxation, and predicts that the steady deformation D_T is approached with an exponentially-decaying transient. Retaining transient inertia predicts the long-time behavior presented in (4.35) – a slower approach towards the steady deformation. The algebraic tail in (4.35) is reminiscent of the problem of an initially stationary solid sphere in a fluid medium under a suddenly imposed force.[34] There, retaining linear inertia in the momentum balance predicts an approach towards the steady-state particle velocity with an algebraic tail scaling as $t^{-\frac{1}{2}}$,[34] whereas the quasi-steady Stokes equations again suggest an exponentially decaying transient at large times.

An expansion of $\widetilde{D}(s)$ about $s \to \infty$ yields

$$\widetilde{D}(s) = \epsilon \frac{Ca_i}{Oh_i^2} \frac{1}{s^3} + \eta \frac{Ca_i}{Oh_i^2} \frac{1}{s^{\frac{7}{2}}} + O\left(\frac{1}{s^4}\right), \tag{4.36}$$

where ϵ and η are constants listed in Appendix D. The inversion of (4.36) shows that at small times,

$$D(t) = \epsilon \frac{1}{2} \frac{Ca_i}{Oh_i^2} t^2 + \eta \frac{8}{15\sqrt{\pi}} \frac{Ca_i}{Oh_i^2} t^{\frac{5}{2}} + O(t^3). \tag{4.37}$$

A Taylor expansion of (4.3) gives $D_{ES} = D_T\, t/\tau + O(t^2)$ for $t \ll 1$. Clearly, (4.37) depicts a slower deformation, an early-time lag, as it shows a t^2 dependence as opposed to a linear dependence in time. We now present results that quantify the deformation $D(t)$ at times that bridge the early and late-time asymptotics presented previously.

A case in which the medium is much more viscous than the drop is considered first. Material properties as well as values for pertinent dimensionless groups are listed in table 4.1. Many of these parameters were acquired from the experimental work of other researchers, which considered a castor oil-silicone oil system.[18,35] The droplet radius was chosen within sizes normally generated in experiments,[18] while the viscosities are reasonable values for oils. The quantities S, M, and R yield a final oblate droplet configuration.

Phase	ε_r	$1/\chi$ (S/m)	μ (Pa s)	ρ (kg/m^3)	a (mm)	γ (mN/m)
drop	3.0	1.2×10^{-12}	0.0484	960		
					4.0	3.2
medium	5.3	4.5×10^{-11}	0.4840	960		

Phase	Ca	Re	Oh	Sa	S	M	R
drop	0.001	0.005	0.4	68.0			
					1.8	10.0	0.03
medium	0.002	9.3×10^{-5}	4.4	32.8			

Table 4.1: First set of parameters for a droplet suspended in a weakly conductive medium. The top section of the table displays properties for the drop and medium, while the bottom section lists pertinent dimensionless groups. Here, ε_r is the relative permittivity.

Note that Re_i and Re_o, and Ca_i and Ca_o are small compared to unity, which justifies the use of the unsteady Stokes equations and a first-order expansion of the droplet surface about equilibrium. The Ohnesorge number Oh of the outer phase is greater than unity, while the converse holds for the drop. Recall that Oh_i appeared naturally within the scaled interfacial boundary condition (4.29) as $Oh_i^2 = Ca_i/Re_i = \mu_i^2/\gamma a \rho_i$. The second equality defines Oh_i as a material property, which can acquire a wide range of values in experimental systems. One can, in principle, always decrease the electric field strength E_∞ to comply with $Re_{i,o} \ll 1$ and $Ca_{i,o} \ll 1$, as these are proportional to E_∞^2, while $Oh_{i,o}$ takes on $O(1)$ (or less) values, independent of E_∞. In fact, $Oh < 1$ is readily achievable in experiments.[36,37] The dimensionless group that measures the relative time scales of charge to momentum relaxation, Sa, is much greater than unity for both phases. A comparison between the deformation calculated from the inversion of the exact expression (A24) in Appendix D and the deformation obtained by employing the quasi-steady Stokes equations with instantaneous charging of the interface[19] (4.3) is shown in figure 4.2(a). The deformation profile $D(t)$ from the inversion of (A24) is negative (prolate) when normalized by D_T for $t\nu_i/a^2 \lesssim 1$,[21] crosses the origin at $t\nu_i/a^2 \approx 1.12$, and

then monotonically reaches the steady-state oblate deformation (4.1). The development of this curve also displays a significant lag compared to (4.3), which is caused by transient charging of the interface, and, to a lesser extent, diffusion of momentum throughout both fluids. The numerical inversion of (A24) is shown together with the asymptotic expansions about $t = 0$ and $t \to \infty$, (4.35) and (4.37), respectively, in figure 4.2(b), showing good agreement at late and early times.

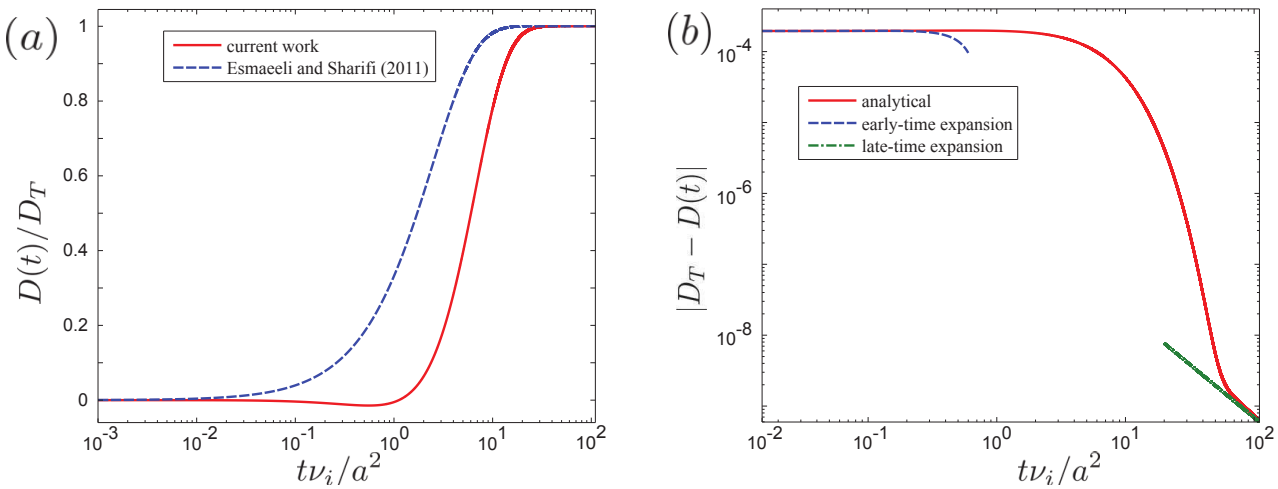

Figure 4.2: (a) Normalized transient deformation of a droplet for parameters listed in table 4.1. The solid curve (red online) is the inversion of (A24), which considers transient inertia and charge relaxation of both fluids, while the dashed curve (blue online) corresponds to (4.3) from Esmaeeli and Sharifi's work,[19] which assumes quasi-steady Stokes flow and instantaneous interfacial charging. The solid curve initially acquires negative ordinate values, which represents a prolate configuration. After this, the deformation profile crosses the origin and monotonically arrives at (4.1), substantially lagging (4.3). (b) Inversion of (A24) together with early- and late-time asymptotics (4.35) and (4.37), respectively.

Based on the literature reviewed in the Introduction, one may expect to

observe the retainment of transient inertia to result in an overshoot in the deformation profile. Recall the definition of the Ohnesorge number $Oh_{i,o} = \sqrt{\tau_{c(i,o)}/\tau_{m(i,o)}}$, where $\tau_{c(i,o)} = \mu_{i,o}a/\gamma$ and $\tau_{m(i,o)} = a^2/\nu_{i,o}$ are the capillary and viscous relaxation time scales. If $Oh \gg 1$, the time scale for droplet relaxation τ_c is much greater than the time scale for diffusion of momentum τ_m, which implies that τ_c will dominate over the former; the droplet quickly establishes a quasi-steady flow, and the dynamics are dictated by interface deformation. On the other hand, if $Oh \ll 1$, then τ_m will dominate, and the dynamics are controlled by the inertia of both fluids. Indeed, it is unsurprising that the results in figure 4.2 do not display an overshoot: although $Oh_i < 1$, we have $Oh_o > 1/Oh_i$, and $\tau_{c,o}$ is dominant over the inner and outer momentum diffusion time scales. However, this does not mean that the capillary time scale $\tau_{c,o}$ determines the transient behavior of the system. As stated previously, $Sa_i \gg 1$ and $Sa_o \gg 1$, which represents the dominance of the charge relaxation time $\tau_e = \varepsilon\chi$ over $\tau_m = a^2/\nu$ both inside and outside of the drop. The ratio of electrical to droplet relaxation time scales τ_e/τ_c is greater than unity for both phases, which implies that the dynamics are controlled by the transport of charge to the interface. At early times $t\nu_i/a^2 \lesssim 1$, insufficient charge has reached the surface of the droplet to develop an appreciable tangential electrical stress. Thus, the drop behaves as a perfect dielectric, and adapts a prolate configuration. Eventually, sufficient charge arrives at the interface, and the droplet switches towards an oblate configuration (D/D_T crosses the origin in 4.2(a)). A similar explanation was offered by Supeene *et al.*[21] for their numerical calculations.

Following this line of reasoning, we move to a different model system, in which the medium is less viscous than the drop. The parameters are listed

in table 4.2. Note that the outer fluid viscosity and interfacial tension have changed relative to the previous system (table 4.1), the latter of which was slightly modified to decrease the Ohnesorge number of both fluids while still maintaining the feasibility of such a system in an experiment.[18] Finally, the conductivities of both oils were increased by two orders of magnitude in order to minimize the influence of charge relaxation and highlight the impact of fluid inertia on the system. Note, these conductivities are within the range of experimental values that characterize leaky dielectric liquids (see Fernández[38]).

Phase	ε_r	$1/\chi$ (S/m)	μ (Pa s)	ρ (kg/m^3)	a (mm)	γ (mN/m)
drop	3.0	1.2×10^{-10}	0.0484	960		
					4.0	4.8
medium	5.3	4.5×10^{-9}	0.0290	960		

Phase	Ca	Re	Oh	Sa	S	M	R
drop	0.007	0.05	0.4	0.68			
					1.8	0.6	0.03
medium	0.012	0.26	0.2	0.02			

Table 4.2: Second set of parameters for a droplet suspended in a weakly conductive medium. The organization is the same as in table 4.1.

The Ohnesorge number is now less than unity in both fluids, while $Re_{i,o}$ and $Ca_{i,o}$ are maintained at values low enough to validate the neglect of the non-linear inertial term and the small-deformation assumption. A comparison between the deformation obtained by employing the unsteady (A24) and quasi-steady (4.3) Stokes equations is displayed in figure 4.3(a). The lag in

the transient profile now begins essentially instantaneously at $t = 0$, although the dip towards a prolate conformation is not as pronounced as that in figure 4.2(a). Similar to figure 4.2(a), however, a lag is observed for the curve generated from the numerical inversion of (A24). In fact, it takes this curve roughly an order of magnitude longer to reach a deformation $D(t) \approx 0.1$ as opposed to the curve generated from (4.3). This lag at early times is proceeded by an overshoot in the deformation at intermediate times, which is followed by an algebraic tail before settling towards Taylor's steady value. Following the previous analysis, $Oh_{i,o} < 1$ together with $Sa_{i,o} < 1$ now represents quick charging of the interface and a dominant momentum diffusion time scale $\tau_{m(i,o)}$. This contributes towards the less pronounced initial prolate conformation as well as the overshoot and algebraic tail. A comparison between the numerical inversion of (A24) and the asymptotic expansions (4.35) and (4.37) is shown in figure 4.3(b), with good agreement observed once again.

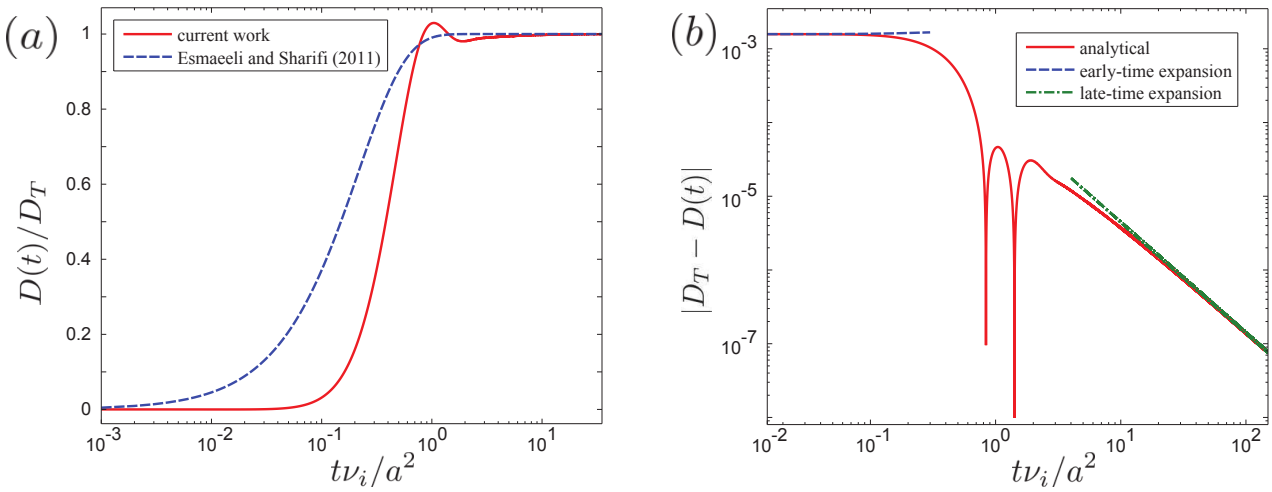

Figure 4.3: (a) Normalized transient deformation of a droplet for parameters listed in table 4.2. The solid curve (red online) is the inversion of (A24), which considers transient inertia and charge relaxation of both fluids, while the dashed curve (blue online) corresponds to (4.3) from Esmaeeli and Sharifi's work,[19] which assumes quasi-steady Stokes flow and instantaneous interfacial charging. The solid curve immediately reaches negative D/D_T values, which represents a prolate configuration. After this, the deformation profile crosses the origin at $t\nu_i/a^2 \approx 0.02$ while lagging (4.3), and overshoots before arriving at steady-state (4.1) with an algebraic tail. (b) Inversion of (A24) together with early- and late-time asymptotics (4.35) and (4.37), respectively.

Transient fluid inertia also affects the development of the flow inside and outside the drop. Esmaeeli and Sharifi[19] present open fluid streamlines that cross the surface of the droplet at early times (figures 2 and 5 in that paper). These streamlines evolve towards the outside of the drop, and four inner vortices emerge, yielding a steady configuration. Figure 4.4 presents streamlines for the parameters presented in table 4.2. The sequence (a) – (d) presents the development towards a steady flow in chronological order. As opposed to Esmaeeli and Sharifi, we observe that at first, four vortices already promote re-

circulation inside of the drop, while closed streamlines cross the surface (figure 4.4(a)). These vortices then disappear, and the fluid streamlines migrate outwards (figure 4.4(b)). While the streamlines are moving towards the outside of the surface, the four inner vortices reappear (figure 4.4(c)). The closed outer streamlines finally extend from the surface towards infinity, thereby appearing as open (figure 4.4(d)). This is consistent with figure 1 of Sozou,[29] although Sozou presented separately the streamlines due to the normal and tangential interfacial stresses. The illustrations of Esmaeeli and Sharifi are not incorrect, but rather reflect their neglect of charge relaxation and transient inertia, which is valid only for $Oh_{i,o} \gg 1$ and $Sa_{i,o} \ll 1$. As mentioned previously, these restrictions are often not valid for experimental systems.

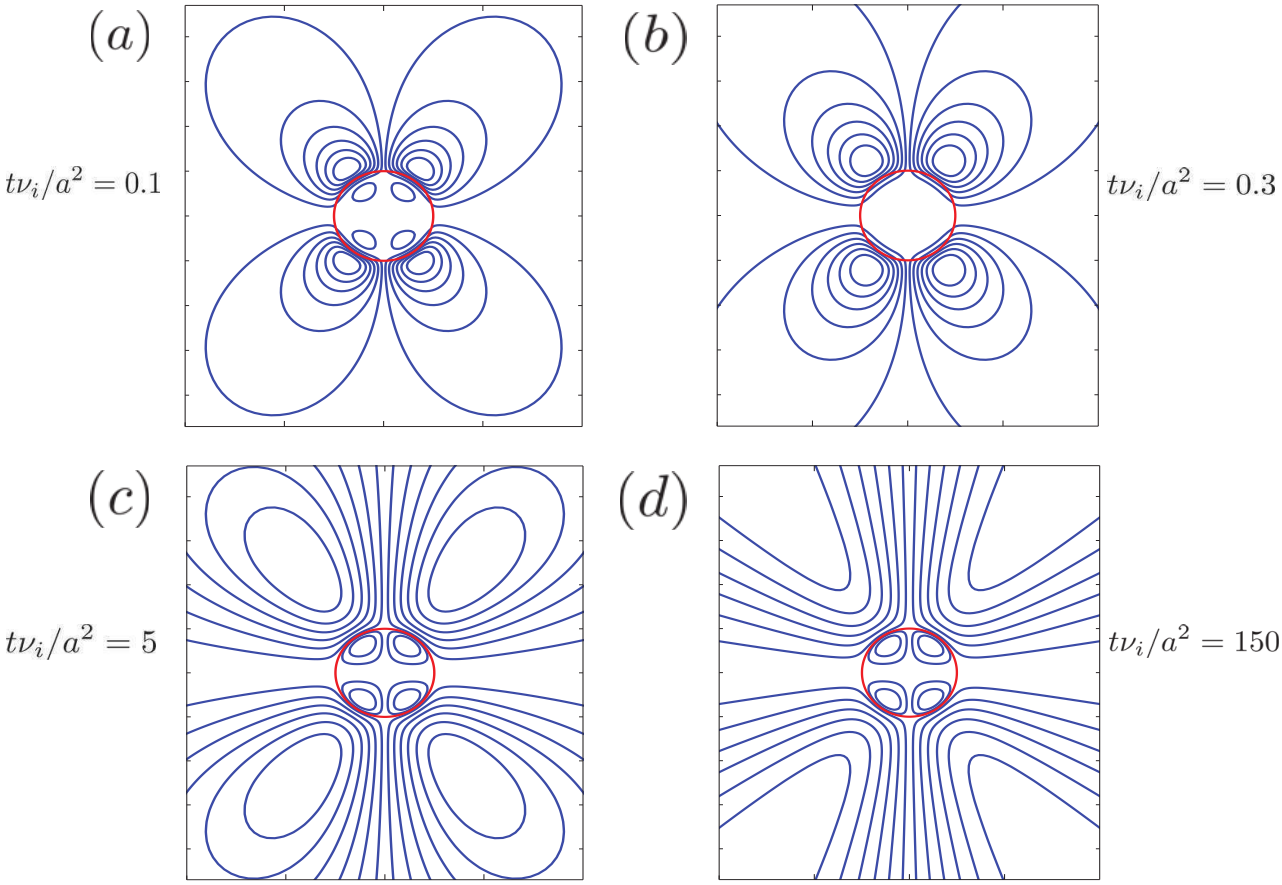

Figure 4.4: Fluid streamlines inside and outside of a droplet during the development of an electrohydrodynamic flow and drop deformation for parameters listed in table 4.2. The subfigures (a) – (d) are presented in chronological order, and the droplet surface is also shown. A steady flow pattern is achieved when $t\nu_i/a^2 \sim O(100)$.

4.4 Discussion

We have analyzed the deformation of a droplet suspended in a medium with a different permittivity, resistivity, and viscosity, under sudden exposure to a DC electric field. Both fluids were treated as leaky dielectrics, and the development of the deformation and flow were examined throughout time, as-

suming that the latter develops according to the unsteady Stokes equations. The novelty of our work is in the analytical study of the influence of linear fluid inertia and interfacial charging, whereas existing theoretical works exclusively consider the former[30,31] or the latter.[29] The presence or absence of an overshoot in the deformation is dictated by the value of an Ohnesorge number, which is the ratio of capillary to momentum diffusion time scales. Additionally, given that the final configuration of the drop is oblate, the extent of adaptation of an initial prolate configuration is controlled by the dimensionless quantity Sa, representing a ratio of the time scales for electrical to viscous relaxation. Consequently, $Oh_{i,o}$ and $Sa_{i,o}$ provide three time scales of interest for each phase: capillary $\tau_{c(i,o)} = \mu_{i,o}a/\gamma$, diffusion of momentum $\tau_{m(i,o)} = a^2/\nu_{i,o}$, and charge relaxation $\tau_{e(i,o)} = \varepsilon_{i,o}\chi_{i,o}$. The largest of these determines how the deformation evolves throughout time towards Taylor's steady-state (4.1). Note that non-monotonic evolutions towards a steady-state are a generic feature of flows governed by multiple time scales, and have been observed in thermocapillary motion of droplets[39] and inertial drop deformation in shear flows,[40] for example.

A value of $Oh \gg 1$ and $Sa \ll 1$ for either of the two phases represents a dominant $\tau_{c(i,o)}$, and provides results which do not differ qualitatively from (4.3), which assumes that inertia is negligible and charging of the droplet surface is instantaneous. If $Oh_{i,o}$ is fixed and Sa for either phase is increased such that $\tau_{e(i,o)}$ is dominant for a final oblate conformation, an increasingly pronounced transition towards an initial prolate shape indicates that at early times the droplet is behaving as a perfect dielectric.[21] Similar to a capacitor, after a surface charge $q(t,\theta)$ accumulates at the interface, the transition towards the oblate deformation takes place, and the development towards the

expected steady deformation substantially lags (4.3). A slow transient flow development was reported by Xu,[30] who observed the motion of fluorescent particles inside a silicone drop suspended in castor oil, and attributed this behavior to a finite electrical relaxation time scale and charge convection effects, the former of which was accounted for in a similar manner to (4.7). Note that for a final prolate configuration, no such transition to oblate would occur.

As Oh and Sa for either phase are decreased to make $\tau_{m(i,o)}$ dominant, an overshoot manifests. This overshoot is preceded by a transient profile which also lags (4.3). After this, an algebraic tail describes the settlement towards the steady deformation. Note that our constraint of creeping flow $Re_{i,o} \ll 1$ renders it difficult to observe a sustained oscillatory behavior towards steady-state, as observed in Supeene *et al.*[21] Supeene *et al.* considered finite Reynolds numbers, which contribute towards the appearance of a more pronounced oscillatory behavior. As shown in the series expansions in (4.35) and (4.37), the deformation is mathematically different from (4.3) at both early and late times. However, the series coefficients in (4.35) and (4.37) adjust themselves to provide a similar qualitative appearance as (4.3) when $Oh_{i,o} \to \infty$ and $Sa_{i,o} \to 0$. The quasi-steady assumption and neglect of interfacial charging are clearly inaccurate outside of this regime, which is experimentally relevant when considering a leaky dielectric system. For example, low Ohnesorge numbers are normally encountered for liquid jets,[41,42] and experimental studies[36,37] on oil-water systems have attained Ohnesorge numbers as low as $O(10^{-2})$, which is expected due to the low viscosity of water and its high interfacial tension against oil. It has been shown that conductive droplets suspended in dielectric media (such as a drop of deionized water in silicone oil) are reasonably well approximated by electrostatic theory.[16,43] Although we have developed

a model to describe an electrohydrodynamic phenomenon, the impact of inertia should still be probed through varying $Oh_{i,o}$, as overshoots have been previously presented in the absence of steady recirculatory flows.[23,24] Such a system, however, may provide additional complexities (e.g., density-matching).

Transient, or linear, inertia alone is enough to cause an overshoot in the deformation profile. Despite this, one may envision that convective inertia (finite Re) in (4.12) will result in additional dynamics not captured by our model. We acknowledge the work of others which has included a complete momentum balance;[21,22,24] however, directly comparing the presence and absence of nonlinear inertia at various $Oh_{i,o}$ has not yet been investigated. Few experiments regarding transient drop deformation have been conducted,[25,26] all of which have suggested a monotonic deformation similar to (4.3). As future work, we aim to experimentally explore the effect of varying Oh and Sa for a system of two fluids. The overshoot and shape transitions may be challenging to capture due to their relatively short-lived duration and small magnitude. On the other hand, capturing the lag at intermediate times for $Oh_{i,o} < 1$ or $Sa_{i,o} > 1$ should be more experimentally feasible, as the difference between the two curves in figures 4.2(a) and 4.3(a) can be an order of magnitude. Finally, the significant effect of inertia and finite electrical relaxation times highlighted in our work serves as motivation to consider systems such as suspended vesicles.[4] Despite the complexity compared with a fluid-fluid interface, our results serve as an incentive to examine the influence of inertia and charge relaxation on transient electrohydrodynamic vesicle deformation.

4.5 Conclusions

We have shown that linear inertia or charge relaxation can lead to non-monotonic transient droplet deformation under a uniform DC electric field. The importance of the former is characterized by the ratio of capillary to momentum diffusion time scales, the Ohnesorge number Oh; the importance of the latter is characterized by the ratio of charge relaxation to momentum diffusion time scales, Sa. Depending on the values of these dimensionless groups, one may obtain a prolate-oblate shape transition or an overshoot in the deformation, or a combination of the two (or neither). Importantly, experimental systems exist in which the values of Oh and Sa are such that transient inertia and interfacial charging cannot be neglected.

Appendix A: calculation of the electrical stresses

We begin with the Laplace transform of the axisymmetric solutions to Laplace's equation (4.4) for the potential $\phi^*_{i,o}$ in spherical coordinates that contain the angular form needed to satisfy the far-field condition $-\nabla^*\phi^*_o \to E_\infty \boldsymbol{e}_z$. These are

$$\widetilde{\phi}^*_i(r^*,\theta,s^*) = \left(\frac{c_9}{r^{*2}} + c_{10}r^*\right)\cos\theta \tag{A1}$$

and

$$\widetilde{\phi}^*_o(r^*,\theta,s^*) = \left(\frac{c_{11}}{r^{*2}} + c_{12}r^*\right)\cos\theta, \tag{A2}$$

where c_9 through c_{12} are dependent on s^*. The Laplace transform of ϕ^*_i and ϕ^*_o is taken for an easier implementation of the surface boundary conditions. Forcing $\widetilde{\phi}^*_i$ to remain bounded at the origin and applying $-\nabla^*\widetilde{\phi}^*_o \to E_\infty \boldsymbol{e}_z/s^*$ as $r^* \to \infty$ together with (4.8) and the Laplace transform of (4.5) provides

the following values for $c_9 - c_{12}$:

$$c_9 = 0, \tag{A3}$$

$$c_{10} = -\left(\frac{3E_\infty}{\tau_{m,i}\, s^*}\right)\left(\frac{Sa_i\, R\, S\, \tau_{m,i}\, s^* + 1}{Sa_i\, R\, \tau_{m,i}\, s^*(2S+1) + R + 2}\right), \tag{A4}$$

$$c_{11} = a^3\left(c_{10} + \frac{E_\infty}{\tau_{m,i}\, s^*}\right), \tag{A5}$$

and

$$c_{12} = -\frac{E_\infty}{\tau_{m,i}\, s^*}, \tag{A6}$$

from which the electric fields throughout both phases may be readily calculated. The expressions for these in the time domain are

$$\boldsymbol{E}_i^* = \frac{3E_\infty}{(R+2)(2S+1)}\left((RS-1)e^{-\frac{R+2}{Sa_i R(2S+1)}\frac{t^*}{\tau_{m,i}}} + 2S + 1\right)\boldsymbol{e}_z, \tag{A7}$$

and

$$\begin{aligned}\boldsymbol{E}_o^* = {} & \frac{E_\infty}{(R+2)(2S+1)}\left(\frac{a}{r^*}\right)^3\Bigg[-6(RS-1)e^{-\frac{R+2}{Sa_i R(2S+1)}\frac{t^*}{\tau_{m,i}}} \\ & +(2S+1)\left(\left(\frac{r^*}{a}\right)^3(R+2) + 2(R-1)\right)\Bigg]\cos\theta\,\boldsymbol{e}_r \\ & -\frac{E_\infty}{(R+2)(2S+1)}\left(\frac{a}{r^*}\right)^3\Bigg[3(RS-1)e^{-\frac{R+2}{Sa_i R(2S+1)}\frac{t^*}{\tau_{m,i}}} \\ & +(2S+1)\left(\left(\frac{r^*}{a}\right)^3(R+2) - R + 1\right)\Bigg]\sin\theta\,\boldsymbol{e}_\theta,\end{aligned} \tag{A8}$$

where $\boldsymbol{e}_r$ and $\boldsymbol{e}_\theta$ are basis vectors in the radial and angular direction, respectively. The electric fields are inverted back to the time domain to calculate the electrical interfacial stresses, after which the Laplace transform is taken again to arrive at (4.9) and (4.10). In addition, as $q^*(t^*, \theta)$ was eliminated to obtain

(4.8), it may be calculated through (4.6), yielding

$$q^*(t^*,\theta) = 3\,\varepsilon_i E_\infty \frac{RS-1}{R+2}\left(1 - e^{-\frac{R+2}{Sa_i R(2S+1)}\frac{t^*}{\tau_{m,i}}}\right)\cos\theta. \tag{A9}$$

The $\cos\theta$ dependence indicates that the net charge on the droplet is identically zero at all times during the charging.

Appendix B: scaling arguments to affirm the use of (4.7)

The full dimensionless equation describing conservation of charge at the surface of the droplet may be written as

$$Sa_i\frac{\partial q}{\partial t} - Re_{E,i}\Big(\boldsymbol{u}\cdot\nabla_s q - q\boldsymbol{n}\cdot(\boldsymbol{n}\cdot\nabla)\boldsymbol{u}\Big) = -\frac{\partial\phi_i}{\partial r} + R\frac{\partial\phi_o}{\partial r}, \tag{A10}$$

where $\nabla_s = \nabla - \boldsymbol{n}(\boldsymbol{n}\cdot\nabla)$ denotes the surface gradient and $Re_{E,i}$ is the electric Reynolds number[14,30] based on the drop. The surface charge $q(t,\theta)$ has been normalized by $\varepsilon_i E_\infty$, while the velocity $\boldsymbol{u}$ together with the differential operators, ∇, ∇_s, and $\frac{\partial}{\partial r}$ have been made dimensionless as in main text. From left to right, the two terms that multiply $Re_{E,i}$ represent convection of charge along the boundary and a change in surface charge density due to dilation of the interface.[14,21] Here, $Re_{E,i} = \varepsilon_i\chi_i U/a = \tau_{e,i}/\tau_{f,i}$, where $\tau_{f,i} = a/U$ is a characteristic flow time scale. After some manipulation, the electric Reynolds number may be rewritten as $Re_{E,i} = Ca_i Sa_i/Oh_i$. As an example, inserting the dimensionless groups from table 4.2, we find that $Re_{E,i} \approx 0.01$ and $Re_{E,o} \approx 1\times10^{-3}$, which permits the disregard of the terms that multiply the electric Reynolds number. One can always decrease Ca_i by decreasing the electric field E_∞ to comply with the assumption behind (4.7).

Appendix C: full solution of the ODE for $\widetilde{f}_{1(i,o)}(r,s)$

Recall the ODE for $\widetilde{f}_{1(i,o)}(r,s)$ provided in (4.17). Given that this is a non-constant coefficient differential equation, the Frobenius method is the most intuitive approach towards a solution. Seeking a power series about $r=0$ of the form $\sum_{n=0}^{\infty} a_n r^{n+\alpha}$ yields $\alpha = -2, 0, 3$, and 5, and two exact solutions: $1/r^2$ and r^3. There are two other series solutions about the same point of expansion; however, we resort to another method to find the remaining two solutions.

Note that despite the regularity of the point $r=0$, $r \to \infty$ is an irregular singular point of (4.17). Hence, a convergent power-series solution about this point is not guaranteed. Indeed, the only well behaved series solution about $r \to \infty$ may be found via a change of variables $\bar{r} = 1/r$. This solution is $\bar{r}^2 = 1/r^2$, which was found above. We therefore turn to the method of dominant balance,[44] which identifies the controlling factor of a solution near an irregular singular point. To find this leading behavior, a substitution $\widetilde{f}_{1(i,o)}(r,s) = e^{\widetilde{S}_1(r,s)}$ is inserted into (4.17). As an approximation, it is customary to neglect all higher-order derivatives after making this substitution, and check if this assumption was valid after a solution is obtained. The fourth order linear differential equation is then exchanged for a first order nonlinear equation:

$$\alpha r^4 \left(\frac{d\widetilde{S}_1(r,s)}{dr}\right)^4 - (sr^4 + 12\alpha r^2)\left(\frac{d\widetilde{S}_1(r,s)}{dr}\right)^2 + 24\alpha r \frac{d\widetilde{S}_1(r,s)}{dr} + 6sr^2 = 0. \tag{A11}$$

As we are concerned with the behavior of a solution as $r \to \infty$, we only retain the terms that are most significant in that limit, which yields

$$\alpha \left(\frac{d\widetilde{S}_1(r,s)}{dr}\right)^4 - s\left(\frac{d\widetilde{S}_1(r,s)}{dr}\right)^2 = 0. \tag{A12}$$

The two solutions that are consistent with our assumptions are $\widetilde{S}_1(r,s) = -r\sqrt{\frac{s}{\alpha}}$ and $\widetilde{S}_1(r,s) = r\sqrt{\frac{s}{\alpha}}$, which in turn determines the leading behavior of $\widetilde{f}_{1(i,o)}(r,s)$ as $e^{-r\sqrt{\frac{s}{\alpha}}}$ and $e^{r\sqrt{\frac{s}{\alpha}}}$. To find the two full solutions for $\widetilde{f}_{1(i,o)}$, we work with the former controlling factor $e^{-r\sqrt{\frac{s}{\alpha}}}$ and perform the substitution $\widetilde{f}_{1(i,o)}(r,s) = \widetilde{V}(r,s)\, e^{-r\sqrt{\frac{s}{\alpha}}}$. After replacing this expression in (4.17), an ODE is obtained for $\widetilde{V}(r,s)$ as

$$\alpha^{\frac{3}{2}} r^3 \frac{d^4\widetilde{V}(r,s)}{dr^4} - 4\alpha r^3\sqrt{s}\,\frac{d^3\widetilde{V}(r,s)}{dr^3} + (5\sqrt{\alpha}r^3 s - 12\alpha^{\frac{3}{2}} r)\frac{d^2\widetilde{V}(r,s)}{dr^2} + (-2r^3 s^{\frac{3}{2}} + 24\alpha r\sqrt{s} + 24\alpha^{\frac{3}{2}})\frac{d\widetilde{V}(r,s)}{dr} - (6\sqrt{\alpha}rs + 24\alpha\sqrt{s}\,)\,\widetilde{V}(r,s) = 0. \tag{A13}$$

Seeking a series expansion of the form $\sum_{n=0}^{\infty} a_n r^{-n}$ now allows the exact solution

$$\widetilde{V}(r,s) = s + \frac{3\sqrt{\alpha s}}{r} + \frac{3\alpha}{r^2}, \tag{A14}$$

where the r^0 coefficient s can take on any value, as long as consistency is kept with the subsequent terms in (A14). This is because $\widetilde{V}$ will be used to build an overall general solution. We now have another exact solution for $\widetilde{f}_{1(i,o)}$, which was found by analyzing the behavior of our equations far away from the droplet. Following the same method, a similar substitution $\widetilde{f}_{1(i,o)}(r,s) = \widetilde{W}(r,s)\, e^{r\sqrt{\frac{s}{\alpha}}}$ is made to find the fourth and final solution. The expression for $\widetilde{W}$ results in

$$\widetilde{W}(r,s) = s - \frac{3\sqrt{\alpha s}}{r} + \frac{3\alpha}{r^2}. \tag{A15}$$

Combining all of the solutions previously introduced provides (4.19), which we

present separately for the inner and outer phases as

$$\widetilde{f}_{1,i}(r,s) = c_1 r^3 + \frac{c_2}{r^2} + c_3 e^{r\sqrt{s}}\left(s - \frac{3\sqrt{s}}{r} + \frac{3}{r^2}\right) + c_4 e^{-r\sqrt{s}}\left(s + \frac{3\sqrt{s}}{r} + \frac{3}{r^2}\right), \tag{A16}$$

and

$$\widetilde{f}_{1,o}(r,s) = c_5 r^3 + \frac{c_6}{r^2} + c_7 e^{r\sqrt{\frac{s}{M}}}\left(s - \frac{3\sqrt{Ms}}{r} + \frac{3M}{r^2}\right) + c_8 e^{-r\sqrt{\frac{s}{M}}}\left(s + \frac{3\sqrt{Ms}}{r} + \frac{3M}{r^2}\right). \tag{A17}$$

Consequently, finding a simplified expression for $\widetilde{f}_{1,i}$ that is non-divergent at the origin first requires us to set $c_2 = 0$. Besides this, a Maclaurin series expansion is needed to determine the relationship between c_3 and c_4:

$$\widetilde{f}_{1,i}(r,s) = c_1 r^3 + \frac{3\alpha^2(c_3 + c_4)}{s r^2} - \frac{1}{2}\alpha\,(c_3 + c_4) + O(r^2). \tag{A18}$$

It now becomes clear that $c_3 = -c_4$ for $\widetilde{f}_{1,i}$ to vanish at $r = 0$. Equation (A16) then becomes

$$\widetilde{f}_{1,i}(r,s) = c_1 r^3 + c_3\left[e^{r\sqrt{s}}\left(s - \frac{3\sqrt{s}}{r} + \frac{3}{r^2}\right) - e^{-r\sqrt{s}}\left(s + \frac{3\sqrt{s}}{r} + \frac{3}{r^2}\right)\right], \tag{A19}$$

which shows how the Bessel function $I_{\frac{5}{2}}$ appears in (4.20), where $C_1 = c_1$ and $C_2 = c_3\, s^{\frac{5}{4}}\sqrt{2\pi}$. Carrying out the analogous procedure to determine which constants to discard for $\widetilde{f}_{1,o}$ in (A17) is simpler in comparison to (A16). It is clear that to avoid deviations as $r \to \infty$, one must discard c_5 and c_7, which yields

$$\widetilde{f}_{1,o}(r,s) = \frac{c_6}{r^2} + c_8\, e^{-r\sqrt{\frac{s}{M}}}\left(s + \frac{3\sqrt{Ms}}{r} + \frac{3M}{r^2}\right). \tag{A20}$$

Again, it is easy to see how the Bessel function $K_{\frac{5}{2}}$ appears in (4.21), where $C_3 = c_6$ and $C_4 = c_8\, s^{\frac{5}{4}}\sqrt{2}\Big/ M^{\frac{1}{4}}\sqrt{\pi}$.

Appendix D: constants in (4.35) and (4.37), and expression for $\widetilde{D}(s)$

The constants $C_1 - C_4$ in (4.20) and (4.21) are dependent upon values for the parameters s, S, M, R, Oh_i, and Sa_i, and are too lengthy to list in a manner that is convenient for the reader to interpret. As stated previously, we are able to provide a Mathematica file which contains the analytical expressions for these upon request. The constants γ, ϵ, and η presented in the asymptotic expansions (4.35) and (4.37) are presented below:

$$\gamma = \frac{9(16M+19)(RS-1)}{400\sqrt{M}(M+1)^2(R+2)^2}, \tag{A21}$$

$$\epsilon = \frac{27(S-1)^2 S}{10(2S+1)^2}, \tag{A22}$$

and

$$\eta = -\frac{27\sqrt{M}(S-1)^2 S}{2\left(\sqrt{M}+1\right)(2S+1)^2}, \tag{A23}$$

while the full analytical expression for the Laplace-space deformation $\widetilde{D}(s)$ from which the expansions in (4.35) and (4.37) were generated reads

$$
\begin{aligned}
\widetilde{D}(s) \;=\; & \Big[27Ca_i(\sqrt{s}\cosh(\sqrt{s})(2(2S+1)((s+15)((R(5R+6)+5)S-16)M^{\frac{3}{2}}+\sqrt{s}(s+15)\\
&\times((R(5R+6)+5)S-16)M+(s((s+R(10R+(R-2)s-51)+10)S+31)-30((R(R+6)\\
&+1)S-8))\sqrt{M}-\sqrt{s}(30((R(R+6)+1)S-8)+s((R(5R+21)+5)S-31)))+RSSa_is\\
&\times(Rs(5(s+15)M^{\frac{3}{2}}+5\sqrt{s}(s+15)M+(s(s+10)-30)\sqrt{M}-5\sqrt{s}(s+6))(2S+1)Sa_i(S-1)^2\\
&+\sqrt{M}(6(s(s+10)-30)S^2+2(-3s^2+s+330)S+31s+R(-(s(3s+92)+390)S^2-31Ss\\
&+3s(s+10)-30(8S+3))+240)+M^{\frac{3}{2}}(s+15)(30S^2-62S+R(S(17S+16)+15)-16)\\
&+M\sqrt{s}(s+15)(30S^2-62S+R(S(17S+16)+15)-16)+\sqrt{s}(-30(s+6)S^2+92Ss+660S\\
&+31s-R(30(S(13S+8)+3)+s(S(47S+31)+15))+240)))+\sinh(\sqrt{s})(RSSa_is(Rs(-15\\
&\times(2s+5)M^{\frac{3}{2}}-15\sqrt{s}(2s+5)M-5(s^2-6)\sqrt{M}+\sqrt{s}(s(s+15)+30))(2S+1)Sa_i(S-1)^2\\
&-3M^{\frac{3}{2}}(2s+5)(30S^2-62S+R(S(17S+16)+15)-16)-3M\sqrt{s}(2s+5)(30S^2-62S+R\\
&\times(S(17S+16)+15)-16)+\sqrt{M}(-5(6S^2-4S+1)s^2-111(2S+1)s+60(S-4)(3S+1)\\
&+R(5(5S^2+S-3)s^2+111S(2S+1)s+30(S(13S+8)+3)))+\sqrt{s}((2S(3S-8)-5)s^2+3\\
&\times(2S(15S-52)-37)s+60(S-4)(3S+1)+R((S(7S+5)+3)s^2+3(S(59S+37)+15)s\\
&+30(S(13S+8)+3))))-2(2S+1)(3(2s+5)((R(5R+6)+5)S-16)M^{\frac{3}{2}}+3\sqrt{s}(2s+5)\\
&\times((R(5R+6)+5)S-16)M+(5(((R-3)R+1)S+1)s^2-111(RS-1)s-30((R(R+6)\\
&+1)S-8))\sqrt{M}+\sqrt{s}(s(5s-((s+15)R^2+3(s+27)R+s+15)S+111)-30((R(R+6)+1)\\
&\times S-8)))))\Big]/\Big[2s(2S+1)(Rs(2S+1)Sa_i+R+2)(R(Sa_i(2Ss+s)+2)+4)(Oh_i^2s((48(-18M^2\\
&+M+17)s^{\frac{3}{2}}-105(M-1)s^{\frac{5}{2}}-585(M-1)\sqrt{M}s^2-288(M-1)\sqrt{M}(3M+7)s-720(M\\
&-1)(3M+2)\sqrt{s}-720(M-1)\sqrt{M}(3M+2)+5s^{\frac{7}{2}})\sinh(\sqrt{s})+\sqrt{s}(25(M-1)s^{\frac{5}{2}}+48(M\\
&-1)(3M+7)s^{\frac{3}{2}}+5\sqrt{M}s^3+105(M-1)\sqrt{M}s^2+48(M-1)\sqrt{M}(3M+32)s+720(M-1)\\
&\times(3M+2)\sqrt{s}+720(M-1)\sqrt{M}(3M+2))\cosh(\sqrt{s}))+24((-15M^{\frac{3}{2}}(2s+5)-5\sqrt{M}(s^2-6)\\
&-15M\sqrt{s}(2s+5)+\sqrt{s}(s(s+15)+30))\sinh(\sqrt{s})+\sqrt{s}(5M^{\frac{3}{2}}(s+15)+5M\sqrt{s}(s+15)+\sqrt{M}\\
&\times(s(s+10)-30)-5\sqrt{s}(s+6))\cosh(\sqrt{s})))\Big]. \qquad \text{(A24)}
\end{aligned}
$$

Appendix E: comparison to previous work

To verify that our results approach those of Esmaeeli and Sharifi[19] as the capillary time scales $\tau_{c(i,o)}$ become dominant, we consider $\{Oh_i = 0.4,\ Oh_o = 26.2\}$ (for which an overshoot is absent), and probe the influence of a varying electrical relaxation time scale $\tau_{e(i,o)}$. Three curves corresponding to $\{Sa_i = 68.0,\ Sa_o = 197.0\}$, $\{Sa_i = 20.4,\ Sa_o = 59.1\}$, and $\{Sa_i = 0,\ Sa_o = 0\}$ are shown in figure 4.5. Our expression (A24) becomes identical to the monotonic deformation profile of Esmaeeli and Sharifi (4.3) as $Sa_{i,o} \to 0$, i.e., as the charge relaxation becomes instantaneous.

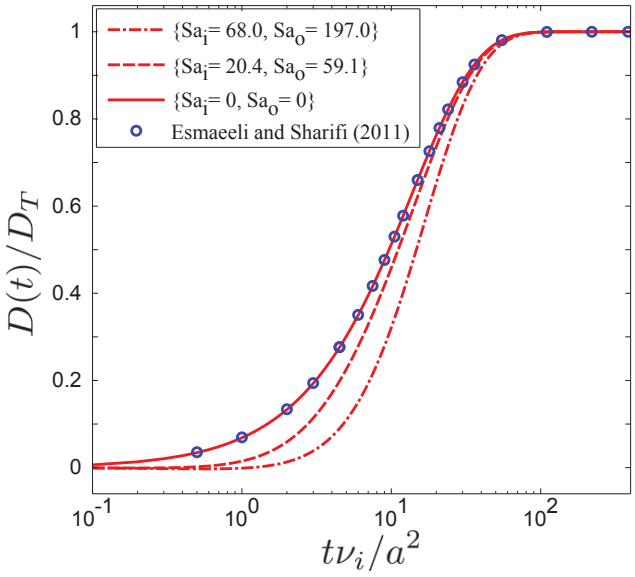

Figure 4.5: Normalized transient deformation of a droplet. The parameters are those listed in table 4.1, with the exception of the viscosity ratio $M = 60$, which provides $\{Oh_i = 0.4,\ Oh_o = 26.2\}$, for which no overshoot is observed. The curves represent the inversions of (A24), while the circles correspond to (4.3) from Esmaeeli and Sharifi.[19] As expected, our results match those of Esmaeeli and Sharifi as $Sa_{i,o}$ approaches zero.

Sozou[29] only tabulated six values of deformation versus time in tables 1

and 2, which suggest a monotonic transient deformation profile. Furthermore, Sozou did not provide actual values for the permittivity S and resistivity R ratios. Thus, direct comparison of our work to Sozou's is difficult. However, the parameters presented in tables 1 and 2 of Sozou[29] yield $\{Oh_i = 12.9, Oh_o = 25.8\}$. For these values of the Ohnesorge number, our calculations predict a monotonic deformation as well. In addition, recall that our stream function in equations (4.20) and (4.21) matches Sozou's solution ((19) and (20) in that paper). Qualitative agreement is also observed in the streamline pattern between our figure 4.4 and Sozou's figure 1.

5. Nonlinear electrohydrodynamics of slightly deformed oblate drops

5.1 Introduction

Taylor's model[13] predicts accurate values for the steady deformation at small capillary numbers $Ca_{i,o}$.[16–18] Here, the double subscript i, o is implemented to label a certain quantity for both the drop and medium, e.g. $Ca_{i,o}$ signifies Ca_i and Ca_o. The large capillary number regime has received computational treatment to enable the prediction of larger, nonlinear, steady–state deformations of isolated leaky dielectric drops[21,45–50] as well as their breakup.[21,45–48] In this nonlinear regime, the stable drop shape need not be spheroidal. Sherwood[45] was the first to numerically calculate the prolate deformation of a weakly conducting drop subjected to a uniform DC electric field. By implementing the boundary integral method to calculate the electrostatic field and flow field, his work predicted the equilibrium drop shapes and unstable configurations for creeping flow, i.e. Reynolds numbers $Re_{\mathrm{Flow}(i,o)} = \rho_{i,o} U a/\mu_{i,o} \to 0$, where $\rho_{i,o}$ denotes the density of either phase and U is a characteristic flow strength. Additionally, the viscosity ratio was set

to unity ($M = 1$). Lac and Homsy[48] considered prolate and oblate conformations, and a differing viscosity between the two phases ($M \neq 1$). By performing a thorough investigation of the dimensionless parameter space spanned by $S = \varepsilon_i/\varepsilon_o$, $R = \chi_i/\chi_o$, and $M = \mu_i/\mu_o$, they predicted various stable drop configurations, as well as highly nonlinear (e.g. multi–lobed) shapes and breakup modes. Their work also analyzed how a differing viscosity between the drop and medium can either enhance stability or promote breakup. Both of these works considered either steady–state deformations or breakup of drops under high field strengths.

Lac and Homsy[48] also compared simulation results against two sets of experiments from Ha and Yang,[51] which measured the steady deformation of a castor oil drop immersed in silicone oil at varying electric capillary number Ca_o. To calculate the interfacial tension γ, Lac and Homsy rescaled the capillary number Ca_o corresponding to the experimental data of Ha and Yang to fit the $O(Ca_o^2)$ weak–field perturbation theory of Ajayi,[52] instead of the $O(Ca_o)$ theory developed by Taylor.[13] This provided a numerically computed deformation curve that matched the experiments for capillary numbers $Ca_o \lesssim 0.2$, with some deviation observed at higher capillary numbers. Further rescaling of the capillary number as well as a slight modification of the dimensionless ratios S and R provided another computational result that yielded a closer match to the experiments of Ha and Yang.[51] Lac and Homsy concluded that careful measurement of the system properties is imperative, and that considering nonlinear effects such as interfacial charge convection may be required to match experimental measurements in some cases. Feng[47] and Fernández[49] have incorporated charge convection when calculating steady–state deformations. Feng[47] implemented a Galerkin finite–element method,

while Fernández[49] used a front–tracking/finite–volume method. Similar to Lac and Homsy,[48] Feng[47] also emphasized the importance of accurate measurement of physical properties, in particular the fluid conductivities ($1/\chi_{i,o}$). The work of Fernández[49] assumes values for the conductivity of both phases when comparing against the experimental measurements of Vizika and Saville.[16] Furthermore, as stated by Feng,[47] the experimental work of Torza *et al.*,[28] Vizika and Saville,[16] and Tsukada *et al.*[53] reports measurements for the steady deformation as a function of $E_\infty^2 a$ without separately stating the values for E_∞ and a. This does not provide sufficient information to quantify the effect of charge convection, which is reflected through the electric Reynolds numbers $Re_{i,o} = \varepsilon_{i,o}\chi_{i,o}U/a = E_\infty^2 \varepsilon_{i,o}^2 \chi_{i,o}/\mu_{i,o}$,[14] where $U \sim \varepsilon_{i,o}E_\infty^2 a/\mu_{i,o}$ is a characteristic velocity scale, which may be expressed in terms of the magnitude of the field E_∞ by balancing electrical and viscous stresses. This dimensionless number is also defined as a ratio of charge relaxation timescales $\tau_{e(i,o)} = \varepsilon_{i,o}\chi_{i,o}$ (a characteristic time for charge to reach the interface) to flow timescale $\tau_f = a/U$. We provide an in–depth discussion on this dimensionless group and its implications for electrohydrodynamic drop deformation in the following sections. The computational studies of Feng[47] and Fernández[49] concluded that surface charge convection suppresses steady–state oblate deformations and strengthens steady–state prolate deformations. Our work, which considers the effect of charge convection on transient deformation via the boundary integral method, also predicts weaker oblate configurations and a strong influence of interfacial charge convection on relatively small deformations.

The transient deformation of a leaky dielectric drop has also received theoretical[19,54,55] and computational[21,56] treatment. For such low–conductivity

systems, the finite amount of time taken for a quantity of charge q^* to arrive at the interface, characterized by the charge relaxation timescales $\tau_{e(i,o)}$, implies that another form of charge transport must be accounted for: the interfacial accumulation of charge. Although this transient phenomenon yields the same steady deformation, it may yield a nonmonotonic approach towards steady–state when the ratio $\tau_{e(i,o)}/\tau_p$ is not small (where τ_p represents a process timescale different from the convective timescale τ_f[15]). Although the influence of the electrical relaxation timescales $\tau_{e(i,o)}$ has been considered when describing phenomena such as stability[57] and tipstreaming[58] of jets, less attention has been provided to its influence on the transient behavior of isolated, weakly conducting drops exposed to uniform DC electric fields. Supeene *et al.*[21] implemented the finite element method to predict the transient deformation of a leaky dielectric drop via a general electrokinetic model and a surface charge conservation equation. Lanauze *et al.*[55] developed an $O(Ca)$ perturbation theory that accounts for charge relaxation and linear inertia. These computational and theoretical efforts have predicted prolate–oblate shape transitions at intermediate times for ultimately steady oblate conformations due to the dominance of the charge relaxation timescales $\tau_{e(i,o)}$ (i.e. they are the timescales of longest duration). As these timescales are increased, the accumulation of interfacial charge q^* is decelerated, which causes the fluids to initially behave as a system of two perfect dielectrics that deform in a prolate fashion due to the absence of any substantial induced electrohydrodynamic flow. Eventually, the steady–state surface charge density profile is slowly reached, thus achieving the expected recirculatory flow and ultimate oblate configuration.

A major conclusion of the present chapter is that both charge relaxation and charge convection must be accounted for when modeling the transient

deformation of low–conductivity drops. An example of such a system – implemented in our experiments – is a millimeter–sized oil drop under a field of strength on the order of kV/cm. Our focus will be on the transient approach towards steady oblate configurations, which will be predicted via the boundary integral method. We account for both charge relaxation and charge convection through a governing equation that considers the transport of interfacial charge. Previous researchers have implemented the boundary integral method without charge relaxation and charge convection to calculate the steady deformation of drops under electric fields.[45,48,59,60] Unlike Supeene *et al.*[21] and Lanauze *et al.*,[55] we compare our calculations for transient deformation against an experimental system consisting of a silicone oil drop suspended in a castor oil medium, with electrical material properties accurately measured via electrochemical impedance spectroscopy. To our knowledge, this is the first direct comparison of computation against experiment for the transient nonlinear deformation of a leaky dielectric drop.

5.2 Problem formulation

Consider a leaky dielectric drop of permittivity ε_i, resistivity χ_i, and viscosity μ_i suspended in a medium with permittivity ε_o, resistivity χ_o, and viscosity μ_o, respectively (figure 5.1). The two phases are assumed to be density–matched ($\rho_o = \rho_i$). A uniform DC electric field is applied, which induces tangential electrical stresses at the interface between the drop and medium. The electrical stresses are balanced by viscous stresses, which in turn induce fluid flow inside and outside of the drop. The induced flow may be directed from the poles towards the equator of the drop (pole to equator), or from the equator towards the poles (equator to pole), depending on the ratio of the values of the characteristic timescales for the development of interfacial

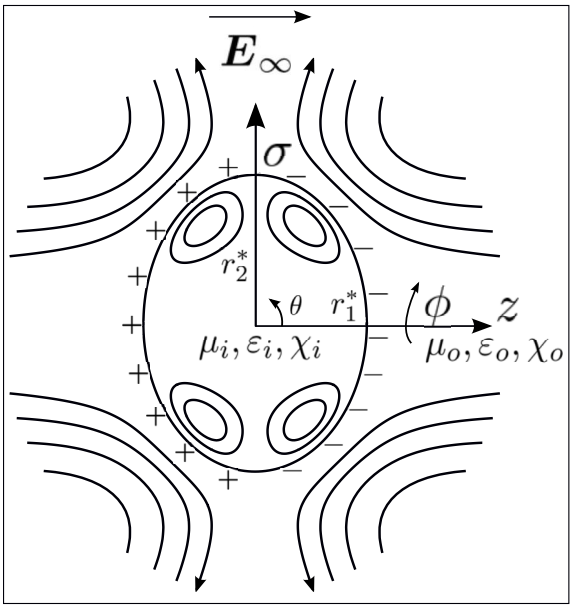

Figure 5.1: Schematic of the electric field–induced oblate deformation of a weakly conducting drop. The drop of viscosity μ_i, permittivity ε_i, and resistivity χ_i is suspended in a medium with properties μ_o, ε_o, and χ_o, respectively. The case considered is that for which the inner charging timescale $\tau_{e,i} = \varepsilon_i \chi_i$ is greater than the outer charging timescale $\tau_{e,o} = \varepsilon_o \chi_o$, which yields the surface charge distribution and oblate deformation qualitatively drawn here. The electric field is directed from left to right, while streamlines are depicted inside and outside of the drop. The direction of flow is from the poles ($\theta = 0, \pi$) towards the equator ($\theta = \pi/2$) of the drop. The electric field and induced fluid flow are both independent of the azimuth ϕ. Here, (σ,ϕ,z) corresponds to the set of cylindrical coordinates, while θ represents the polar angle measured from the positive z–axis. The major and minor semi–axes are denoted by r_2^* and r_1^*, respectively.

charge of both phases $\tau_{e(i,o)} = \varepsilon_{i,o}\chi_{i,o}$ (also known as the charge relaxation timescales[15]). If the electrical relaxation timescale of the medium is greater than that of the drop ($\tau_{e,o} > \tau_{e,i}$), the flow is directed from equator to pole; the converse yields a flow that is pole to equator ($\tau_{e,i} > \tau_{e,o}$). Prolate drops may experience flows that are either equator to pole or pole to equator; oblate drops exclusively undergo flows that are pole to equator.[18,48] In this work, we only consider steady deformations that are oblate and axisymmetric (no dependence on the azimuth ϕ shown in figure 5.1). This permits the use of a cylindrical coordinate system (σ,ϕ,z) when quantifying the drop deformation.

5.3 Governing equations

We utilize the boundary integral method to calculate the electric field and fluid velocity at the interface, and subsequently the deformation of the drop throughout time. We account for the interfacial accumulation of charge and the convection of that charge by the induced electrohydrodynamic flow, the latter of which couples the field and flow governing equations.

5.3.1 Electric field

The first step is to calculate the electric field at the interface separating the drop and medium. The electric field is irrotational, and we neglect any diffuse charge due to the low–conductivity fluids inherent to leaky dielectric systems. In this framework, Gauss's law for electrostatics reduces to Laplace's equation for the inner and outer electrostatic potential $\phi^*_{i,o}$.[48,59,60] One boundary condition dictates the outer electric field to approach the applied field $\boldsymbol{E}^*_o = -\nabla^*\phi^*_o \to \boldsymbol{E}_\infty$ at large distances from the drop. Two interfacial boundary conditions require that[48,59]

$$E^*_{t,o} = E^*_{t,i} \tag{5.1}$$

and

$$\varepsilon_o E^*_{n,o} - \varepsilon_i E^*_{n,i} = q^*, \tag{5.2}$$

where $E^*_{t(i,o)} = \boldsymbol{E}^*_{i,o} \cdot \boldsymbol{t}$ denotes the tangential components of the electric fields at the boundary that separates the two phases, and $\boldsymbol{t}$ is a unit tangent vector that is positive in the counter–clockwise direction (note that the latter should not be confused with dimensionless time t, which is a scalar quantity). The normal components of the electric fields at the interface are designated by $E^*_{n(i,o)} = \boldsymbol{E}^*_{i,o} \cdot \boldsymbol{n}$, where $\boldsymbol{n}$ is a unit normal vector that is positive when pointing outward from the drop. The condition (5.1) imposes a continuous tangential electric field across the interface (or equivalently, a continuity in potential), while (5.2) relates the jump in electric displacement caused by the surface charge q^* that accumulates due to the differing permittivity ε and resistivity χ between the two phases. The final electrical boundary condition at the surface of the drop describes the conservation of interfacial charge, namely

$$\frac{1}{\chi_i} E^*_{n,i} - \frac{1}{\chi_o} E^*_{n,o} = \frac{\partial q^*}{\partial t^*} + \nabla^*_s \cdot (\boldsymbol{u}^*_o \, q^*). \tag{5.3}$$

The first term on the right–hand side represents charge relaxation, i.e. the temporal accumulation of charge at the interface. The second term accounts for charge convection and changes in the surface charge density q^* due to dilation of the interface.[15] For brevity, we refer to this second term as the convective term, since it is responsible for surface charge convection. Note that the appearance of the fluid velocity $\boldsymbol{u}^*_o$ in (5.3) couples the electrostatic and flow fields.

We now non–dimensionalize the equations for the electric part of the problem. Distance is made dimensionless with the radius of the initial spherical

drop a. The electric fields $\boldsymbol{E}^*_{i,o}$ are normalized by the magnitude of the uniform applied field E_∞. The charge density q^* is normalized by $\varepsilon_o E_\infty$, while time t^* is made dimensionless with the outer electrical relaxation timescale $\tau_{e,o} = \varepsilon_o \chi_o$ due to the fact that the timescales $\tau_{e(i,o)}$ are largest for our experimental system. Finally, the velocities $\boldsymbol{u}^*_{i,o}$ are normalized by $U \sim \varepsilon_o E_\infty^2 a/\mu_o$. These scalings are applied to all equations henceforth. Laplace's equation may be reformulated as an integral equation that satisfies the far–field condition and (5.1), which reads[48,59,60]

$$\boldsymbol{E}^\infty \cdot \boldsymbol{n}(\boldsymbol{x}) - \frac{1}{4\pi} \oint_A \frac{\boldsymbol{r} \cdot \boldsymbol{n}(\boldsymbol{x})}{r^3} (E_{n,o}(\boldsymbol{y}) - E_{n,i}(\boldsymbol{y})) dA(\boldsymbol{y}) = \frac{1}{2} \left[E_{n,o}(\boldsymbol{x}) + E_{n,i}(\boldsymbol{x}) \right], \tag{5.4}$$

where the closed integral is over the surface A of the drop. Here, $\boldsymbol{r} = \boldsymbol{y} - \boldsymbol{x}$ is the distance between an observation point $\boldsymbol{y}$ that is free to move throughout the boundary and a fixed source point $\boldsymbol{x}$ on the interface, while $r = \sqrt{\boldsymbol{r} \cdot \boldsymbol{r}}$. The lack of asterisks $*$ above any quantity in equation (5.4) emphasizes that each quantity in (5.4) is dimensionless. As (5.4) contains two unknowns $E_{n,o}$ and $E_{n,i}$, we turn to the dimensionless form of equation (5.2), which is $E_{n,o} - SE_{n,i} = q$. This equation is applied by substituting the inner perpendicular field $E_{n,i}$ into (5.4), which yields

$$\begin{aligned} \frac{S-1}{4\pi S} \oint_A \frac{\boldsymbol{r} \cdot \boldsymbol{n}(\boldsymbol{x})}{r^3} E_{n,o}(\boldsymbol{y}) dA(\boldsymbol{y}) + \frac{S+1}{2S} E_{n,o}(\boldsymbol{x}) \;\; &= \;\; \boldsymbol{E}^\infty \cdot \boldsymbol{n}(\boldsymbol{x}) - \\ &\frac{1}{4\pi S} \oint_A \frac{\boldsymbol{r} \cdot \boldsymbol{n}(\boldsymbol{x})}{r^3} q(\boldsymbol{y}) dA(\boldsymbol{y}) + \frac{1}{2S} q(\boldsymbol{x}). \end{aligned} \tag{5.5}$$

If the surface charge density q is given at an instant in time, the right–hand side of (5.5) is a known quantity. This is indeed the case, as we assume an uncharged interface $q = 0$ at time $t = 0$. Hence, the interfacial charge evolution equation (5.3) is not needed at this stage, and it is possible to solve for

the normal field $E_{n,o}$ at this instant.

Once the normal electric fields $E_{n(i,o)}$ are calculated from (5.2) and (5.5), the tangential field $E_{t,o} = E_{t,i}$ remains unknown. The tangential field may be obtained via an integral formulation of Laplace's equation in terms of the electrostatic potential ϕ_o:[61]

$$\phi_o(\boldsymbol{x}) = \phi^{\infty}(\boldsymbol{x}) + \oint_A \frac{1}{4\pi r}(E_{n,o}(\boldsymbol{y}) - E_{n,i}(\boldsymbol{y}))dA(\boldsymbol{y}). \tag{5.6}$$

The tangential field is computed according to $E_{t,o} = -\frac{\partial \phi_o}{\partial s}$, where s is a tangential coordinate measured from the positive z–axis. From the solution to the normal and tangential electric fields, the jump in electrical stress at the interface is readily calculated by evaluating the Maxwell stress tensor $\boldsymbol{\tau}^*_{e(i,o)} = \varepsilon_{i,o}\left(\boldsymbol{E}^*_{i,o}\boldsymbol{E}^*_{i,o} - \frac{1}{2}E^{*2}_{i,o}\boldsymbol{I}\right)$, where $\boldsymbol{I}$ is the identity tensor. Once normalized by $\varepsilon_o E^2_{\infty}$, the jump in electrical stress (from out to in) across the interface is given by

$$\begin{aligned}[\boldsymbol{\tau}_e \cdot \boldsymbol{n}] \;\; &= \;\; \frac{1}{2}\left[(E^2_{n,o} - SE^2_{n,i}) + (S-1)E^2_{t,o}\right]\boldsymbol{n} \\ &\quad + E_{t,o}(E_{n,o} - SE_{n,i})\,\boldsymbol{t} = \Delta p_E \boldsymbol{n} + qE_{t,o}\boldsymbol{t}.\end{aligned} \tag{5.7}$$

Equation (5.7) is a general condition that assumes that the electrical relaxation timescales $\tau_{e(i,o)}$ may take on arbitrary values. Assuming that charge relaxation and charge convection in (5.3) become vanishingly small ($\tau_{e(i,o)} \to 0$), the charge conservation equation (5.3) results in $E_{n,i} - RE_{n,o} = 0$. Substituting for $E_{n,i}$ in equation (5.7) yields the jump in electrical stress derived by Lac and Homsy[48] (equation (2.7) in that paper). Following their notation, we refer to the normal component Δp_E in (5.7) as the electric pressure, while the tangential component $qE_{t,o}$ is responsible for the induction of steady–state

recirculatory fluid flow within the drop and throughout the medium. Note, however, that we cannot implement equation (2.7) in Lac and Homsy[48] due to our consideration of charge relaxation and charge convection. Instead, we make use of (5.7) to calculate the jump in electrical stress at the surface of the drop.

5.3.2 Fluid flow

The tangential electrical stresses (5.7) exerted at the interface are balanced by viscous stresses, thus resulting in fluid flow. To compute the resulting interfacial velocity profile, we assume zero–Reynolds–number flow. For the drop size and applied fields in our experiments, the Reynolds numbers $Re_{Flow(i,o)}$ are $O(1)$. However, Feng and Scott[46] showed that computations at Reynolds numbers of order unity provided little difference in the steady deformation from those predicted under creeping flow. Also, as shown in the following sections, our computations reach a steady–state deformation close to that of the experimental measurements. This provides an a posteriori validation of our creeping flow assumption. Here, the interfacial fluid velocity may be expressed in terms of an integral equation, which reads in dimensionless form[62]

$$\begin{aligned} \boldsymbol{u}_o(\boldsymbol{x}) \;=\; & -\frac{1}{4\pi(M+1)} \oint_S \Delta\boldsymbol{f}(\boldsymbol{y}) \cdot \boldsymbol{J}(\boldsymbol{y},\boldsymbol{x})\, dS(\boldsymbol{y}) \\ & -\frac{1}{4\pi}\frac{M-1}{M+1} \oint_S \boldsymbol{u}_o(\boldsymbol{y}) \cdot \boldsymbol{K}(\boldsymbol{y},\boldsymbol{x}) \cdot \boldsymbol{n}(\boldsymbol{y})\, dS(\boldsymbol{y}), \end{aligned} \tag{5.8}$$

where $\boldsymbol{J}$ and $\boldsymbol{K}$ denote the free–space Green's functions for velocity and stress, respectively.[62] The dimensionless jump in hydrodynamic traction $\Delta\boldsymbol{f}$ across the surface is given by

$$\Delta\boldsymbol{f} = \frac{2\,\kappa_m\,\boldsymbol{n}}{Ca_o} - \left[\boldsymbol{\tau}_e \cdot \boldsymbol{n}\right], \tag{5.9}$$

where κ_m represents the mean curvature and $[\boldsymbol{\tau}_e \cdot \boldsymbol{n}]$ is the jump in electrical stress in (5.7). Knowledge of $\boldsymbol{u}_o$ from solving (5.8) now permits updating the interfacial charge through the charge conservation equation (5.3), which reads in dimensionless form as

$$\frac{\partial q}{\partial t} = \frac{E_{n,i}}{R} - E_{n,o} - Re_o \, \nabla_s \cdot (\boldsymbol{u}_o q), \tag{5.10}$$

where $Re_o = \varepsilon_o \chi_o U/a = E_\infty^2 \varepsilon_o^2 \, \chi_o/\mu_o$ designates the electric Reynolds number based on the medium properties. This dimensionless group represents the ratio of charge relaxation $\tau_{e,o} = \varepsilon_o \chi_o$ to flow $\tau_f = a/U$ timescales.

Following Feng,[47]

$$\nabla_s \cdot (\boldsymbol{u}_o q) = \frac{dq(\boldsymbol{u}_o \cdot \boldsymbol{t})}{ds} + \frac{q \boldsymbol{u}_o \cdot \boldsymbol{e}_\sigma}{\sigma} \tag{5.11}$$

for our coordinate system, where $\boldsymbol{e}_\sigma$ is a basis vector in the $\boldsymbol{\sigma}$–direction (radial). Furthermore, the position of the interface is updated by integrating the kinematic condition

$$\frac{\partial \boldsymbol{\xi}}{\partial t} = Re_o \, \boldsymbol{u}_{n,o}, \tag{5.12}$$

where $\boldsymbol{u}_{n,o} = (\boldsymbol{u}_o \cdot \boldsymbol{n}) \, \boldsymbol{n}$ and $\boldsymbol{\xi}$ denotes the positions of a set of marker points placed on the surface of the drop. The time–dependent quantities q and $\boldsymbol{\xi}$ may be updated by a time–stepping scheme, as explained below.

5.3.3 Numerical scheme

We impose an initially uncharged interface ($q = 0$ throughout), and consecutively solve the integral equations (5.5), (5.6), and (5.8) via the boundary element method. Thereafter, the time–dependent conditions (5.10) and (5.12) are integrated through a second order Runge–Kutta method, while assuring

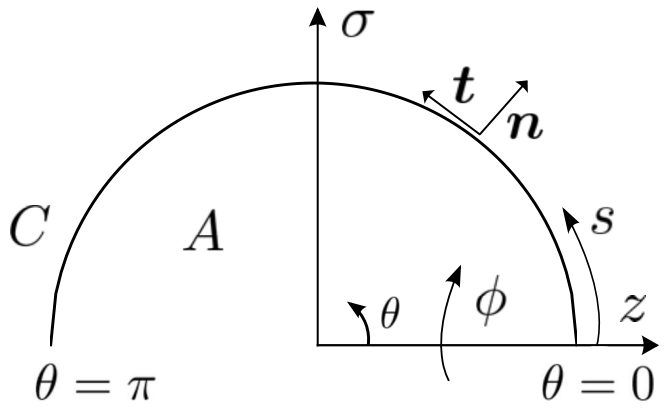

Figure 5.2: Computational diagram of the initial drop shape. As the field and flow are considered axisymmetric, the integral equations (5.5), (5.6), (5.8) are reduced from integrals along the surface A to integrals along the contour C. Here, the normal $\boldsymbol{n}$ and tangential $\boldsymbol{t}$ vectors are illustrated; the former is positive when pointing outwards, while the latter is positive when pointing in the counter–clockwise direction, respectively. Finally, the continuous arc–length s, which begins from the positive z–axis ($\theta = 0$), is positive when pointing in the counter–clockwise direction.

that the step–size Δt is maintained small enough such that the volumetric flow–rate across the interface $\oint_S \boldsymbol{u}_{n,o}\, dS$ is at most $O(10^{-6})$. The field and flow are assumed axisymmetric, which permits analytical integration of the integrands in (5.5), (5.6), and (5.8) over the azimuth, thus reducing the surface integrals to line integrals along the drop contour C (see figure 5.2). Thus, the tangential coordinate s corresponds to the continuous arc–length along the surface of the drop measured from the positive z–axis in the counter–clockwise direction. The axisymmetric free–space Green's functions $\boldsymbol{J}$ and $\boldsymbol{K}$ in (5.8) are computed in terms of elliptic integrals of the first and second kind, respectively. These are extracted from the open–source library BEMLIB.[61]

The top half of the drop ($0 \leq \theta \leq \pi$) is partitioned into N segments, typically ranging from $N = 100 - 200$, for which all functions are interpolated by piecewise–continuous cubic polynomials (splines) parametrized with respect to

the continuous arc–length s. Following Lac and Homsy,[48] these polynomial representations may possess either vanishing first or second derivatives at the endpoints ($\theta = 0, \pi$). Implementing either one of these conditions for the unknown functions provides enough information to solve the boundary integral equations (5.5), (5.6), (5.8). Note that we do not assume symmetry with respect to the plane $z = 0$. Following standard regularization techniques,[61] the logarithmically singular terms in these kernels are subtracted from the main integrals, thus rendering the integrands regular as the observer $\boldsymbol{y}$ approaches the source point $\boldsymbol{x}$. Subsequently, the singularity is added back and integrated. The regular integrals in (5.5), (5.6), (5.8) are then broken up into integrals along each segment, each of which is calculated by implementing Gauss–Legendre quadrature; the remaining singular integrals are computed by utilizing Gauss–Legendre quadrature for integrals that posses logarithmic singularities.[61] All simulations are conducted until the normal velocity $u_{n,o}$ at every node is at most $O(10^{-4})$, such that steady–state is reached and no subsequent appreciable changes occur in the calculated quantities throughout time.

5.4 Computations for transient deformation

The impacts of charge relaxation and charge convection on transient drop deformation are first probed separately. Our focus is on the transient deformation; however, comparison of the attained steady–state against values reported in the literature provides a useful check of our computations.

5.4.1 The effect of charge relaxation

We first examine the influence of the charging term $\frac{\partial q}{\partial t}$ in (5.10), while still focusing on the limit of negligibly small electric Reynolds numbers $Re_{i,o} \to 0$. Here, convection of charge by the flow becomes negligible. In this limit, (5.10)

yields the interfacial charging condition

$$E_{n,i} - RE_{n,o} = R\frac{\partial q}{\partial t}. \tag{5.13}$$

Here, the electrical relaxation timescales $\tau_{e(i,o)} = \varepsilon_{i,o}\chi_{i,o}$ are considered nonzero, although small in comparison with the flow timescale $\tau_f = a/U$. The interface acquires a surface charge q over the timescales $\tau_{e(i,o)}$, similar to the RC time constant of a capacitor. Note that although the convective term is neglected in equation (5.10), the effect of the electric Reynolds number Re_o is preserved through the kinematic condition (5.12). This dimensionless group may be rewritten as $Re_o = Ca_o \frac{\tau_{e,o}}{\tau_{c,o}}$, where $\tau_{c,o} = \mu_o a/\gamma$ represents the capillary timescale based on the medium properties. Here, $\tau_{e,o}/\tau_{c,o}$ is the ratio of timescales $\tau_{e,o}/\tau_p$ defined by Saville[15] that characterizes the transport of charge towards the interface, with the process timescale $\tau_p = \tau_{c,o}$. Hence, we label this ratio of timescales $\tau_{e,o}/\tau_{c,o}$ as a Saville number Sa_o. To compare our computational results against published literature results for steady deformation, we focus on the particular set of dimensionless parameters (S, M, R) = (20, 1, 0.5), which was examined by Lac and Homsy,[48] and corresponds to a drop that is less conductive than the medium and fluids that possess viscosities equal to one another. Note that for this set of values ($SR > 1$), the steady–state conformation is oblate. The electric capillary number is held at $Ca_o = 0.5$. To probe the influence of a varying charging timescale $\tau_{e,o}$, the transient deformation is examined as $Sa_o = \tau_{e,o}/\tau_{c,o}$ is varied over two orders of magnitude.

The transient deformation corresponding to $Sa_o = \{0.1, 1, 10\}$ and $Ca_o = 0.5$ is illustrated in figure 5.3. All three curves achieve a steady deformation

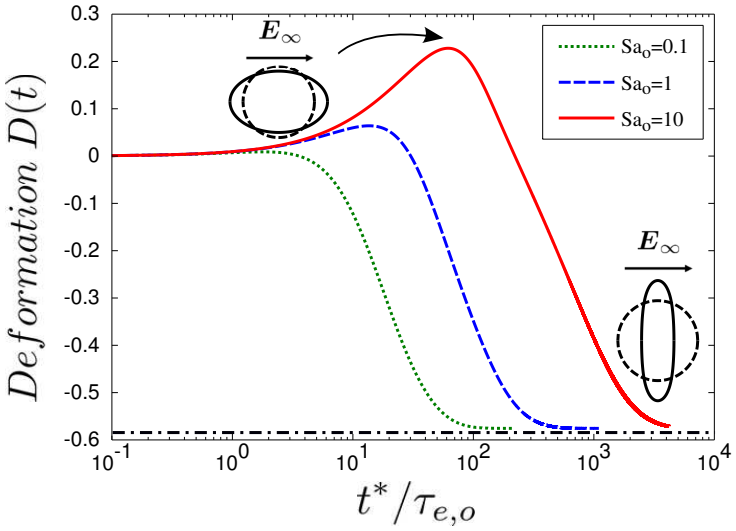

Figure 5.3: Transient deformation $D(t)$ as a function of dimensionless time for different ratios of charging $\tau_{e,o}$ to capillary $\tau_{c,o}$ timescales, which we label as a Saville number Sa_o. The capillary number $Ca_o = 0.5$ and the set of dimensionless parameters (S, M, R) = (20, 1, 0.5) correspond to one of the cases analyzed by Lac and Homsy.[48] Here, time t^* is normalized by the electrical relaxation timescale $\tau_{e,o}$ of the dotted curve describing $Sa_o = 0.1$. The shape of the drop possessing the largest transient prolate deformation ($Sa_o = 10$, the solid curve) and its steady oblate deformation shape (applicable to all three curves) are also shown. The dash–dotted line represents the steady–state reported by Lac and Homsy.[48]

of $D = -0.58$ (denoted by the dash–dotted line), in agreement with Lac and Homsy.[48] For this set of parameters, Taylor's $O(Ca)$ theory would predict an oblate deformation D_T of magnitude greater than unity, which is clearly incorrect. Approaching the same steady–state value for the deformation as Lac and Homsy confirms that our numerical method has been implemented properly. Unlike Lac and Homsy,[48] however, we also compute the entire transient deformation profile, which displays nonmonotonic behavior. In particular, an increasingly pronounced prolate–oblate shape transition is observed as Sa_o increases. As described by Supeene *et al.*[21] and Lanauze *et al.*,[55] an increasing charging timescale $\tau_{e,o}$ extends the amount of time for charge to reach the interface. Thus, at early times, both phases behave as perfect dielectrics; hence, the drop deforms along the applied field (prolate) due to the absence of sufficient induced electrohydrodynamic flow. Eventually, enough charge reaches the interface to drive the recirculatory flow and promote a change in configuration, thus yielding the expected ultimate oblate deformation. As Sa_o is increased, the shape transition becomes more pronounced, in terms of the maximum transient prolate deformation; it also becomes more long–lived, in terms of the amount of time during which the shape remains prolate. It takes the solid curve describing $Sa_o = 10$ more than an order of magnitude longer to reach steady–state in comparison to the dotted curve corresponding to $Sa_o = 0.1$.

5.4.2 The effect of charge convection

We now consider the effects of charge relaxation and charge convection. As a basis for comparison, we focus on a system for which $(S,\ M,\ R) = (0.5,\ 1,\ 100)$, studied by Feng.[47] In figure 7 of that paper, Feng plots the steady deformation for this system as a function of the square of the applied

dimensionless electric field, namely $E_\infty^2 \varepsilon_f a/\gamma$, where the field is normalized by performing a balance of electrical stress $\varepsilon_f E_\infty^2$ and interfacial stress γ/a. Here, ε_f is the permittivity of free space. In that figure, two curves, which correspond to zero and finite electric Reynolds number, respectively, indicate that charge convection suppresses the steady oblate deformation at a given electric field strength. At an electric capillary number $Ca_o = 2$ (a dimensionless electric field squared of 0.4 in Feng's paper), the simulation that does not consider charge convection is unable predict a stable drop shape; the computation that is conducted at a nonzero electric Reynolds number $Re_o = 0.7$ predicts a steady oblate conformation. Note that our definition for $Re_{i,o}$ differs from that of Feng.[47] While we separately define an electric Reynolds number $Re = \varepsilon\chi U/a$ for each phase, Feng defines this dimensionless group as $Re_{\text{Feng}} = (\varepsilon_i + \varepsilon_o)\chi_i\chi_o U_{\text{Taylor}}/(\chi_i + \chi_o)a$, where U_{Taylor} is expressed as the maximum interfacial angular velocity derived by Taylor.[13]

We predict the exact same behavior as Feng[47] when comparing our simulations with and without charge convection. Additionally, we report the development towards the steady–state shape. Figure 5.4 depicts the transient deformation for these two conditions, where the dashed and solid curves correspond to computational results in the limit of electric Reynolds number $Re_o \to 0$ and $Re_o = 0.7$, respectively. Although these two curves follow the same behavior at early times (roughly $t = t^*/\tau_{e,o} < 10$), the dashed curve begins to diverge from the solid curve when $t \approx 10$ and finally predicts drop breakup, while the solid curve predicts a steady–state deformation of $D = -0.23$.[47] Achieving the same steady configuration as predicted by Feng indicates that proper numerical implementation of charge convection has been achieved. As described by Feng,[47] the stabilization of oblate drops due to charge convection results

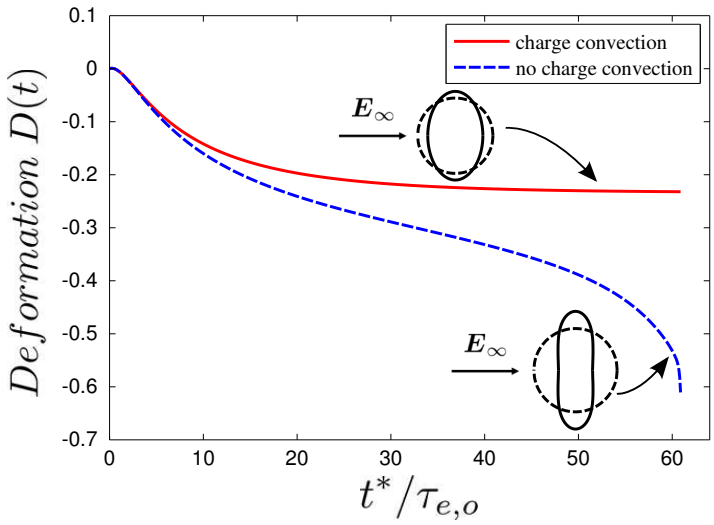

Figure 5.4: Transient deformation $D(t)$ as a function of dimensionless time $t = t^*/\tau_{e,o}$. The capillary number $Ca_o = 2$ and $(S,\ M,\ R) = (0.5,\ 1,\ 100)$. Both curves account for charge relaxation ($\frac{\partial q}{\partial t}$ in equation (5.10)). The solid curve, however, results from a simulation that also includes charge convection (an electric Reynolds number $Re_o = 0.7$), while the dashed curve is obtained in the limit $Re_o \to 0$. Here, we display the final shape of the drop corresponding to the simulation conducted at finite Re_o, which achieves a steady deformation. The shape resulting from the simulation carried out at $Re_o \to 0$ is shown right before the onset of numerical instability ($t \approx 60$).

from the weakened tangential flow resulting from the distorted surface charge density profile, which we will discuss further later.

5.5 Comparison of computation against experiment

5.5.1 Experimental procedure

Two 5×5 cm brass electrodes are attached to either side of a plastic cell, which holds the fluids, at a separation of 2 cm. A 1.9 cm diameter hole is made through the bottom of the cell to allow illumination with a fiber optic illuminator (Fiber–Lite MI–152, Dolan–Jenner Industries). A drop of silicone oil (Sigma–Aldrich) is injected into a castor oil (Sigma–Aldrich) medium from

a 25 μL glass syringe with a 22 gauge needle. A potential difference is applied across the two electrodes using a high–voltage power supply (Gamma High Voltage Research, Inc.). As soon as the field is applied, images are recorded at a rate of 15 frames per second with a firewire camera (Guppy PRO F–125B, Allied Vision Technologies) until the drop deformation reaches steady–state. All image analyses are subsequently conducted with ImageJ software. Our experimental setup is similar to that of Salipante and Vlahovska.[18]

To accurately predict the deformation of leaky dielectric systems, precise measurement of the fluid properties is crucial.[16] Here, the permittivity ε and resistivity χ of each phase is measured via electrochemical impedance spectroscopy.[63] The viscosity μ of each fluid is measured using a cone–and–plate rheometer (D–HR 2 rheometer, TA Instruments). Finally, the interfacial tension of the castor oil–silicone oil interface is extracted from the experimental work of Salipante and Vlahovska.[18] These material properties are listed in table 5.1. The greatest source of measurement error originates from the voltage measurement. For this purpose, a high–voltage probe (80K–15, Fluke Corporation) is implemented in conjunction with a standard digital multimeter (HHM29, Omega Engineering, Inc.). The error in measurement of the applied voltage is 2.25% (based on accuracy of the probe and multimeter). This error does not significantly change the results of any of our computational predictions. Given that we expect possible losses of voltage, we use the lower bound of the confidence in applied voltage in our computations. A minimum of six measurements of the transient drop deformation are taken per field strength. The transient deformation is then repeatedly measured for a different drop of approximately the same size and voltage to assess for reproducibility between different drops. All measurements produced a similar result for the transient

Phase	ε_r	$1/\chi$ (S/m)	μ (Pa S)	a (mm)	γ (mN/m)
drop (silicone oil)	2.8	2.0×10^{-12}	0.05	2.0	4.5
medium (castor oil)	4.9	5.8×10^{-11}	0.68		

Table 5.1: Dimensional parameters for a silicone oil drop suspended in a castor oil medium. Here, ε_r denotes the relative permittivity.

drop deformation. A representative measurement of deformation for each field strength at a fixed size is presented in this work to display the error in the deformation due to measurement of the drop semi–axes. Note that we display this uncertainty because it is larger than the standard deviation that arises from the repeated measurement of the transient deformation.

5.5.2 Transient deformation at an electric field strength of 1.6 kV/cm

The experimental castor oil–silicone oil system is described in table 5.1. For this set of parameters, all steady–state configurations are oblate. The correspondent dimensionless groups are listed in table 5.2. The viscosity ratio M is less than unity; i.e. the drop is less viscous than the suspending medium. The capillary numbers $Ca_{i,o}$ are $O(10^{-1})$, while the Saville numbers $Sa_{i,o}$ and electric Reynolds numbers $Re_{i,o}$ are greater than unity. Here, $Sa_{i,o} > 1$ and $Re_{i,o} > 1$ represent a dominance of the electrical relaxation timescales $\tau_{e(i,o)}$ over the capillary $\tau_{c(i,o)} = \mu_{i,o} a/\gamma$ and flow $\tau_f = a/U$ timescales, respectively. Thus, the transient and steady–state behavior are controlled by the transport of charge towards and along the interface, i.e. we expect charge relaxation and charge convection to be relevant. The dimensionless groups in table 5.2 are implemented in our computations.

Phase	Ca	Sa	Re	S	M	R
drop (silicone oil)	0.3	605.3	158.2			
				0.6	0.1	29.2
medium (castor oil)	0.5	2.6	1.2			

Table 5.2: Dimensionless groups that describe a drop of silicone oil suspended in a castor oil medium at an electric field strength of 1.6 kV/cm. See table 5.1 for dimensional quantities.

The experimental measurement of the deformation throughout time is depicted by the open circles in figure 5.5. The error bars in this curve originate from the measurement of the major r_2^* and minor r_1^* semi–axes, handled using standard propagation of error. The $O(Ca)$ theory of Lanauze *et al.*[55] that considers the charge relaxation $\tau_{e(i,o)}$ and momentum diffusion $\tau_{m(i,o)} = a^2\rho_{i,o}/\mu_{i,o}$ timescales is shown as the dashed curve. Note that this theory yields the steady–state deformation D_T predicted by Taylor.[13] Due to the fact that $\tau_{e(i,o)} \gg \tau_{m(i,o)}$ for this experimental system (assuming that $\rho_o = \rho_i \approx 960$ kg/m^3), considering the momentum relaxation timescales $\tau_{m(i,o)}$ makes no difference in predicting the development of the drop shape; i.e. transient inertia is irrelevant and the flow is essentially quasi–steady. The theory captures the initial prolate–oblate shape transition during early times $t^* \lesssim 0.5\,\mathrm{s}$, before diverging from the experimental measurement and overpredicting the steady deformation.

The remaining curves in figure 5.5 result from boundary integral calculations. The simulation that considers neither charge relaxation nor charge convection is implemented by making use of equation (5.13) and decreasing the resistivities $\chi_{i,o}$ by two orders of magnitude for use in (5.12), while still maintaining the resistivity ratio $R = \chi_i/\chi_o$ unchanged. The result from this calculation is shown as the dotted curve in figure 5.5. This curve is unable to capture the shape transition, instead predicting a monotonic development towards a steady–state deformation that overpredicts the deformation measured in the experiment.

The dash–dotted curve in figure 5.5 results from a simulation that only takes charge relaxation into account through equation (5.13). This curve ex-

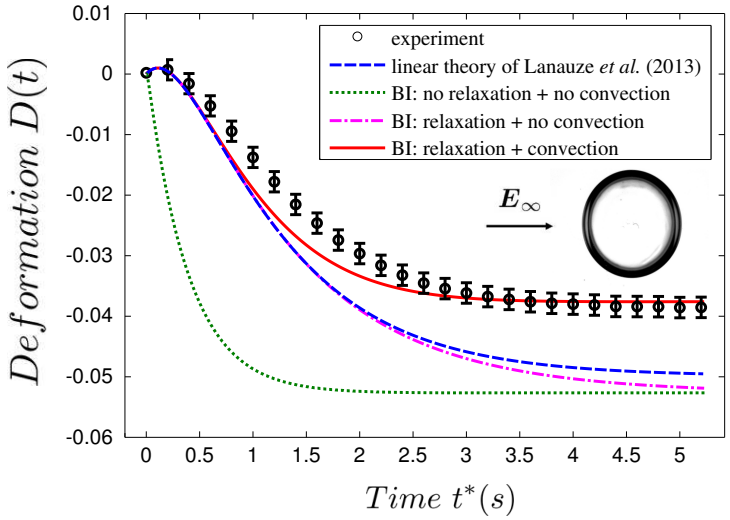

Figure 5.5: Transient deformation of a silicone oil drop suspended in a castor oil medium at a field strength of 1.6 kV/cm. The dimensional parameters for this system are listed in table 5.1 and the dimensionless groups are listed in table 5.2. The open circles denote the experimental measurement, while the dashed curve illustrates the small–Ca theory of Lanauze *et al.*[55] that accounts for charge relaxation. The remaining curves result from boundary integral calculations. The dotted curve results from a simulation that considers an instantaneous interfacial charging with no charge convection, while the dash–dotted curve results from a simulation that considers finite electrical relaxation timescales $\tau_{e(i,o)} = \varepsilon_{i,o}\chi_{i,o}$ with no charge convection. Finally, the solid curve results from a simulation that accounts for charge relaxation together with charge convection. The inset is an image of the steady oblate shape measured experimentally.

hibits similar transient behavior to the $O(Ca)$ theory of Lanauze *et al.*[55] during times $t^* \lesssim 2\,\mathrm{s}$, which is unsurprising since they both account for charge relaxation (equation (5.13)). The dash–dotted curve eventually reaches the same steady–state as the dotted curve that considers instantaneous charge relaxation and no charge convection. When the capillary number is not small, we expect the $O(Ca)$ theory to deviate from this computational prediction (dash–dotted curve). It is merely a coincidence that the $O(Ca)$ prediction is actually closer to the steady–state experimental measurement than the boundary integral calculation; the latter should provide a more accurate result at the capillary numbers $Ca_i = 0.3$ and $Ca_o = 0.5$ considered. The fact that this calculation is unable to capture the experimental curve together with the large electric Reynolds numbers $Re_{i,o}$ (table 5.2) leads us to consider the full charge–transport equation (5.10). The solid curve depicted in figure 5.5 results from a simulation that considers both charge relaxation and charge convection. Although slight deviation from the experiment is observed during intermediate times $0.5\,\mathrm{s} \lesssim t^* \lesssim 2.5\,\mathrm{s}$, this computation provides a more accurate representation of the experimentally–measured transient deformation (within the calculated error). Hence, both charge relaxation and charge convection in (5.10) must be accounted for when predicting time–dependent drop deformation for such low–conductivity systems with large electrical relaxation timescales $\tau_{e(i,o)}$, such that $Sa_{i,o} > 1$ and $Re_{i,o} > 1$. Note that although the deformations illustrated in figure 5.5 are small, the nonlinear effect of charge convection still plays a role in determining the steady–state deformation. This is a central conclusion of our work.

Phase	Ca	Sa	Re	S	M	R
drop (silicone oil)	0.4	605.3	263.0			
				0.6	0.1	29.2
medium (castor oil)	0.8	2.6	2.0			

Table 5.3: Dimensionless groups that describe a drop of silicone oil suspended in a castor oil medium at an electric field strength of 2.1 kV/cm.

5.5.3 Transient deformation at an electric field strength of 2.1 kV/cm

The electric field is increased to 2.1 kV/cm, yielding the dimensionless parameters in table 5.3. The electric capillary $Ca_{i,o} = \varepsilon_{i,o} E_\infty^2 a/\gamma$ and electric Reynolds $Re_{i,o} = E_\infty^2 \varepsilon_{i,o}^2 \chi_{i,o}/\mu_{i,o}$ numbers have increased due to their proportionality to E_∞^2, while the Saville numbers $Sa_{i,o}$ remain unchanged. The resulting experimental measurement and computational curves for this set of parameters are displayed in figure 5.6. The description for each of these curves is the same as in figure 5.5. Since larger capillary numbers $Ca_{i,o}$ are considered, the $O(Ca)$ theory of Lanauze *et al.*[55] shows a greater deviation at steady–state from the boundary integral simulations and the experimental measurement. Note that the dash–dotted curve (only charge relaxation) has not yet reached steady–state in figure 5.6; it eventually settles towards the same steady deformation as the dotted curve (no charge relaxation or convection). Although the same trend is observed in the extent of agreement of the set of boundary integral calculations with the experimental measurement, the curves that are not able to capture the transient deformation profile measured in the experiment overpredict the steady–steady state deformation by a more substantial amount in comparison to figure 5.5. This is due to the more pronounced effect of charge convection, which is reflected through the increase in electric Reynolds numbers $Re_{i,o}$ due to the larger applied voltage.

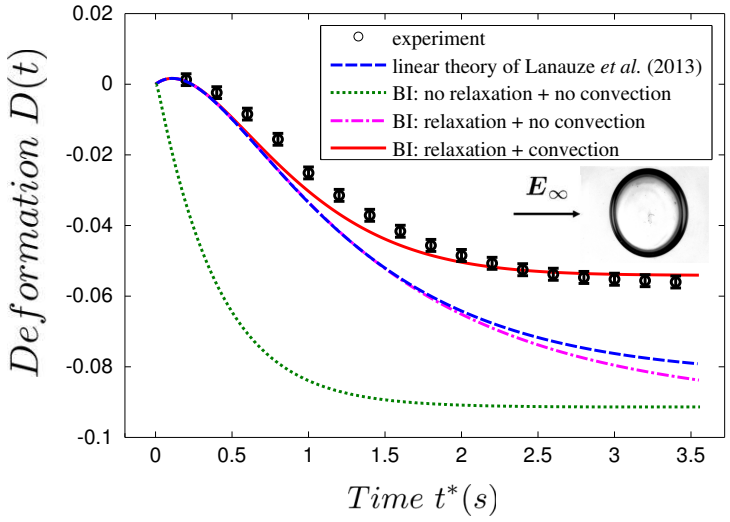

Figure 5.6: Transient deformation of a silicone oil drop suspended in a castor oil medium at a field strength of 2.1 kV/cm. The dimensional parameters for this system are listed in table 5.1 and the dimensionless groups are listed in table 5.3. The description of the curves is the same as in figure 5.5. The inset is an image of the steady oblate shape measured experimentally.

To understand why charge convection suppresses steady oblate deformations, we examine the surface charge density profile along the interface of the drop. Figure 5.7(a) shows the steady–state ($t^* \approx 3\,\mathrm{s}$ in figure 5.6) dimensionless interfacial charge q as a function of the polar angle θ. As we assumed symmetry with respect to the azimuth ϕ (see figure 5.2), analyzing the results for the top half of the drop yields all necessary information to investigate the effects of surface charge convection. The dashed curve in figure 5.7(a) results from the simulation that does not take charge convection into account (equation (5.13)), while the solid curve considers the full governing equation (5.10) for charge transport. Here, the magnitude of the surface charge density q is lessened throughout the regions away from the equator ($\theta = \pi/2$) due to convection of charge from pole to equator. Convection of charge is also observed to cause a rapid variation in q at the equator of the drop. As the scaling for the electrical stress is given by $[\boldsymbol{\tau}_e \cdot \boldsymbol{n}] \sim qE_\infty$, the pronounced reduction in q leads to a decrease in the electrical stress. Due to the fact that oblate configurations are driven by an induced electrohydrodynamic flow, a simple balance of electrical and viscous stresses yields $U \sim qE_\infty a/\mu \sim \varepsilon E_\infty^2 a/\mu$. This relationship dictates that the decrease in $[\boldsymbol{\tau}_e \cdot \boldsymbol{n}]$ provides a suppression of the flow strength U that drives the deformation. This is illustrated in figure 5.7(b), where the tangential velocity $u_{t,o} = u_{t,i} = \boldsymbol{u}_{i,o} \cdot \boldsymbol{t}$ is presented as a function of the polar angle θ for the cases where charge convection is considered (solid line) and neglected (dashed line). Here, a weakening of the tangential flow is present throughout the regions of reduced interfacial charge q. This reasoning helps understand the difference between the simulated steady deformations that do and do not account for surface convection of charge in figure 5.6. Note that the magnitude of the steady–state charge $\int_S q\,dS = \int_C 2\pi q\sigma\,dC$ that resides

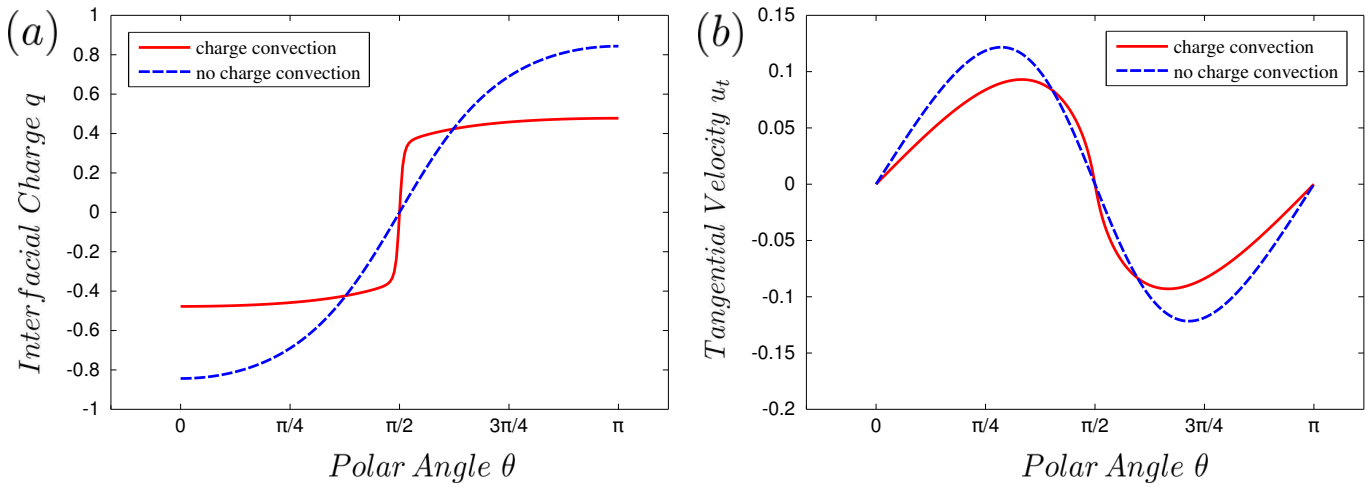

Figure 5.7: (a) Steady interfacial charge density profile q as a function of the polar angle θ corresponding to a silicone oil drop suspended in a castor oil medium at a field strength of 2.1 kV/cm ($t^* \approx 3$ s in figure 5.6). The solid curve results from the simulation that considers surface charge convection from the poles ($\theta = 0, \pi$) towards the equator ($\theta = \pi/2$) of the drop; the dashed curve does not account for interfacial charge convection. (b) Steady interfacial tangential velocity u_t (note that $u_{t,o} = u_{t,i}$) as a function of the polar angle θ ($t^* \approx 3$ s in figure 5.6). The solid curve results from the simulation that considers surface charge convection towards the equator of the drop; the dashed curve does not account for interfacial charge convection.

at each half of the drop decreases with increasing electric Reynolds numbers $Re_{i,o}$. When charge convection is accounted for, charge swept from pole to equator by the induced electrohydrodynamic flow is neutralized at the equator. Hence, the overall amount of charge on each half of the drop is reduced.

We now examine the development of the two steady surface charge density profiles q displayed in figure 5.7(a). Figure 5.8(a) illustrates the evolution of interfacial charge that yields the steady–state depicted by the dashed curve in figure 5.7(a), while figure 5.8(b) illustrates the evolution of interfacial charge that yields the steady–state depicted by the solid curve in figure 5.7(a). In figure 5.8(a), the four curves present a gradual development towards the steady charge density profile. Here, all curves qualitatively display a $\cos(\theta)$ depen-

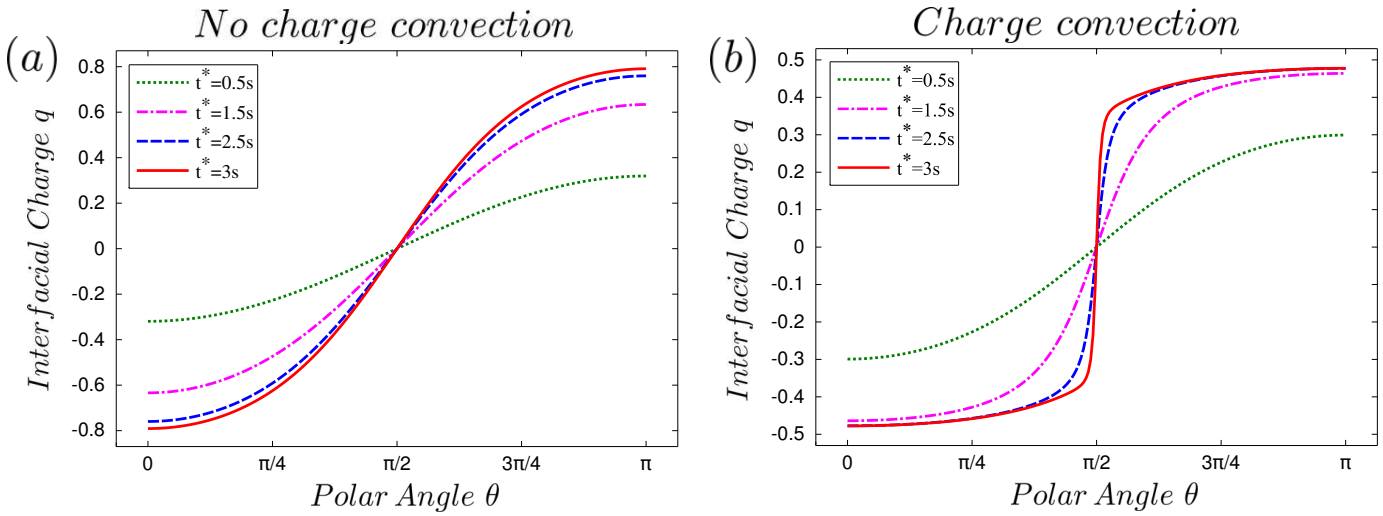

Figure 5.8: Development of the interfacial charge density profile q as a function of the polar angle θ for a silicone oil drop suspended in a castor oil medium at a field strength of 2.1 kV/cm. (a) The set of curves corresponds to the simulation for transient deformation that accounts for charge relaxation and does not consider charge convection in figure 5.6 (the dash–dotted curve), which eventually yields the same steady–state surface charge density distribution as the dashed curve in figure 5.7(a). (b) The set of curves corresponds to the simulation for transient deformation that accounts for both charge relaxation and charge convection in figure 5.6 (the solid curve), which eventually yields the same steady–state surface charge density distribution as the solid curve figure 5.7(a).

dence that results due to charge accumulating at the interface without any convection by the fluid flow. If convection of charge by the induced electrohydrodynamic flow is accounted for, the flow sweeps the accumulating charge from pole to equator (figure 5.8(b)). Here, the maximum in surface charge q increases at the poles as time progresses. Simultaneously, the previously–described sharp variation in q occurs at the equator due to charge convection from pole to equator. As the electric Reynolds numbers $Re_{i,o}$ increase at high electric field strengths, the governing equation for interfacial charge (5.10) becomes approximately hyperbolic. Thus, there exists the possibility of a "charge shock," in which the surface charge distribution displays nearly discontinuous behavior at the equator, as illustratd in figure 5.8(b) for $t^* = 3\,\mathrm{s}$.

Phase	Ca	Sa	Re	S	M	R
drop (silicone oil)	3.8	605.3	2.3×10^3			
				0.6	0.1	29.2
medium (castor oil)	6.6	2.6	17.7			

Table 5.4: Dimensionless groups that describe a drop of silicone oil suspended in a castor oil medium at an electric field strength of 6.1 kV/cm.

5.5.4 Transient deformation at an electric field strength of 6.1 kV/cm

The electric field is further increased to 6.1 kV/cm, which provides the dimensionless groups listed in table 5.4. The electric capillary $Ca_{i,o}$ and electric Reynolds $Re_{i,o}$ numbers have increased by approximately an order of magnitude in comparison with table 5.3. The results for this system are presented in figures 5.9(a) and 5.9(b). In figure 5.9(a), only the experimental measurement of the transient deformation, the boundary integral simulation that considers charge relaxation and charge convection through equation (5.10), and the $O(Ca)$ theory of Lanauze *et al.*[55] are displayed. Although the deformation in the experiment reaches steady–state around time $t^* \approx 3$ s, the simulation only reaches $t^* \approx 0.8$ s, at which time the normal velocity $u_{n,o}$ in equation (5.12) is $O(10^{-3})$. The computation is only shown until this point in time. From this point forth $u_{n,o}$ increases, eventually predicting an unstable drop conformation. The $O(Ca)$ theory is displayed until $t^* \approx 0.75$ s as a basis for comparison against the other curves. The curve corresponding to the linear theory begins to deviate from the computation and experiment around $D = -0.02$, and ends with a large overprediction of the steady deformation measured experimentally ($D_T = -0.72$, not shown).

The surface charge density q as a function of the polar angle θ correspond-

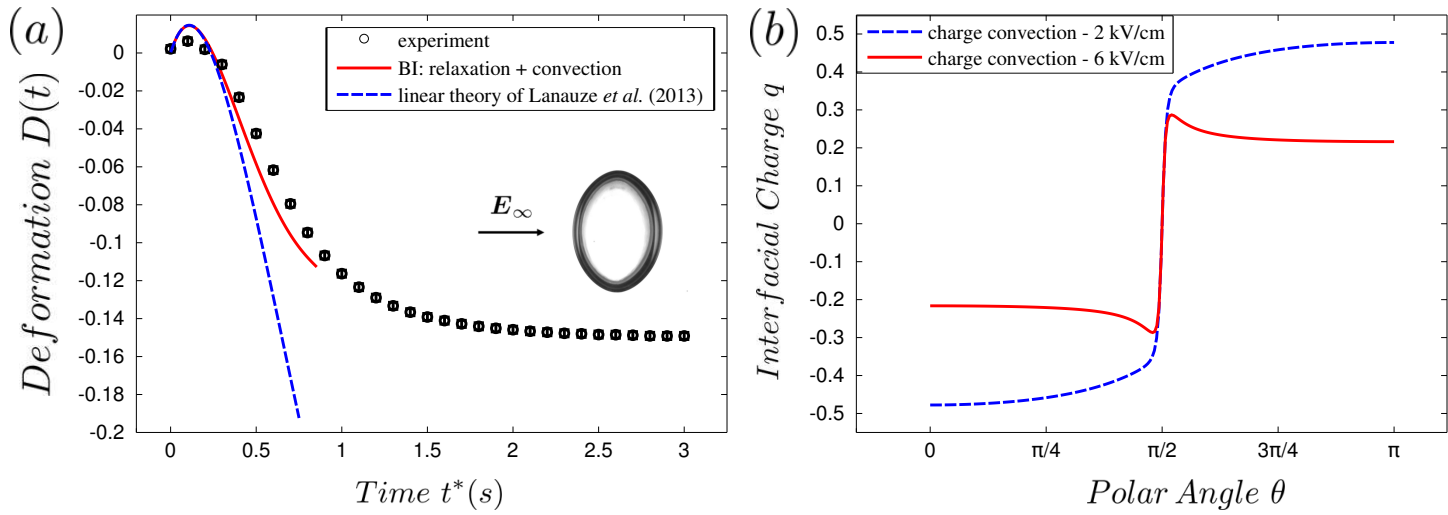

Figure 5.9: (a) Transient deformation of a silicone oil drop suspended in a castor oil medium at a field strength of 6.1 kV/cm. The dimensional parameters for this system are listed in table 5.1 and the dimensionless groups are listed in table 5.4. The open circles denote the experiment, while the dashed curve illustrates the small–Ca theory of Lanauze *et al.*[55] that considers charge relaxation. Finally, the solid line represents the boundary integral simulation that accounts for both charge relaxation and charge convection through equation (5.10). The inset is an image of the steady oblate shape measured experimentally. (b) Interfacial charge density profile q as a function of the polar angle θ. The solid curve results from the simulation corresponding to a field strength of 6.1 kV/cm ($t^* \approx 0.8$ s in figure 5.9(a)), which considers surface charge convection from the poles ($\theta = 0, \pi$) towards the equator ($\theta = \pi/2$) of the drop. The dashed curve accounts for charge convection at field strength of 2.1 kV/cm, which results in a steady–state profile (note that this is the same curve as the solid curve in figure 5.7(a)).

ing to the approximate point of instability of the computation, $t^* \approx 0.8\,\mathrm{s}$ in figure 5.9(a), is illustrated through the solid curve in figure 5.9(b). The dashed curve is exactly the same as the solid curve in figure 5.7(a), which considers charge convection and is able to predict the steady–state deformation displayed by the solid curve in figure 5.6 at a lower field strength of $2.1\,\mathrm{kV/cm}$. Although a sharp variation in q was previously observed in figure 5.7(a) at the equator of the drop at a field of $2.1\,\mathrm{kV/cm}$ due to interfacial charge convection directed from pole to equator, this abrupt change is further accentuated when the field is increased to $6.1\,\mathrm{kV/cm}$. Furthermore, this increase in field strength provides a maximum in the magnitude of the interfacial charge distribution q near the equator, thus providing a nonmonotonic surface charge density profile. If the simulation were to proceed beyond $t^* \approx 0.8\,\mathrm{s}$, the sharp variation at the equator and the maximum in q would both increase until the curve ceases to be smooth and the simulation terminates.

We believe that the solid curve in figure 5.9(b) is an artifact of the imposed axisymmetry of the boundary integral calculation. At a high enough electric field strength, an onset of drop rotation and three–dimensional flow is expected due to an electric torque exerted to restore the misaligned dipole that arises in systems for which $\tau_{e,i} > \tau_{e,o}$.[17,18] Hence, axisymmetric oblate deformations are unstable to three–dimensional instabilities at high electric fields.[15] This phenomenon is akin to Quincke rotation for a solid particle suspended in a fluid.[64] To check whether this critical voltage for the onset of rotation has been reached, we calculate the threshold electric field for a solid particle,[65]

$$E_Q = \sqrt{\frac{2\mu_o S(2R+1)^2}{3\varepsilon_i \varepsilon_o \chi_o R(RS-1)}}, \tag{5.14}$$

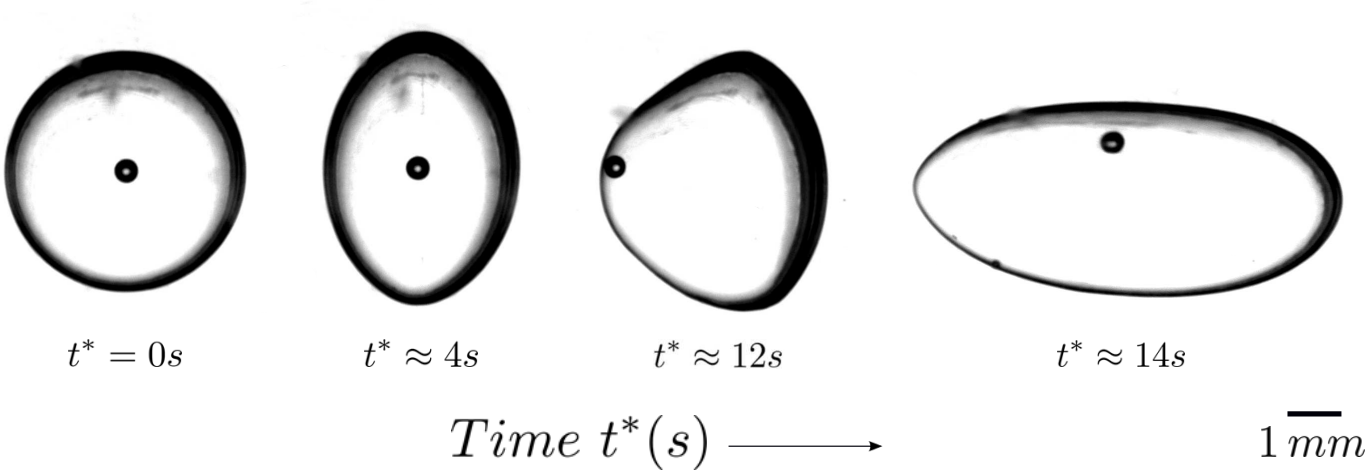

Figure 5.10: Onset of rotation and three–dimensional flow of a silicone oil drop suspended in a castor oil medium at a field strength of 6.8 kV/cm. An air bubble is present inside of the drop. This bubble does not affect the experimental measurement; it allows the direction of flow to be traced.

where E_Q denotes the critical electric field for the onset of Quincke rotation of a solid particle. Equation (5.14) is obtained by balancing the electrical and viscous torques on a spherical rigid object. It is independent of particle size since both the electrical and viscous torques scale as a^3. We implement this expression as an approximation; considerable experimental deviation from (5.14) has been observed for low–viscosity drops,[17,18] which is the regime of our experiments ($M = 0.1$). Inserting the dimensional parameters from table 5.1 and the dimensionless groups S, M, R from table 5.2 yields $E_Q = 3.2\,\mathrm{kV/cm}$. For our system, the experimental onset of rotation occurs at a threshold field strength of approximately 6.8 kV/cm – only 0.7 kV/cm greater than the field strength in figure 5.9 – which is closer to the threshold electric fields reported in the literature[17,18] for castor oil–silicone oil systems. As illustrated in figure 5.10, such three–dimensional instabilities may occur for deformations of modest amplitude. Here, the sequential images illustrate the silicone oil drop acquiring an oblate shape and then transitioning towards an unstable configuration.

5.6 Conclusion

We have analyzed the nonlinear transient deformation of a leaky dielectric drop of permittivity ε_i, resistivity χ_i, and viscosity μ_i suspended in a medium with permittivity ε_o, resistivity χ_o, and viscosity μ_o, respectively. Our first contribution was the calculation of the transient deformation via an axisymmetric boundary integral method, which accounts for surface charge convection and a finite relaxation timescale for interfacial accumulation of charge. For steady oblate drops, the dominant electrical relaxation timescales $\tau_{e(i,o)} = \varepsilon_{i,o}\chi_{i,o}$ yielded an initial prolate configuration due to a lack of sufficient charge at the interface,[21,55] which in turn causes the drop and medium to initially behave akin to perfect dielectrics. As the ratio of charge relaxation to capillary timescale (Saville number $Sa_o = \tau_{e,o}/\tau_{c,o}$) increased at a fixed capillary number Ca_o, the prolate conformation became more pronounced and long–lived, while the steady–state deformation remained unchanged. Furthermore, charge convection was shown to restrain steady oblate deformations.

Our second contribution was a direct comparison of numerical simulation against experimental measurement with no adjustable parameters. Our focus on oblate drops was due to their flow–driven nature, which therefore accentuates interfacial charge convection.[47] Both charge relaxation and charge convection were required to correctly quantify the time–dependent deformations measured experimentally. Furthermore, these two forms of surface charge transport were found to operate simultaneously rather than serially (see figure 5.8(b)); that is, charge accumulates at the interface as the electrohydrodynamic flow convects the charge from pole to equator. Good agreement was observed for moderate electric field strengths (1.6 kV/cm, 2.1 kV/cm). How-

ever, the computation failed as the field increased towards 6.1 kV/cm, which is due to an onset of drop rotation and unsteady three–dimensional flow.[17,18] Although the oblate deformations illustrated in figures 5.5 and 5.6 were moderate, charge convection provided a strong nonlinear effect on the interfacial charge distribution q, as illustrated in figures 5.7(a) and 5.9(b). We have not encountered such distorted surface charge density profiles in published works that consider the effects of interfacial charge convection on steady oblate electrohydrodynamic drop deformation,[47,49] which we believe is due to the lack of any reported results at such high electric Reynolds numbers $Re_{i,o} = \tau_{e(i,o)}/\tau_f$. This effect, which mostly reduced q throughout the interface, translates to a less–pronounced tangential flow u_t (figure 5.7(b)), and thus a reduced oblate deformation. Thus, the modest deformations measured experimentally required a nonlinear model to enable an accurate prediction.

Our boundary integral calculations enabled the prediction of the transient deformation of the castor oil–silicone oil system in tables 5.2 and 5.3; however, room for improvement of the experimental setup exists. The most substantial issue in our system is the dielectrophoretic migration of silicone oil drops at high electric field strengths. Although care was taken when injecting the drop into the center of the cell, we believe that more careful alignment of the electrodes would minimize the migration of these drops, and improve agreement between our computations and the experiments in figures 5.5 and 5.6. Our work emphasizes the need to consider both charge relaxation and charge convection when modeling the transient deformation of leaky dielectric systems at large Saville $Sa_{i,o}$ and electric Reynolds $Re_{i,o}$ numbers. The significant effects of these two phenomena serves as motivation to perform further experimental and computational studies that consider a wider range of systems with dif-

fering permittivity S, resistivity R, and viscosity M ratios. Finally, a fully three–dimensional boundary integral simulation would prove useful in predicting steady–state drop deformation at higher electric fields, as well as the exact field strength at the onset of drop rotation and unsteady flow observed in experiments.[17,18]

6. Relaxation or breakup of a low–conductivity drop upon removal of a uniform DC electric field

6.1 Introduction

As stated in the Introduction of this thesis, the dynamics of "leaky dielectric" materials under electric fields are of recent interest in areas of soft matter physics such as vesicle manipulation,[4,66–69] interfacial self–assembly of colloidal particles,[6,70–72] electrorheological response of polymer blends,[38,73–75] and field–induced dynamics of pendant and sessile drops.[76–79] To gain insight into the response of these relatively complicated systems to electric fields, it is essential to first quantify the timescales and occurring dynamics of simple systems, such as a single isolated drop placed under a uniform DC electric field. The modeling of the transient field–induced deformation of isolated weakly conductive drops has received continued attention.[19,21,54–56,80] For these low–conductivity systems, the charge relaxation timescales $\tau_{e(i,o)} = \varepsilon_{i,o}\chi_{i,o}$, which characterize the time over which the interface acquires its steady–state surface charge den-

sity distribution q^*, are often comparable to other system timescales and must be accounted for. Note that the superscript $*$ is implemented to identify a dimensional variable; material properties contain no superscripts. The ratios of charge relaxation timescales $\tau_{e(i,o)}$ to the flow timescale $\tau_f = a/U$ are labeled as the electric Reynolds numbers $Re_{i,o} = \tau_{e(i,o)}/\tau_f$.[14] Here, U represents a characteristic velocity scale. When the electric Reynolds numbers are $O(1)$, the induced EHD flow convects charge as it accumulates at the drop surface. This interfacial charge convection provides an intricate coupling between the electric field and fluid flow; it has been shown to strengthen prolate deformations and weaken oblate deformations.[47,49] It has also been shown to drive "charge shocks" in the surface charge density profile of oblate drops,[80] where a rapid variation in the charge density occurs near the equator. Large charge relaxation timescales $\tau_{e(i,o)}$ relative to the capillary timescales $\tau_{c(i,o)} = \mu_{i,o}a/\gamma$ delay interfacial charging,[15] which in turn extends the transient deformation process.[21,54,55,80] Increasingly large values of $\tau_{e(i,o)}/\tau_{c(i,o)}$ also cause prolate to oblate shape transitions for ultimate oblate configurations.[21,55,80] We labeled the ratios of $\tau_{e(i,o)}$ to capillary timescales $\tau_{c(i,o)}$ as Saville numbers[15] $Sa_{i,o}$ in our previous publication.[80] Our work examined the role of transient interfacial charging and surface charge convection on transient EHD drop deformation. There, we analyzed the effects of finite $Sa_{i,o}$ and $Re_{i,o}$ via experiment and computation. Accounting for charge relaxation and charge convection was crucial to correctly predict our experimental measurements for the transient oblate deformation of a silicone oil drop suspended in a castor oil medium.

The impact of charge transport towards and along the interface is dictated by the magnitude of the electrical relaxation timescales $\tau_{e(i,o)}$ relative to other system timescales. This in turn determines the appropriate retention

of terms in the governing equation dictating the conservation of interfacial charge. For example, vesicle systems normally possess a high membrane resistivity in comparison to their surrounding salt solutions.[4,66,68] This in turn yields fast charging timescales $\tau_{e(i,o)}$ in comparison to the membrane capacitive timescale $\tau_b = C_b L(\chi_i + 0.5\chi_o)$, where C_b is the biomimetic membrane capacitance and L denotes a characteristic lengthscale (typically the vesicle radius). Since $\tau_{e(i,o)}/\tau_b \ll 1$, transient charging of the surrounding fluids is negligible in comparison to charging of the membrane capacitor; hence, fluid charge relaxation is negligible. Furthermore, charge convection is normally neglected for these systems since at steady–state, tangential electrical stresses are balanced by interfacial tension gradients[4,66,68] as opposed to viscous stresses; no fluid flow is induced at the membrane surface. On the other hand, the weakly conductive fluids implemented in the present study are characterized by electrical relaxation timescales $\tau_{e(i,o)}$ that may be on the order of the capillary $\tau_{c(i,o)}$ and flow τ_f timescales. This in turn renders relevance to the transient interfacial charging and surface charge convection mechanisms, respectively.

Since charge relaxation affects the time–dependent deformation of a weakly conducting drop exposed to an electric field, we expect it to play a major role in the relaxation of a drop upon removal of the field. While the relaxation of a drop upon cessation of a flow field is well studied,[20,81–83] the relaxation of a drop upon cessation of an electric field has received scant attention. Importantly, the presence of an additional (charging) timescale under an electric field suggests that the drop relaxation dynamics should be rich. Therefore, in the present chapter, we analyze the relaxation of a prolate leaky dielectric drop upon removal of a uniform DC electric field via theory, computation, and experiment. This work is therefore an extension of our previous publication;[80]

here, we examine the effect of surface charge transport on drop relaxation upon removal of an applied electric field. In our experimental system, consisting of a castor oil drop suspended in silicone oil, we observe an asymmetry between the transient deformation and relaxation processes: the drop relaxes faster than the rate at which it achieves its steady deformation. Our computations reveal that the asymmetry in the deformation–relaxation profile arises from an interfacial tangential electrical stress that acts together with the capillary stress to quickly restore the shape of the drop back to a sphere once the applied field is removed; this differs from the deformation process in which the electrical stress and capillary stress counteract one another. Furthermore, we present computational results for a different low–conductivity system for which a highly nonlinear (multi–lobed) steady–state deformation can lead to drop breakup when the electric field is withdrawn; i.e. the drop does not relax back to equilibrium.

6.2 Modeling drop deformation and relaxation

A uniform DC electric field $\boldsymbol{E}_\infty$ is applied across a neutrally buoyant drop suspended in an immiscible medium. The mismatch in permittivity and resistivity between the two phases gives rise to interfacial shear electrical stresses that are balanced by shear viscous stresses; an EHD flow is thus induced throughout the drop and medium. In this work, we consider a drop with greater conductivity than the medium ($R < 1$). We further stipulate the timescale for charge relaxation in the medium $\tau_{e,o} = \varepsilon_o \chi_o$ is greater than that of the drop $\tau_{e,i} = \varepsilon_i \chi_i$ ($SR < 1$). Thus, the rate of charging of the surface is limited by the medium. This yields EHD flows that are directed from the equator ($\theta = \pi/2$) towards the poles ($\theta = 0, \pi$) of the drop (equator–to–pole)[18,48] (figure 6.1). Here, the field–induced dipole is along the imposed electric field

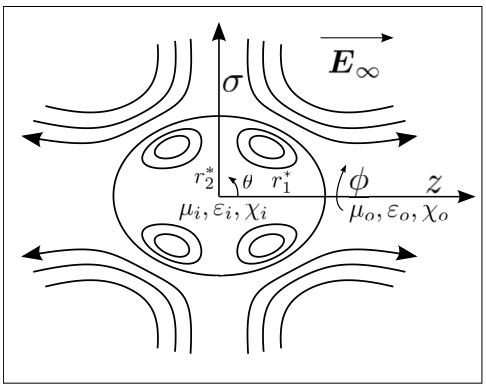

Figure 6.1: Schematic of the prolate deformation of a leaky dielectric drop under a uniform DC electric field of magnitude E_∞. The drop is characterized by permittivity ε_i, resistivity χ_i, and viscosity μ_i, while the medium is characterized by properties ε_o, χ_o, and μ_o, respectively. The permittivity $S = \varepsilon_i/\varepsilon_o$ and resistivity $R = \chi_i/\chi_o$ ratios chosen in this work yield a flow directed from the equator ($\theta = \pi/2$) towards the poles ($\theta = 0, \pi$) of the drop, as illustrated by the depicted streamlines. A cylindrical coordinate system (σ,ϕ,z) is implemented due to the assumed axisymmetric nature of the field and flow. Here, r_1^* and r_2^* represent the major and minor semi–axes, while θ denotes the polar angle.

and the field–induced deformation is prolate. The drop deformation is assumed to be independent of the azimuthal angle ϕ. This axisymmetry permits the use of a cylindrical coordinate system (σ,ϕ,z). Once a steady–state deformation is achieved, the electric field is removed, allowing the interface to discharge and the drop to relax back to its spherical equilibrium shape, or to undergo breakup.

We solve for both the electric field and fluid flow profiles at the surface of the drop once the uniform field E_∞ is applied at time $t_d^* = 0$. Here, t_d^* is the elapsed time for the deformation process. The transient drop deformation $D(t_d^*)$ is then quantified from the calculated interfacial field and flow. Once a steady–state deformation is achieved, the field $\boldsymbol{E}_\infty$ is set to zero, and the drop is allowed to relax (or break up). The transient deformation and drop relaxation are first quantified through asymptotic analysis valid in the

linear regime (i.e. to first order in $Ca_{i,o}$). The drop deformation–relaxation process is then quantified through boundary integral computations capable of predicting linear and nonlinear deformations. Unlike previous researchers who have implemented the boundary integral method to calculate the steady–state field–induced deformation of liquid drops,[9,45,48,59,60] we account for finite charge relaxation timescales $\tau_{e(i,o)}$ through an equation that dictates the conservation of surface charge density. Furthermore, we compute the transient drop deformation under an electric field and drop relaxation upon removal of the applied field. The computational results are validated against the linear theory predictions and compared against experimental measurements.

6.2.1 Linear theory

To calculate the transient drop deformation $D(t_d^*)$ when the electric field is applied, we make use of our previously–developed linear theory[55] that considers both the charge relaxation $\tau_{e(i,o)} = \varepsilon_{i,o}\chi_{i,o}$ and momentum relaxation $\tau_{m(i,o)} = a^2\rho_{i,o}/\mu_{i,o}$ timescales, where $\rho_{i,o}$ denotes the density of either phase, respectively. As we shall show in the subsequent sections, our experimental system yields dominant electrical relaxation timescales, for which $\tau_{e(i,o)} \gg \tau_{m(i,o)}$ (note that $\rho_i = \rho_o \approx 960$ kg/m^3). Hence the interfacial charging timescales $\tau_{e(i,o)}$ dictate the temporal evolution of the drop shape; the momentum diffusion timescales $\tau_{m(i,o)}$ do not impact the occurring dynamics of the system. Our analytical expression[55] for the evolution of the drop shape yields Taylor's steady–state linear deformation[13] at long times. This analytical expression is given in the Laplace domain in equation (D4) of our previous article.[55]

To calculate the drop relaxation upon removal of the electric field, we begin with the governing equations for electrostatics. Note that spherical

coordinates ($\zeta = \sqrt{z^2 + \sigma^2}, \theta, \phi$) are implemented to develop our analysis in the linear regime $Ca_{i,o} \ll 1$. Knowledge of the inner ϕ_i^* and outer ϕ_o^* electrostatic potentials requires solutions to Laplace's equation[48,59,60] $\nabla^{*2}\phi_{i,o}^* = 0$. The irrotational electric fields are calculated from the gradient of the potentials. The inner electrostatic potential is bounded at the origin $\zeta = 0$, and the outer field $-\nabla^*\phi_o^*$ approaches zero (note that $\boldsymbol{E}_\infty = 0$ during relaxation) as $\zeta \to \infty$. Furthermore, the potential is continuous across the interface; i.e. $\phi_i^* = \phi_o^*$ at $\zeta = a$. The remaining boundary conditions applied at the drop surface $\zeta = a$ read

$$\varepsilon_o E_{n,o}^* - \varepsilon_i E_{n,i}^* = q^* \tag{6.1}$$

and

$$\frac{1}{\chi_i} E_{n,i}^* - \frac{1}{\chi_o} E_{n,o}^* = \frac{\partial q^*}{\partial t_r^*}, \tag{6.2}$$

where $E_{n(i,o)}^* = \boldsymbol{E}_{i,o}^* \cdot \boldsymbol{n}$ represents the normal component of the electric fields evaluated at the interface, and t_r^* is the time elapsed since the field is removed. Here, the unit normal vector $\boldsymbol{n}$ is positive when pointing into the medium. The boundary condition (6.1) accounts for the jump in electric displacement, while (6.2) dictates the conservation of surface charge density q^*. The right–hand side of equation (6.2) represents the accumulation of interfacial charge q^*,[14,15] which occurs over the electrical relaxation timescales $\tau_{e(i,o)}$.

Following our analytical approach in quantifying transient deformation,[55] we take the Laplace transform of equations (6.1) and (6.2) to eliminate q^* and formulate a new boundary condition. Unlike our previous approach, however, we require the steady–state value for the surface charge density $q_{t_r^*=0}^*$ just before the electric field is removed and the interface begins to discharge. Eliminating

q^* through use of (6.1) and (6.2) yields

$$\widetilde{E}^*_{n,i}\,(1+s^*\tau_{e,i}) = R\,\widetilde{E}^*_{n,o}\,(1+s^*\tau_{e,o}) - q^*_{t^*_r=0}\,\chi_i, \tag{6.3}$$

where the Laplace transform of $E^*_{n(i,o)}$ is given by $\widetilde{E}^*_{n(i,o)} = \int_0^\infty e^{-s^*t^*_r} E^*_{n(i,o)}\,dt^*_r$. After applying the aforementioned boundary conditions to the general solutions for the electrostatic potentials $\phi^*_{i,o}$, the interfacial electrical stresses are readily computed through the Maxwell stress tensor $\boldsymbol{\tau}^*_{e(i,o)} = \varepsilon_{i,o}\left(\boldsymbol{E}^*_{i,o}\boldsymbol{E}^*_{i,o} - \frac{1}{2}E^{*2}_{i,o}\,\boldsymbol{I}\right)$, where $\boldsymbol{I}$ represents the identity tensor. After inversion towards the time domain, the radial and angular jump (from outside to inside) in electrical stress across the surface of the drop is given by

$$[\boldsymbol{\tau}^*_e\cdot\boldsymbol{n}]_\zeta = -\frac{q^{*\,2}_{t^*_r=0}}{\varepsilon_o}\frac{((2S-5)\cos 2\theta - 3)}{4S(S+2)^2\cos\theta}\;e^{-\frac{2(2R+1)}{R(S+2)}\frac{t^*_r}{\tau_{e,o}}} \tag{6.4}$$

and

$$[\boldsymbol{\tau}^*_e\cdot\boldsymbol{n}]_\theta = \frac{q^{*\,2}_{t^*_r=0}}{\varepsilon_o}\frac{\sin\theta}{S(S+2)}\;e^{-\frac{2(2R+1)}{R(S+2)}\frac{t^*_r}{\tau_{e,o}}}, \tag{6.5}$$

where $q^*_{t^*_r=0} = -3\,\varepsilon_o E_\infty \frac{RS-1}{2R+1}\cos\theta$ denotes steady–state surface charge density distribution of a slightly–deformed drop.[55] When the electric field is removed, the interface begins to discharge; the radial and angular jump in electrical stress decays towards zero.

We compute the fluid flow and drop relaxation that result from the electrical stresses (6.4) and (6.5). Our focus is on dominant viscous forces (i.e. Reynolds numbers $Re_{\mathrm{Flow}(i,o)} = \rho_{i,o}Ua/\mu_{i,o} \ll 1$). This requires solution to the Stokes equations

$$\nabla^* p^*_{i,o} = \mu_{i,o}\nabla^{*2}\boldsymbol{u}^*_{i,o} \qquad \text{and} \qquad \nabla^*\cdot\boldsymbol{u}^*_{i,o} = 0, \tag{6.6}$$

where $p^*_{i,o}$ and $\boldsymbol{u}^*_{i,o}$ represent the pressure and velocity distributions. To solve for the velocity and pressure fields, we first implement a stream function $\psi^*_{i,o}(\zeta, \theta, t^*_r)$ from which the velocity profiles are readily calculated through $\boldsymbol{u}^*_{i,o} = \nabla^* \wedge \left[\frac{\psi^*_{i,o}(\zeta,\theta,t^*_r)\boldsymbol{e}_\phi}{\zeta \sin\theta}\right]$. Use of the stream function automatically satisfies the incompressibility constraint. The stream function satisfies the biharmonic equation[32] $D^4\psi^*_{i,o} = 0$, where

$$D^2 = \frac{\partial^2}{\partial\zeta^2} + \frac{\sin\theta}{\zeta^2}\frac{\partial}{\partial\theta}\left(\frac{1}{\sin\theta}\frac{\partial}{\partial\theta}\right). \tag{6.7}$$

The pressure fields $p^*_{i,o}$ are then obtained through solution of the momentum balance in (6.6). The interfacial boundary conditions involve a no–slip condition $u^*_{\theta,i} = u^*_{\theta,o}$, a no–flux condition $u^*_{\zeta,i} = u^*_{\zeta,o} = \frac{\partial\xi^*}{\partial t^*_r}$, a balance between tangential electrical and viscous stresses $[\boldsymbol{\tau}^*_e \cdot \boldsymbol{n}]_\theta + [\boldsymbol{\tau}^*_h \cdot \boldsymbol{n}]_\theta = 0$, and a balance between normal electrical, viscous, and capillary stresses $[\boldsymbol{\tau}^*_e \cdot \boldsymbol{n}]_\zeta + [\boldsymbol{\tau}^*_h \cdot \boldsymbol{n}]_\zeta = \gamma\ \nabla^*_s \cdot \boldsymbol{n}$. Here, $u^*_{\theta(i,o)}$ and $u^*_{\zeta(i,o)}$ denote the angular and radial components of the interfacial velocities $\boldsymbol{u}^*_{i,o}$, ξ^* represents the drop surface, $\boldsymbol{\tau}^*_h = -p^*\boldsymbol{I} + \mu\left[\nabla^*\boldsymbol{u}^* + (\nabla^*\boldsymbol{u}^*)^T\right]$ is the hydrodynamic stress tensor, and ∇^*_s denotes the surface gradient operator. For a detailed explanation of the application of these conditions, see Esmaeeli and Sharifi[19] and Lanauze *et al.*[55] Note that unlike Esmaeeli and Sharifi, we account for transient interfacial charging through equation (6.2). However, the remaining interfacial boundary conditions required to solve for the velocity and pressure fields throughout the drop and medium are the exact same as those considered by Esmaeeli and Sharifi[19] and Lanauze *et al.*[55] We implement these boundary conditions, with distance scaled with the spherical drop radius a, time scaled with the outer charge relaxation timescale $\tau_{e,o} = \varepsilon_o\chi_o$, surface charge density scaled with $\sqrt{\gamma\,\varepsilon_o/a}$, electric field scaled with the characteristic field $E_c = \sqrt{\gamma/a\varepsilon_o}$,

stress scaled with the capillary stress γ/a, and velocity scaled with the capillary velocity $U = \gamma/\mu_o$. Note that the nondimensionalization applied to the field and velocity is derived by balancing the scaling for electrical stress $\varepsilon_o E_c^2$ (for the field) and viscous stress $\mu_o U/a$ (for the velocity) against the scaling for the capillary stress γ/a. This is preferred to any scaling with E_∞ since the applied field is set to zero to allow the drop to relax once it has achieved its steady–state conformation. The scaling for the interfacial charge q^* follows by substituting the scaling for the electric field into $\varepsilon_o E_c$. We omit the remainder of the applied steps and present our analytical expression for the drop relaxation, which reads

$$\begin{aligned} D(t_r) &= [e^{-\frac{40(M+1)t_r Sa_o}{38M^2+89M+48}}\{(q_{t_r=0}/\cos\theta)^2 RSa_o(-19MS+7M-16S+13)+4(S+2)D_T((2M \\ &\quad +3)(19M+16)(2R+1)-20(M+1)R(S+2)Sa_o)\}+(q_{t_r=0}/\cos\theta)^2 RSa_o(M(19S \\ &\quad -7)+16S-13)e^{-\frac{2(2R+1)t_r}{R(S+2)}}]/[4(S+2)((2M+3)(19M+16)(2R+1)-20(M \\ &\quad +1)R(S+2)Sa_o)], \end{aligned} \tag{6.8}$$

where D_T denotes the steady field–induced linear deformation predicted by Taylor.[13] Note that $q_{t_r=0}$ is divided by $\cos\theta$ to eliminate any angular dependence in this expression. An expansion around $t_r = 0$ yields

$$D(t_r) = D_T - \frac{[(q_{t_r=0}/\cos\theta)^2(M(19S-7)+16S-13)+80(M+1)(S+2)^2 D_T]\, Sa_o t_r}{2\,(38M^2+89M+48)\,(S+2)^2} + O(t_r^2). \tag{6.9}$$

Equation (6.9) indicates that once a stable linear deformation D_T is achieved, the rate at which the drop relaxes increases with both the magnitude of D_T and the value of the Saville number Sa_o. As shown in the following sections, our experiments and computations also display this trend.

6.2.2 Boundary integral formulation

The boundary integral method is implemented to solve for the electric field and fluid flow at the surface of the drop, as well as the resulting time–dependent drop deformation $D(t)$. The integral formulation and numerical solution of the differential governing equations for the field and flow are discussed in detail by Lanauze *et al.*[80] Unlike that work, however, charge convection is unaccounted for in the charge conservation equation (6.2), despite the electric Reynolds numbers $Re_{i,o} \sim O(1)$. This is due to the negligible role of charge convection in determining the steady prolate configurations that characterize our experimental system. As we shall see, our computations predict the steady deformations achieved in our experiments within the error in measurement. Hence, this assumption is verified *a posteriori* when comparing computational results against experimental measurements in the following sections. Furthermore, the previously–described nondimensionalization procedure is applied to the subsequent equations.

When the drop achieves a steady–state deformation, its shape ξ^* and surface charge density q^* profiles are extracted. With these numerical values for the steady drop shape and interfacial charge, the capillary numbers $Ca_{i,o}$ are set to zero due to the removal of the uniform applied field $\boldsymbol{E}_\infty = 0$. The boundary integral computations are then conducted in absence of the imposed field to model drop relaxation. Note that all equations henceforth have been rendered dimensionless, as indicated by the lack of the superscript $*$.

We begin with the dimensionless integral formulation of Laplace's equation

for the electric potential, namely[48,59,60,80]

$$\frac{S-1}{4\pi S}\oint_A \frac{\boldsymbol{r}\cdot\boldsymbol{n}(\boldsymbol{x})}{r^3}E_{n,o}(\boldsymbol{y})dA(\boldsymbol{y}) + \frac{S+1}{2S}E_{n,o}(\boldsymbol{x}) = n_z(\boldsymbol{x})\sqrt{Ca_o} \qquad (6.10)$$
$$-\frac{1}{4\pi S}\oint_A \frac{\boldsymbol{r}\cdot\boldsymbol{n}(\boldsymbol{x})}{r^3}q(\boldsymbol{y})dA(\boldsymbol{y}) + \frac{1}{2S}q(\boldsymbol{x}),$$

where the closed integral is evaluated over the interface. Note that (6.10) satisfies all the boundary conditions for the electric field described in section 6.2.1 except for equation (6.2), which remains to be applied. Here, $n_z = \boldsymbol{n}\cdot\boldsymbol{z}$, $\boldsymbol{r} = \boldsymbol{y} - \boldsymbol{x}$ is the distance between an observation point $\boldsymbol{y}$ and a source point $\boldsymbol{x}$, and $r = \sqrt{\boldsymbol{r}\cdot\boldsymbol{r}}$. The instantaneous surface charge density q is required to solve equation (6.10) for the normal field $E_{n,o}$. When the field is initially applied, the surface of the drop contains no charge (i.e. $q = 0$ at time $t_d = 0$). When the field is removed, the steady–state value for the interfacial charge distribution is implemented as the initial condition. The value for q at future times is obtained through numerical time integration of equation (6.2). The instantaneous shape of the drop is required to calculate the surface integrals in equation (6.10) and all equations that follow.

The inner normal electric field $E_{n,i}$ may be calculated through application of (6.1). The tangential field $E_{t,o} = E_{t,i} = E_{i,o}\cdot\boldsymbol{t}$ is acquired via an integral equation that governs the electrostatic potential ϕ_o,[61] which is given by

$$\phi_o(\boldsymbol{x}) = -z(\boldsymbol{x})\sqrt{Ca_o} + \oint_A \frac{1}{4\pi r}(E_{n,o}(\boldsymbol{y}) - E_{n,i}(\boldsymbol{y}))dA(\boldsymbol{y}). \qquad (6.11)$$

The tangential field is $E_{t,o} = -\frac{\partial\phi_o}{\partial s}$, where s represents the continuous drop arc–length measured from the positive z–axis. The jump in electrical stress

(from outside to inside) across the drop surface is

$$[\boldsymbol{\tau}_e \cdot \boldsymbol{n}] = \frac{1}{2}\left[(E_{n,o}^2 - SE_{n,i}^2) + (S-1)E_{t,o}^2\right]\boldsymbol{n} + E_{t,o}(E_{n,o} - SE_{n,i})\,\boldsymbol{t}. \quad (6.12)$$

Note that equation (6.12) differs from (6.4) and (6.5) since those equations are only valid in the linear regime. Equation (6.12) holds regardless of the value of the electric capillary numbers $Ca_{i,o}$.

The field–induced interfacial fluid flow is computed through an integral formulation of the Stokes equations,[62]

$$\begin{aligned} \boldsymbol{u}_o(\boldsymbol{x}) \;=\; & -\frac{1}{4\pi(M+1)}\oint_S \Delta\boldsymbol{f}(\boldsymbol{y})\cdot\boldsymbol{J}(\boldsymbol{y},\boldsymbol{x})\,dS(\boldsymbol{y}) \\ & -\frac{1}{4\pi}\frac{M-1}{M+1}\oint_S \boldsymbol{u}_o(\boldsymbol{y})\cdot\boldsymbol{K}(\boldsymbol{y},\boldsymbol{x})\cdot\boldsymbol{n}(\boldsymbol{y})\,dS(\boldsymbol{y}), \end{aligned} \quad (6.13)$$

where $\boldsymbol{J}$ and $\boldsymbol{K}$ denote the free–space Green's functions for velocity and stress,[62] $\Delta\boldsymbol{f} = 2\,\kappa_m\,\boldsymbol{n} - [\boldsymbol{\tau}_e \cdot \boldsymbol{n}]$ represents the jump in hydrodynamic traction across the interface, and κ_m is the mean curvature. The position of the interface is updated via time integration of the kinematic condition

$$\frac{\partial\boldsymbol{\xi}}{\partial t} = Sa_o\,\boldsymbol{u}_{n,o}, \quad (6.14)$$

where $\boldsymbol{u}_{n,o} = (\boldsymbol{u}_o \cdot \boldsymbol{n})\,\boldsymbol{n}$, $t = t_d$ during the deformation process, and $t = t_r$ during the relaxation process. Once the drop shape ξ and surface charge density distribution q have been updated, equations (6.10) through (6.14) are solved recursively until the drop achieves a steady–state conformation or breaks up. The numerical solution procedure of these equations is discussed in our previous publication.[80]

6.2.3 Validation of numerical computation

To validate our boundary integral computations, we compare the predicted numerical deformation–relaxation profile with the small–Ca theory given in our previous publication[55] that describes the transient drop deformation, and equation (6.8) describing the drop relaxation. The physical system of interest is a drop of castor oil suspended in silicone oil; it is characterized by the material properties listed in table 6.1. The pertinent dimensionless groups extracted from these properties are displayed in table 6.2. Here, the drop is less viscous and more conductive than the medium (i.e. $M < 1$ and $R < 1$). First, we focus on an electric field strength of $E_\infty = 0.5\,\mathrm{kV/cm}$, which yields small capillary numbers $Ca_i = 1.3 \times 10^{-2}$ and $Ca_o = 7.1 \times 10^{-3}$, respectively.

The resulting curves for the transient drop deformation and drop relaxation are presented in figure 6.2(a). Note that all curves begin from time $t^* = 0$ although the drop relaxation occurs after a steady deformation has been achieved; this visualization approach is implemented to emphasize any asymmetry between the deformation and relaxation processes. The horizontal axis time t^* is equal to the deformation time t_d^* for the drop deformation process, and equal to the relaxation time t_r^* for the drop relaxation process. Here, the linear theory for the deformation and relaxation agrees well with our computational predictions. This verifies the numerical predictions since our theory provides accurate results for small capillary numbers $Ca_{i,o}$. Increasing the electric field to $E_\infty = 2.8\,\mathrm{kV/cm}$ yields the capillary numbers $Ca_i = 0.4$ and $Ca_o = 0.2$, respectively. The deformation–relaxation profile in this case is illustrated in figure 6.2(b). As the capillary numbers are increased from those in figure 6.2(a), deviation between the linear theory and computational predictions becomes pronounced. Here, the higher applied field results in de-

formations that are nonlinear in the capillary numbers $Ca_{i,o}$, which the theory is unable to capture.

Phase	ε_r	$1/\chi$ (S/m)	μ (Pa s)	a (mm)	γ (mN/m)
drop (castor oil)	4.9	5.8×10^{-11}	0.68		
				0.5	4.5
medium (silicone oil)	2.8	2.0×10^{-12}	4.80		

Table 6.1: Material properties of a castor oil drop suspended in silicone oil. Here, ε_r denotes the relative permittivity.

Phase	Sa	S	M	R
drop (castor oil)	2.6			
		1.8	0.14	0.03
medium (silicone oil)	22.3			

Table 6.2: Electric–field–independent dimensionless groups that describe a castor oil drop suspended in silicone oil.

6.3 Comparison of numerical computation against experimental measurement

6.3.1 Experimental setup

The present experimental setup is similar to that in our previous publication.[80] A drop of castor oil (Sigma–Aldrich) is injected into a silicone oil (Sigma–Aldrich) medium held by a plastic cell with two 5 cm×5 cm brass parallel electrodes separated at a distance of 2 cm. The permittivity ε and resistivity χ of each fluid is measured via electrochemical impedance spectroscopy.[63] A

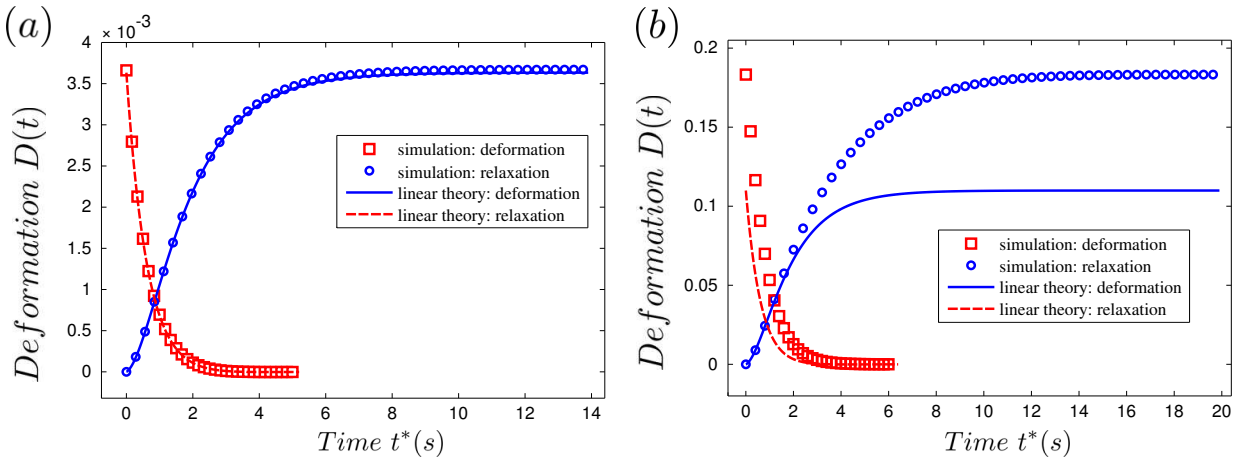

Figure 6.2: Transient deformation and relaxation of a weakly conducting drop. The material properties of this system are listed in table 6.1, while the relevant dimensionless groups are given in table 6.2. The open circles (deformation) and open squares (relaxation) represent boundary integral computations, while solid (deformation[55]) and dashed lines (relaxation, equation (6.8)) denote linear theory calculations. Figure 6.2(a) corresponds to capillary numbers $Ca_i = 1.3 \times 10^{-2}$ and $Ca_o = 7.1 \times 10^{-3}$, while figure 6.2($b$) corresponds to $Ca_i = 0.4$ and $Ca_o = 0.2$, respectively.

voltage is applied across the electrodes using a DC power supply (Gamma High Voltage Research, Inc.). Images of the drop are then collected at a rate of 15 frames per second though a firewire camera (Guppy PRO F–125B, Allied Vision Technologies). When the drop reaches a steady–state deformation, the power supply is switched off, thereby allowing the drop to relax back to its initial equilibrium shape. We analyze the collected images using ImageJ software. The error bars in our measurements of the drop deformation–relaxation profile originate from the uncertainty in measurement of the drop semi–axes r_1^* and r_2^*, respectively. To compare our experimental measurements against computational predictions, the relaxation process is assumed to begin once the deformation deviates from the error corresponding to the steady drop conformation; the preceding measurement is thus considered the initial point in the relaxation profile. Both the experimental and computational curves for

the transient deformation and drop relaxation will be shown from $t^* = 0$ to highlight any asymmetry between the two processes.

6.3.2 Drop deformation and relaxation at electric field strengths of $1.8\,\mathbf{kV/cm}$ and $2.3\,\mathbf{kV/cm}$

We quantify the deformation–relaxation profile of the castor oil–silicone oil system characterized by the properties given in table 6.1 and table 6.2. The applied field $E_\infty = 1.8\,\mathrm{kV/cm}$ yields the capillary numbers $Ca_i = 0.2$ and $Ca_o = 0.1$, respectively. The results for this system are displayed in figure 6.3. Our computations predict the measured drop deformation and relaxation within the experimental error, with some slight deviation between the computation and experiment during $1\,\mathrm{s} \lesssim t^* \lesssim 3\,\mathrm{s}$ for both the deformation and relaxation processes. Furthermore, our computation slightly overestimates the measured steady–state deformation. We believe the deviation occurs due to the dielectrophoretic migration of the castor oil drop, which originates from nonuniformities in the applied field arising from slight tilts in the electrodes.

To verify the neglect of interfacial charge convection in equation (6.2), we compare the computational results illustrated in figure 6.3 against computations that account for charge convection. The results from these computations are depicted in figure 6.4. Although the electric Reynolds number for the drop $Re_i = 1.6$ and medium $Re_o = 2.1$, the curves resulting from computations conducted at these Reynolds numbers exhibit minimal deviation from those conducted at $Re_{i,o} = 0$. From this figure, it is apparent that at this applied field strength, surface charge convection does not play an appreciable role in the transient deformation and drop relaxation processes. This differs from the system we examined in our previous publication[80] (a drop of silicone oil sus-

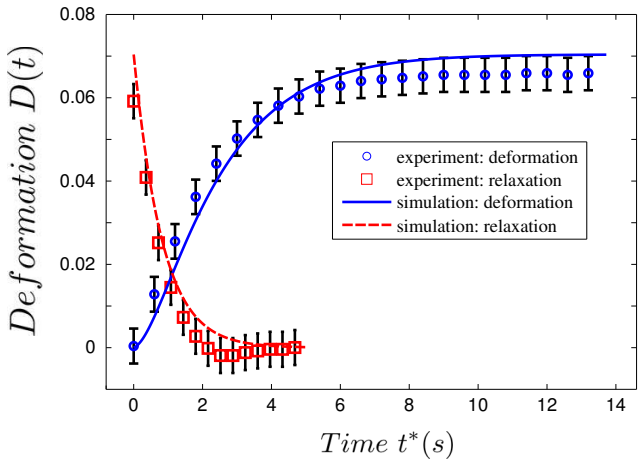

Figure 6.3: Transient deformation and relaxation of a castor oil drop suspended in silicone oil. The material properties of this system are listed in table 6.1, while the relevant dimensionless groups are given in table 6.2. The imposed electric field strength is $E_\infty = 1.8\,\mathrm{kV/cm}$, which yields the capillary numbers $Ca_i = 0.2$ and $Ca_o = 0.1$, respectively. The open circles (deformation) and open squares (relaxation) denote experimental measurements, while solid (deformation) and dashed (relaxation) lines correspond to boundary integral computations.

pended in castor oil) in which higher field strengths were required to achieve modest oblate deformations, thereby yielding larger electric Reynolds numbers (note that $Re_{i,o} \sim E_\infty^2$). Furthermore, we expect charge convection to play a less substantial role for prolate drops since these systems do not require steady EHD flows to drive the drop away from equilibrium. This differs from oblate drops, in which electric field–induced flows are essential to achieve a deformation. To simplify our analysis in the subsequent sections, the remaining systems are modeled under the absence of surface charge convection.

From figure 6.3, it is apparent that the drop quickly relaxes towards its spherical equilibrium shape in comparison to the rate at which it reaches its steady prolate conformation. To quantify this asymmetry between the transient deformation and relaxation processes, we define the ratio $\tau_{\mathrm{on/off}} = t^*_{\mathrm{on}}/t^*_{\mathrm{off}}$. Here, t^*_{on} is the time required for the drop to reach 90% of its steady–state de-

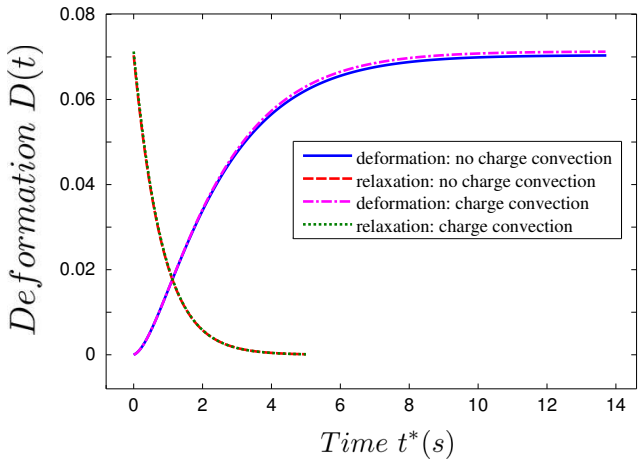

Figure 6.4: Transient deformation and relaxation of a castor oil drop suspended in silicone oil. The material properties of this system are listed in table 6.1, while the relevant dimensionless groups are given in table 6.2. The imposed electric field strength is $E_\infty = 1.8\,\mathrm{kV/cm}$, which yields the capillary numbers $Ca_i = 0.2$ and $Ca_o = 0.1$, respectively. The solid (deformation) and dashed (relaxation) lines denote boundary integral computations conducted in the absence of surface charge convection, while dash–dotted (deformation) and dotted (relaxation) lines correspond to boundary integral computations that account for surface charge convection.

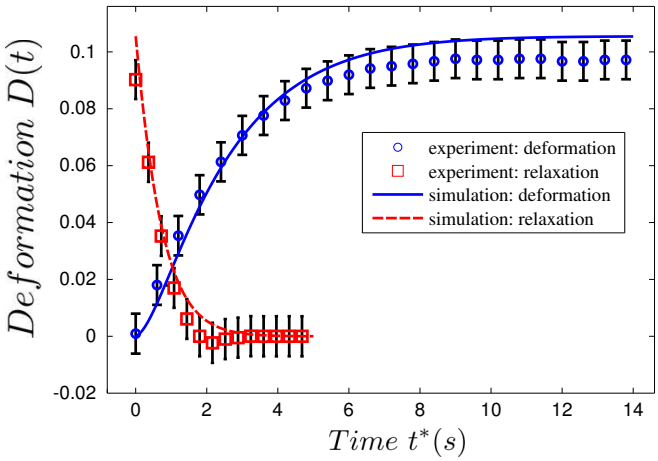

Figure 6.5: Transient deformation and relaxation of a castor oil drop suspended in silicone oil. The material properties of this system are listed in table 6.1, while the relevant dimensionless groups are given in table 6.2. The imposed electric field strength is $E_\infty = 2.3\,\mathrm{kV/cm}$, which yields the capillary numbers $Ca_i = 0.3$ and $Ca_o = 0.2$, respectively. The legend is the same as that in figure 6.3.

formation, while t^*_{off} is the time required for the drop to undergo a 90% loss of its steady deformation. This definition for t^*_{on} and t^*_{off} avoids discerning the specific time when the drop achieves its steady configuration. For this applied field strength, $\tau_{\mathrm{on/off}} = 2.9$. Slightly increasing the electric field to a value $E_\infty = 2.3\,\mathrm{kV/cm}$ yields the deformation–relaxation profile presented in figure 6.5. Here, values for the electric capillary numbers are given by $Ca_i = 0.3$ and $Ca_o = 0.2$, respectively. Our computations are once again able to predict the measured transient deformation and drop relaxation. The increase in $Ca_{i,o}$ provides the accompanying increase in $\tau_{\mathrm{on/off}} = 3.5$.

Since the driving force for the deformation of a low–conductivity drop is the interfacial electrical stress jump $[\boldsymbol{\tau}^*_e \cdot \boldsymbol{n}]$, we expect it to play a major role in the relaxation process of the deformed drop. We thus turn to the dimensionless normal stress balance at the surface of the drop, given by $[\boldsymbol{\tau}_e \cdot \boldsymbol{n}]_n + [\boldsymbol{\tau}_h \cdot \boldsymbol{n}]_n = \nabla_s \cdot \boldsymbol{n}$. When the field $\boldsymbol{E}_\infty$ is applied, both the nor-

mal electrical stress $[\boldsymbol{\tau}_e \cdot \boldsymbol{n}]_n$ and the normal viscous stress $[\boldsymbol{\tau}_h \cdot \boldsymbol{n}]_n$ act to deform the drop, while the capillary stress $\nabla_s \cdot \boldsymbol{n}$ acts to resist any deviation away from the minimum energy configuration provided by the initial spherical shape. The tangential stress balance $[\boldsymbol{\tau}_e \cdot \boldsymbol{n}]_t + [\boldsymbol{\tau}_h \cdot \boldsymbol{n}]_t = 0$ indicates that that the tangential viscous stress $[\boldsymbol{\tau}_h \cdot \boldsymbol{n}]_t$ counteracts the tangential electrical stress $[\boldsymbol{\tau}_e \cdot \boldsymbol{n}]_t$ that induces the EHD flow directed from equator–to–pole (depicted by the tangential velocity profile u_t at $\theta \approx \pi/4$ in figure 6.6(a)). In short, the normal and tangential components of the electrical stress $[\boldsymbol{\tau}_e \cdot \boldsymbol{n}]$ drive the drop away from equilibrium and cause it deform in the direction of the applied field. The main change that occurs when the applied field is removed is a reversal in direction of the interfacial tangential electric field $\boldsymbol{E}_t$, as shown in figure 6.7. Figure 6.7(a) depicts the field lines around the castor oil drop when the steady–state deformation in figure 6.5 is achieved. Note that although the steady deformation displayed in figure 6.5 is nonlinear, the field lines are computed from Taylor's analysis[13] to simply illustrate their direction. The field lines in figure 6.7(b) are computed from our linear theory in section 6.2.1.

Figure 6.7(b) shows that when the electric field is removed, the tangential component of the field at the drop surface $\boldsymbol{E}_t$ increases in magnitude relative to figure 6.7(a) and reverses direction. This change is most pronounced near the equator of the drop. Since the interfacial tangential electrical stress $[\boldsymbol{\tau}_e \cdot \boldsymbol{n}]_t = q\boldsymbol{E}_t$,[48] the change in $\boldsymbol{E}_t$ yields a reversal in the direction of this electrical stress, which is now directed from pole–to–equator. The field–induced tangential flow u_t during the discharging process now favors drop relaxation (figure 6.6(b)). Furthermore, the magnitude of the interfacial flow is large yet short–lived in comparison to the flow achieved at steady–steady when the

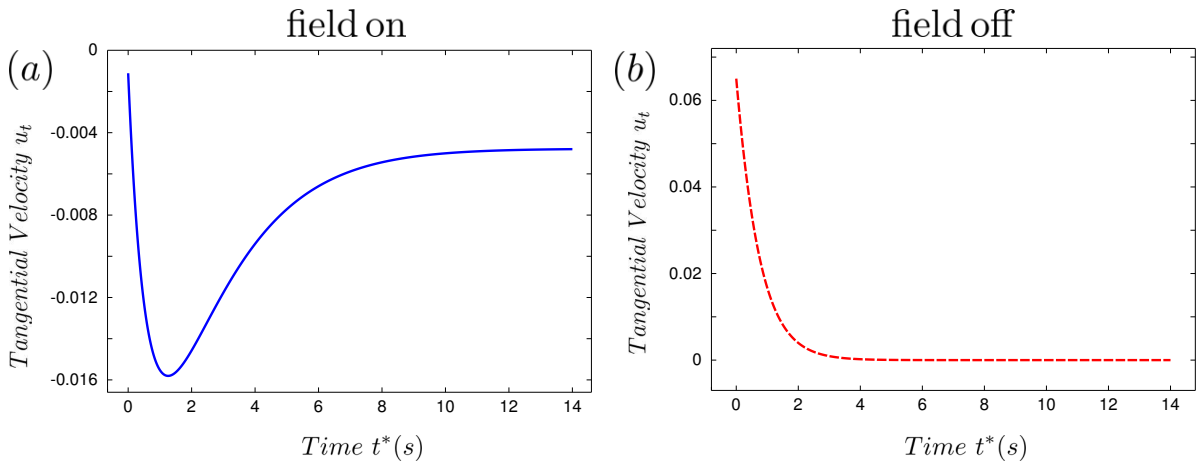

Figure 6.6: Time–dependent dimensionless tangential velocity u_t at the surface of a castor oil drop suspended in silicone oil ($\theta \approx \pi/4$). The imposed electric field strength is $E_\infty = 2.3\,\mathrm{kV/cm}$, which yields the capillary numbers $Ca_i = 0.3$ and $Ca_o = 0.2$, respectively. In figure 6.6(a) the field $\boldsymbol{E}_\infty$ is applied, which yields a development of interfacial velocity directed from equator–to–pole (denoted by the negative sign in u_t) that helps drive the drop deformation depicted by the solid curve in figure 6.5. In figure 6.6(b) the field is removed, which yields a decay in the interfacial velocity directed from pole–to–equator (denoted by the positive sign in u_t) that helps drive the drop relaxation depicted by the dashed curve in figure 6.5.

drop surface is fully charged. This occurs due to the fact that the tangential electrical stress $[\boldsymbol{\tau}_e \cdot \boldsymbol{n}]_t$ and the capillary stress $\nabla_s \cdot \boldsymbol{n}$ both favor drop relaxation, which was not the case then the uniform field was applied. This in turn causes the asymmetry in the deformation–relaxation profile quantified in figure 6.3 and figure 6.5, respectively. Note that if the charging and discharging processes occurred instantaneously, the capillary timescales $\tau_{c(i,o)}$ would dictate the transient drop deformation and drop relaxation, thus yielding a symmetric deformation–relaxation profile. This becomes apparent when applying the limit $\tau_{e,o} \to 0$ to the normal and tangential components of the electrical stress in equations (6.4) and (6.5). Here, the electrical stresses become zero upon removal of the applied field $\boldsymbol{E}_\infty$, which in turn yields no assistance to the capillary stress in the drop relaxation process. Decreasing the

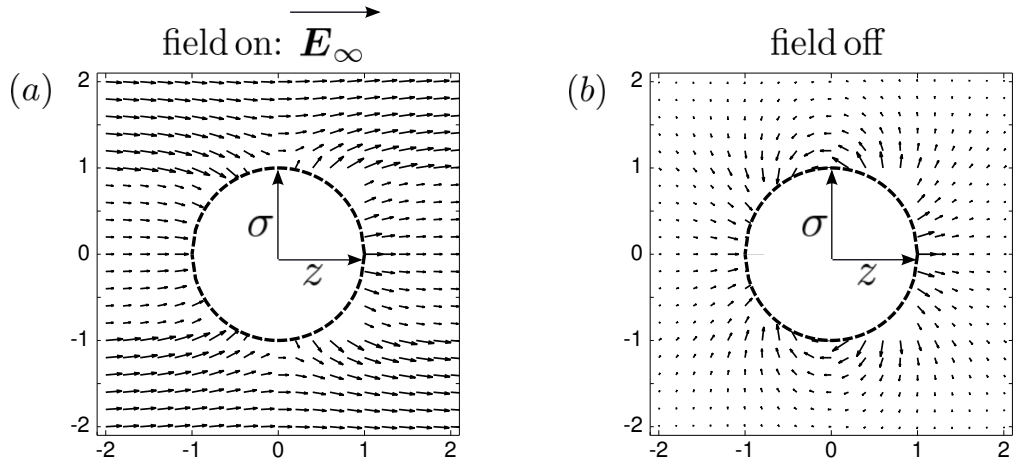

Figure 6.7: Electric field lines outside a castor oil drop suspended in silicone oil. The imposed electric field strength is $E_\infty = 2.3\,\mathrm{kV/cm}$, which yields the capillary numbers $Ca_i = 0.3$ and $Ca_o = 0.2$, respectively. Figure 6.7(a) illustrates the field lines calculated from Taylor's analysis[13] when the steady–state deformation in figure 6.5 is achieved, while figure 6.7(b) depicts the field lines computed from our analysis in section 6.2.1 when the field is removed and the drop is allowed to relax.

charging timescales $\tau_{e(i,o)}$ by two orders of magnitude through decreasing the resistivity χ of each phase for the same system presented figure 6.5 yields the computational deformation–relaxation profile illustrated in figure 6.8. Here, the dimensionless ratio $\tau_{on/off}$ is decreased from $\tau_{on/off} = 3.5$ (figure 6.5) to $\tau_{on/off} = 1.4$. Since the dimensionless groups $\{S, M, R\}$ and capillary numbers $Ca_{i,o}$ remain unaltered from those in figure 6.5, we conclude that the decrease in Saville numbers $Sa_{i,o}$ (or equivalently, a decrease in the resistivities of the fluids) is solely responsible for the decrease in asymmetry between the drop deformation and relaxation processes. As previously stated, removing the electric field yields a reversal in the interfacial tangential electrical stress. To observe an asymmetry in the drop deformation–relaxation profile, the charging timescales $\tau_{e(i,o)}$ should be $O(1)$ relative to the capillary timescales $\tau_{c(i,o)}$. This allows the tangential electrical stress to act over a longer period of time to assist in the drop relaxation process towards equilibrium.

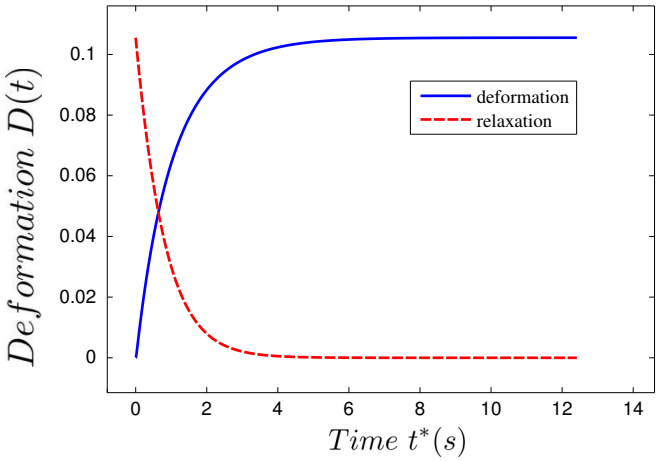

Figure 6.8: Transient deformation and relaxation of a castor oil drop suspended in silicone oil. The material properties of this system are listed in table 6.1, with the resistivity χ of each phase decreased by two orders of magnitude. This in turn decreases the Saville numbers $Sa_{i,o} = \tau_{e(i,o)}/\tau_{c(i,o)}$ by two orders of magnitude, while leaving the remaining dimensionless groups in table 6.2 unchanged. The imposed electric field strength is $E_\infty = 2.3\,\mathrm{kV/cm}$, which yields the capillary numbers $Ca_i = 0.3$ and $Ca_o = 0.2$, respectively. The drop deformation (solid) and relaxation (dashed) curves result from our boundary integral computations.

As an alternative view on the asymmetry between the deformation and relaxation, we examine the transient storage of energy within the drop when the field $\boldsymbol{E}_\infty$ is applied, as well as the release of stored energy when the field is removed. Due to the finite resistivity χ of each fluid, a certain amount of charge $\int_{\frac{1}{2}A} q^* dA$ accumulates at each half of the drop surface. Here, the surface integral is carried out over the right half of the drop. The drop is thus able to store charge at its interface, similar to a capacitor. The energy stored in a capacitor is given by $\frac{1}{2} E_\infty \, a \int_{\frac{1}{2}A} q^* dA$, where $E_\infty \, a$ is the applied voltage. Furthermore, deforming the drop also results in storage of capillary energy, given by $\gamma \int_A dA$. Note that the interfacial tension γ is assumed to remain constant throughout the drop deformation and relaxation. After applying the previously–described scaling for the electric field and surface charge, and normalizing energy by $\gamma \, a^2$, the expressions for capacitive and capillary energy yield $\frac{1}{2} \int_{\frac{1}{2}A} q \, dA$ and $\int dA$, respectively. The storage and release of capacitive and capillary energy for the conditions in figure 6.5 is shown in figure 6.9. Interestingly, figure 6.9(a) indicates that the surface of the drop charges and discharges in a symmetric fashion, on the order of the larger charging timescale $\tau_{e,o} = 12.3\,\mathrm{s}$. However, figure 6.9($b$) displays an asymmetry between the storage and release of capillary energy. This asymmetry is directly correlated to the asymmetry in the drop deformation–relaxation profiles depicted in figure 6.3 and figure 6.5. That is, a drop with an asymmetric deformation–relaxation profile is expected to store and release capillary energy in an asymmetric fashion. Surprisingly, however, the storage and release of capacitive energy is symmetric.

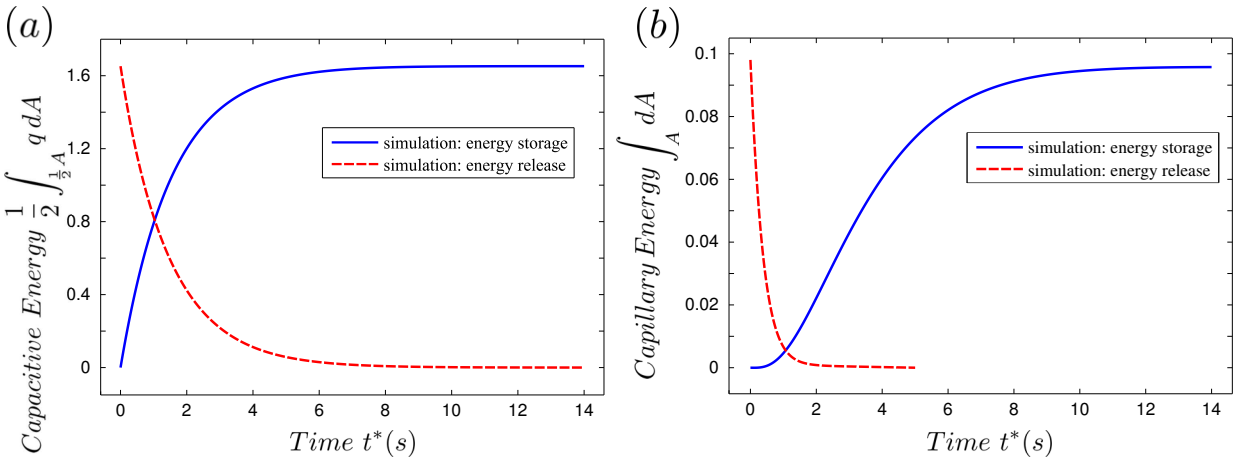

Figure 6.9: Time–dependent energy storage and release by a castor oil drop suspended in silicone oil. The imposed electric field strength is $E_\infty = 2.3\,\mathrm{kV/cm}$, which yields the capillary numbers $Ca_i = 0.3$ and $Ca_o = 0.2$, respectively. This storage and release of energy corresponds to the deformation–relaxation profile illustrated in figure 6.5. Figure 6.9(a) depicts the storage and release of capacitive energy, given in dimensionless form as $\frac{1}{2}\int_{\frac{1}{2}A} q\,dA$. Figure 6.9($b$) illustrates the storage and release of capillary energy, given in dimensionless form as $\int_A dA$. Here, we subtract the dimensionless capillary energy of a spherical drop 4π from the energy profile to depict the deviation from this minimum energy configuration.

6.4 Breakup of a drop upon removal of imposed field

We examine the relaxation of a leaky dielectric system characterized by the set of dimensionless parameters $(S, M, R) = (1.37, 1, 0.1)$, which yields prolate conformations under a uniform DC electric field. The steady–state drop deformation for this system was thoroughly quantified as a function of outer electric capillary number Ca_o by Lac and Homsy.[48] In their analysis, a range of capillary numbers $0.345 < Ca_o < 0.365$ yielded access to two steady drop configurations: spheroidal and two–lobed. Above this electric capillary number ($0.365 \leq Ca_o \leq 0.5$), a family of two through five–lobed drop shapes become attainable. These highly nonlinear shapes do not undergo breakup;

rather, the drops achieve steady–state deformations due to multiple internal recirculating flows.[48]

From this system,[48] the capillary numbers $Ca_o = \{0.3, 0.38, 0.4\}$ are chosen for the present study. For $Ca_o = 0.3$, a steady spheroidal drop deformation is achieved, while $Ca_o = 0.38$ and $Ca_o = 0.4$ yield two–lobed and three–lobed stable shapes, respectively. The transient drop deformation and drop relaxation corresponding to the electric capillary number $Ca_o = 0.3$ is displayed in figure 6.10. Figure 6.11(a) and figure 6.12(a) illustrate the deformation–relaxation profile for $Ca_o = 0.38$ and $Ca_o = 0.4$, respectively. The outer Saville number $Sa_o = \tau_{e,o}/\tau_{c,o}$ for these three computations ($Ca_o = \{0.3, 0.38, 0.4\}$) are chosen as $Sa_o = \{0.167, 0.132, 0.125\}$. Note that the time axis of these figures is normalized by the charging timescale of figure 6.10 for proper comparison of the time–dependent deformation and drop relaxation. These values for the Saville number are chosen due to the fact that they yield $\tau_{e,o} < \tau_{c,o}$, which indicates that the surface of the drop discharges quickly in comparison with the rate at which it relaxes due to capillary stress. Hence, the transient interfacial charging and discharging is assumed to play a minimal role in the drop relaxation process, and we interpret the relaxation of the deformed surface as being capillary–driven.[20,81–83]

After the field is removed, the stable spheroidal configuration attained in figure 6.10 relaxes to a spherical equilibrium shape. The transient deformation profiles for $Ca_o = 0.38$ and $Ca_o = 0.4$ displayed in figure 6.11(a) and figure 6.12(a) display highly nonmonotonic behavior. We believe that this occurs because these values for the capillary number are near $Ca_o = 0.365$, for which bifurcation into two stable drop configurations is observed.[48] The

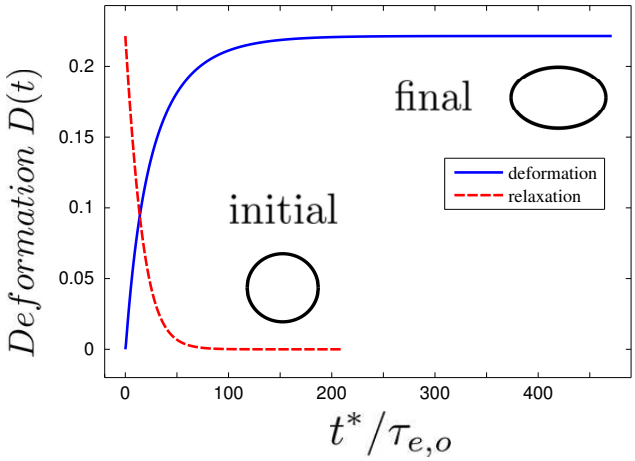

Figure 6.10: Capillary–driven relaxation of a prolate low–conductivity drop corresponding to a system characterized by the dimensionless groups $(S, M, R) = (1.37, 1, 0.1)$.[48] Here, we compute the transient deformation (solid curve) under the imposed uniform field, and allow the drop to undergo relaxation (dashed curve) once the electric field is removed. This figure illustrates the deformation–relaxation profile of a spheroidal configuration achieved at $Ca_o = 0.3$, which is able to recover its initial spherical equilibrium shape upon removal of the applied field.

two and three–lobe shapes illustrated in figure 6.11(b) and figure 6.12(b) undergo breakup once the field is removed. The dashed curve in figure 6.11(b) shows an increase in the time–dependent deformation parameter $D(t)$ when the field is removed after a stable two–lobed shape is achieved at $Ca_o = 0.38$. This increase is due to the occurrence of a local minimum in the drop radius between the two lobes at steady–state, which in this case corresponds to the minor semi–axis. A large capillary pressure results from this minimum, which drives flow towards the two lobes and further elongates the drop shape, eventually leading to breakup[81] (shown at the end of the dashed curve in figure 6.11(b)). The dashed curve in figure 6.12(b) illustrates a continuous decrease in the time–dependent deformation parameter $D(t)$ when the field is removed after a stable three–lobed shape is achieved at $Ca_o = 0.40$. Here, the lobes at the end of the drop drive flow towards the middle lobe, thus causing the drop to retract as the local minimum in drop radius between each lobe pair

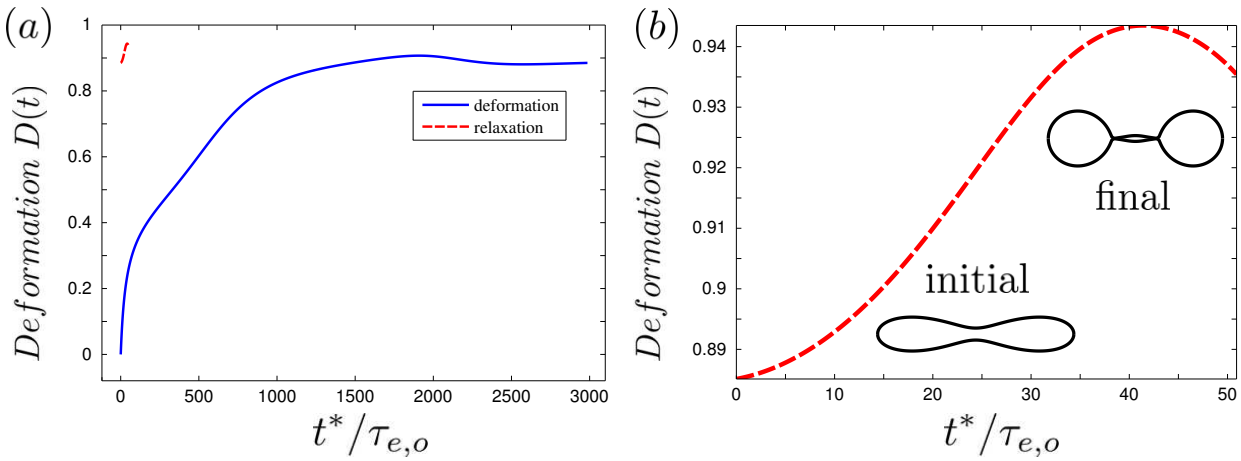

Figure 6.11: Capillary–driven relaxation of a prolate low–conductivity drop corresponding to a system characterized by the dimensionless groups $(S, M, R) = (1.37, 1, 0.1)$.[48] Here, we compute the transient deformation (solid curve) under the imposed uniform field, and allow the drop to undergo relaxation (dashed curve) once the electric field is removed. Figure 6.11(a) illustrates the deformation–relaxation profile of a stable two–lobed shape achieved at $Ca_o = 0.38$, which attains breakup via end–pinching upon removal of the applied field. Figure 6.11(b) depicts the drop breakup process in greater detail. The insets correspond to the initial and final drop shape for the relaxation, respectively.

decreases. Hence, the minor semi–axis increases due to this influx and the deformation decreases before resulting in drop breakup (shown at the end of the dashed curve in figure 6.12(b)).

For the steady two–lobed shape achieved at $Ca_o = 0.38$, we examine two orders of magnitude of the Saville number Sa_o to probe its influence on the relaxation and eventual breakup of this highly nonlinear drop conformation. Figure 6.13 shows that increasing the Saville number from $Sa_o = 0.05$ to $Sa_o = 5$ delays the interfacial discharging process by over two orders of magnitude. Note that the time axis is normalized by the charging timescale for $Sa_o = 0.05$. However, as illustrated in figure 6.14, increasing Sa_o from 0.05 to 5 plays a minimal role on the relaxation process of the drop as well as the

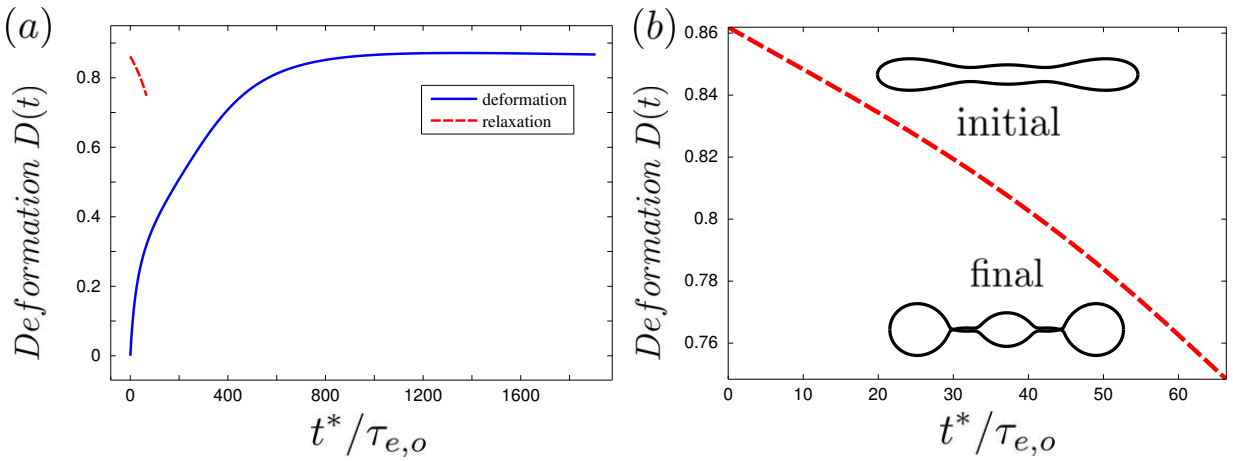

Figure 6.12: Capillary–driven relaxation of a prolate low–conductivity drop corresponding to a system characterized by the dimensionless groups $(S, M, R) = (1.37, 1, 0.1)$.[48] Here, we compute the transient deformation (solid curve) under the imposed uniform field, and allow the drop to undergo relaxation (dashed curve) once the electric field is removed. Figure 6.12(a) illustrates the deformation–relaxation profile of a stable three–lobed shape achieved at $Ca_o = 0.4$, which attains breakup via end–pinching upon removal of the applied field. Figure 6.12(b) depicts the drop breakup process in greater detail. The insets correspond to the initial and final drop shape for the relaxation, respectively.

shape it acquires during breakup. The curve for $Sa_o = 5$ in these two figures indicates that the drop surface has not fully discharged by the time the drop breaks up. Thus, the timescale for breakup does not seem to be enslaved to the charging timescale. We find this to be surprising since varying the Saville numbers $Sa_{i,o}$ plays a crucial role in determining the temporal asymmetry in transient drop deformation and drop relaxation to equilibrium.

In essence, the breakup of the two drops in figure 6.11(b) and figure 6.12(b) results from induced flows at the local minima in radius that separate the drop lobes, which in turn causes the continuous thinning of this radius until pinch–off of the lobes is achieved. This breakup mechanism resulting from capillary–driven drop relaxation, known as "end–pinching,"[20,81–83] was originally devel-

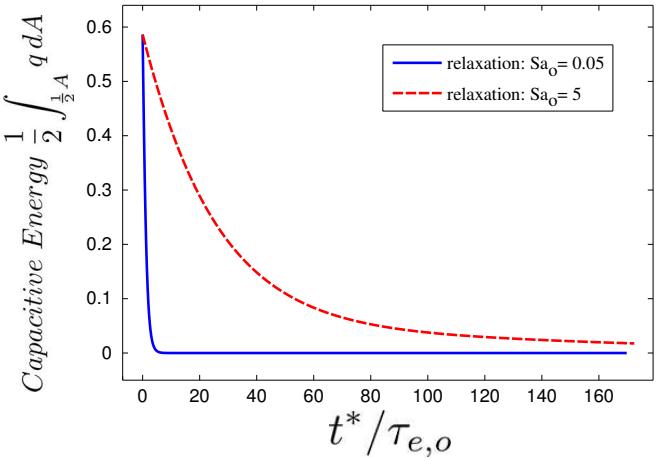

Figure 6.13: Time–dependent release of capacitive energy, given in dimensionless form as $\frac{1}{2}\int_{\frac{1}{2}A} q\,dA$, by a prolate low–conductivity drop corresponding to a system characterized by the dimensionless groups $(S, M, R) = (1.37, 1, 0.1)$.[48] The steady–state two–lobed shape is achieved under a capillary number $Ca_o = 0.38$. This steady drop configuration is allowed to relax under Saville numbers $Sa_o = 0.05$ (solid curve) and $Sa_o = 5$ (dashed curve), respectively. The initial and final shapes for this relaxation process are illustrated in figure 6.11(b).

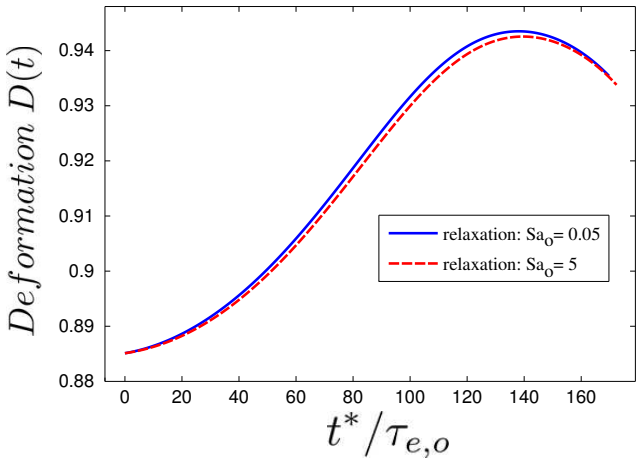

Figure 6.14: Breakup of a prolate low–conductivity drop corresponding to a system characterized by the dimensionless groups $(S, M, R) = (1.37, 1, 0.1)$.[48] The steady–state two–lobed shape is achieved under a capillary number $Ca_o = 0.38$. This steady drop configuration is allowed to relax under Saville numbers $Sa_o = 0.05$ (solid curve) and $Sa_o = 5$ (dashed curve), respectively. The initial and final shapes for this relaxation process are illustrated in figure 6.11(b).

oped to explain the relaxation of drops deformed by uniaxial extensional flows. In those cases, the drops reached steady shapes characterized by long cylindrical midsections with bulbous ends under the imposed flows, and attained breakup once the flow fields were removed. Although we have carried out our computations for drop breakup in the Stokes flow regime $Re_{\mathrm{Flow}(i,o)} \to 0$, inertia has been determined to be relevant during pinch–off of viscous threads resulting from drops undergoing capillary relaxation.[84,85] Here, the local velocity scale at the thinning thread $U_l \sim \tau_b^{\beta-1}$, where τ_b is the time remaining until breakup and the constant parameter $\beta \leq 0.175$. As $\tau_b \to 0$, the local velocity U_l diverges. Hence, the neglect of inertia becomes invalid as the local minimum in drop radius approaches zero. A detailed study that accounts for electrical, viscous, inertial, and capillary forces during drop breakup, however, is outside of the scope of the present article.

6.5 Conclusions

We have examined the deformation–relaxation profile of a prolate low–conductivity drop with permittivity ε_i, resistivity χ_i, and viscosity μ_i suspended in a medium with permittivity ε_o, resistivity χ_o, and viscosity μ_o, respectively. The transient deformation and drop relaxation were computed via the boundary integral method, with transient charging and discharging of the interface accounted for. Our computations for the drop deformation–relaxation profile were first validated through comparison against linear, $O(Ca_{i,o})$ theory. Furthermore, our computational results were also compared against an experimental system consisting of a castor oil drop suspended in a silicone oil medium under two distinct electric field strengths. Our numerical predictions for the transient deformation and drop relaxation qualitatively captured the experimental measurements within the error in measurement of the time–

dependent deformation parameter $D(t)$.

Both our experiments and numerical computations displayed an asymmetry between the drop deformation and relaxation processes, in which the drop relaxed back to its initial spherical shape quickly in comparison to the rate at which it achieved its steady–state deformation. This asymmetry occurred due to the instantaneous reversal of the interfacial tangential electrical stress when the applied field was removed. This in turn reversed the direction of the induced interfacial tangential flow, which was originally directed from the equator towards the poles of the drop and acted to drive the drop away from equilibrium. The tangential electrical stress and capillary stress thus acted in unison to quickly restore the shape of the deformed drop back to equilibrium when the field was removed. For an asymmetry in the drop deformation–relaxation profile to arise, the charging timescales $\tau_{e(i,o)}$ need to be comparable to the capillary timescales $\tau_{c(i,o)}$ so that these electrical stresses remain long–lived to assist the drop retraction process: slow interfacial charging and discharging yields fast drop relaxation. This asymmetry is further accentuated with increasing capillary numbers $Ca_{i,o}$. Our quantification of the transient storage and release of capacitive and capillary energy showed that although the drop stored and released capillary energy in an asymmetric fashion, the storage and release of capacitive energy occurred symmetrically.

Finally, we showed that a drop that achieves a stable field–induced deformation need not relax back to its initial spherical equilibrium shape when the electric field is removed. For the case of two and three–lobed steady shapes,[48] the drop achieved breakup via the end–pinching mechanism.[20,81–83] We believe that end–pinching of the multi–lobed stable drop shapes predicted by our com-

putations would be difficult to achieve experimentally, since large drop aspect ratios yield a high sensitivity to nonuniformities in the applied field. Based on experimental observations, highly deformed drops often migrate under electric fields that are presumed to be uniform, and achieve asymmetric breakup. Instead of achieving a multi–lobed steady drop conformation, we believe that a convenient alternative to observe end–pinching would involve driving drops out of equilibrium at or above their critical capillary number. After the drop has achieved a time–dependent highly nonlinear shape, one would remove the applied field. Such has been the approach taken by researchers who have examined the relaxation of exceedingly deformed drops upon removal of planar extensional flows.[81,86]

We believe that quantifying the deformation–relaxation profiles of weakly conducting drops is useful to understand increasingly complex systems such as multiple drops exposed to electric fields. For example, if two leaky dielectric drops are placed next to each other along the axis of the imposed field[9,59,87] each drop will experience a dielectrophoretic attraction due to the presence of the neighboring drop. Furthermore, the field–induced flows outside each drop may yield drop–drop attraction or repulsion.[59] For drops separated at large distances relative to their radius, this EHD response will dictate the interaction between the two drops. If the field is removed, our results indicate that provided that the drops do not coalesce, the finite charging timescales $\tau_{e(i,o)}$ would yield EHD flows outside each drop that would in turn provide a strong yet short–lived opposing interaction in comparison to that achieved under the applied field. That is, if the field–induced flows yielded a net attractive (repulsive) force, the drops would experience a greater repulsive (attractive) force upon removal of the field. We also expect the nonzero charging timescales $\tau_{e(i,o)}$

of these low–conductivity fluids to affect the rheological response of multiple–drop systems under the simultaneous application of electric fields and flow fields[38,73,75] during deformation and relaxation, respectively.

Finally, surface charge convection was neglected throughout the majority of this work due to its minimal role in determining the transient deformation and drop relaxation measured in our experiments. However, we hypothesize that its effect on drop deformation and relaxation of field–induced multi–lobed configurations will be significantly more pronounced. Examining the effect of charge convection on the evolution of highly nonlinear prolate drop shapes is currently under investigation.

7. The breakup of an oil drop containing a colloidal suspension of carbon black particles under a uniform DC electric field

7.1 Introduction

Suspension stability in nonpolar fluids is of relevance for use in the petroleum industry,[88] use in drug delivery,[89] and use in electrophoretic displays.[90] Stability of the suspension may be achieved via the addition of surfactant, which prevents particle aggregation through either steric stabilization due to polymer adsorbed to the particle surface, or electrostatic stabilization due to particle surface charging.[91] These two regimes of suspension stability may be attained through varying amounts of added dispersant. The Bjerrum length $\lambda_B = \frac{e^2}{4\pi\varepsilon_r\varepsilon_0 k_B T}$ characterizes the distance required for the electric potential energy between two opposite monovalent charges to balance the thermal energy, thus resulting in the separation of the two charges. Here, e is the elementary charge, ε_r represents the relative electric permittivity, ε_0 denotes the permittivity of free space, k_B represents the Boltzmann constant, and T is the absolute

temperature. Due to the low dielectric constant of nonpolar fluids ($\varepsilon_r \approx 2$) in comparison to water ($\varepsilon_r \approx 80$), the Bjerrum length λ_B for these systems is around 40 times greater than it is for water. The addition of surfactant to nonpolar fluids helps lower the Bjerrum length through the formation of reverse micelles, which contain polar head groups that locally increase the permittivity of the solution;[92] this results in electrostatic stabilization of the colloidal suspension. Although dispersants are often implemented to yield stabilization of charge in nonpolar fluids, the origin and dynamics of charge in these low–conductivity systems remains an active research area in colloid science.[93–96]

One may find a number of studies regarding the formation of colloidal aggregates under the action of an electric field[97–99] or flow field,[100–102] and the breakup of aggregates under flow fields.[103–105] However, comparatively less research has been conducted with respect to drops containing suspensions of varying degrees of colloidal stability. Furthermore, the influence of external stimuli, such as an electric field, on drops with a range of suspension stabilities has not been addressed. The aim of this work is to examine the breakup of an oil drop composed of a fixed amount of carbon black particles suspended in a nonpolar fluid under a uniform DC electric field. Varying amounts surfactant will be added to the suspension to yield a range of degrees of colloidal stability. As we shall show, two distinct concentrations of dispersant yield radically different field–induced drop breakup. To our knowledge, this a previously–unobserved phenomenon. Processes such as piezoelectric inkjet printing require the application of a voltage to generate liquid drops often composed of dilute colloidal suspensions.[2,106] Moreover, we expect that our results will permit a deduction on colloidal stability based on the qualitative drop breakup configurations achieved under applied electric fields. This could in turn help

tune key parameters in applications, such as particle concentration and applied voltage, to achieve a desired outcome such as a specific electric–field–induced drop breakup conformation.

7.2 Materials and methods

7.2.1 Sample preparation and experimental setup

Samples of carbon black (Monarch 280, Cabot Corporation) and polyisobutylene succinimide surfactant (OLOA 11000, Chevron Oronite) suspended in squalane (Alfa Aesar) were produced in 50 ml vials at various concentrations of OLOA. The carbon black was reported to have a primary particle diameter of 30 nm. A primary particle aggregate diameter of 200 nm was determined from light scattering measurements (Zetasizer Nano ZS90). The true composition of OLOA 11000 is 75% surfactant and 25% mineral oil. However, the amount of mineral oil was considered negligibly small when preparing the samples. Hence, we interpreted the amount of added OLOA as pure surfactant. In this work, the added amount of surfactant is reported in parts OLOA per 100 parts carbon black (pph). Carbon black was heated in a vacuum oven at 200°C for 4 hours and allowed to cool to remove trace amounts of water. Then, the particles were introduced into premixed samples of squalane and OLOA surfactant; the particle concentration was fixed at 3.3 g/L and the carbon black volume fraction was fixed at 0.19%. The samples were sonicated (Cole–Parmer 750–Watt Ultrasonic Homogenizer) for 20 minutes and stored in a desiccator. For each experiment, the samples were resonicated for 30 minutes. The colloidal stability of a given sample was evaluated by conducting millifluidic experiments on an particle–loaded squalane drop, in which the area that contains carbon black was measured throughout time. These experiments were conducted in conjunction with measurements for the

fluid conductivity. A suspension that is sterically stabilized is expected to yield a clear supernatant within the drop, thus indicating that the carbon black particles have aggregated and the colloidal clusters have sedimented. An electrostatically–stabilized suspension is expected to yield no supernatant and display an increase in the measured solution conductivity. Although we do not allude to these measurements that quantify colloidal stability, we utilize them to interpret the dynamics of the particle–loaded squalane drops under the electric fields implemented in our experiments.

The drop of particle–loaded squalane is injected into a plastic cell filled with silicone oil. A voltage on the order of kV/cm is applied across two $5\,\mathrm{cm} \times 5\,\mathrm{cm}$ brass electrodes separated at a distance of 2 cm using high–voltage DC power supply (Gamma High Voltage Research, Inc.). As soon as the electric field is applied, the time–dependent drop shape is recorded at a rate of 7.5 frames per second using a firewire camera (Guppy PRO F–125B, Allied Vision Technologies). Image analysis is conducted using ImageJ software. The material properties of the systems examined in this study are listed in table 7.1. The permittivity and resistivity of each fluid is measured via electrochemical impedance spectroscopy.[63] The viscosity of each phase is extracted from the literature. Finally, the interfacial tension is acquired by fitting our previously–developed linear theory, which quantifies the electric field–induced transient deformation of a low–conductivity drop,[55] to the experimental timespan during which the drop deformation is $O(10^{-2})$. Here, the deformation is quantified as the difference between the drop semi–axes parallel and normal to the applied field divided by the sum of the two.

7.2.2 Computation of transient drop shape

We implement the boundary integral method to compute the electric field and fluid flow at the drop surface, as well as the resulting drop deformation. The differential governing equations are those described by Taylor's leaky dielectric model.[13–15] Here, the electric field is governed by Laplace's equation for the electrostatic potential and the fluid flow is governed by the Stokes equations for the velocity and pressure fields. The linearity of the differential equations conveniently permits a reformulation to integral equations that hold at the drop surface. The form and numerical solution procedure of the integral equations is discussed in detail in previous publications.[9,45,48,59,60,80] These equations apply to viscous low–conductivity systems, for which the volumetric charge density is negligibly small; charge is localized at the drop interface. This entails the exertion of interfacial tangential electrical stresses by the applied electric field, which are balanced by viscous stresses; a steady recirculating flow is generated within the drop and throughout the medium. The resulting drop deformation may be along (prolate) the applied field or normal (oblate) to the applied field, depending on the ratio of the permittivity $S = \varepsilon_i/\varepsilon_o$, resistivity $R = \chi_i/\chi_o$, and viscosity $M = \mu_i/\mu_o$ of the fluids. Here, the subscripts denote the drop (inner, i) and medium (outer, o) phases, respectively. If charging of the drop surface is assumed instantaneous, the magnitude of the resulting drop shape for a system with fixed values for the parameters $\{S, M, R\}$ is dictated by the electric capillary number $Ca_o = \varepsilon_o E_\infty^2 a/\gamma$. This dimensionless group quantifies the strength of the electrical stress $\varepsilon_o E_\infty^2$ that acts to deform the drop, relative to the capillary stress γ/a that acts to restore the drop back to equilibrium. Here, E_∞ is the magnitude of the uniform applied field, a denotes the radius of a spherical drop, and γ represents the interfacial tension. Although we refer to the capillary number Ca_o as that of the medium, we

examine this and the remainder of the dimensionless groups for both phases throughout this work.

In practice, charging of the drop surface does not occur instantaneously. This leads to the examination of charge transport towards[21,54,55,80] and along[21,47,49,80] the interface. The characteristic timescale for the drop to acquire a certain amount of charge per unit area q^* at steady–state is the electrical relaxation timescale $\tau_{e,o} = \varepsilon_o \chi_o$. Note that the superscript $*$ is implemented to denote a dimensional variable; the lack of a superscript renders that variable dimensionless. This charging timescale leads to the examination of the governing equation dictating the conservation of interfacial charge, which reads in dimensionless form as

$$\frac{1}{R} E_{n,i} - E_{n,o} = Sa_o \frac{\partial q}{\partial t} + Re_o \nabla_s \cdot (\boldsymbol{u}_o q). \tag{7.1}$$

Here, $E_{n,i}$ and $E_{n,o}$ denote the inner and outer normal electric fields evaluated at the interface. Furthermore, note that the electric fields have been normalized by the magnitude of the uniform applied field E_∞, the surface charge density has been normalized by $\varepsilon_o E_\infty$, time has been normalized by the capillary timescale $\tau_{c,o} = \mu_o a/\gamma$ that characterizes deformation of the interface, distance has been normalized by the drop radius a, and velocity has been normalized by the characteristic velocity scale U. This equation is applied as a boundary condition to solve for the electric field at the surface of the drop. Importantly, terms in the right–hand side of this equation represent transient charging of the interface and convection of the charge by the induced fluid flow. The dimensionless groups that dictate the relative importance of these charge transport mechanisms are the Saville number[15] $Sa_o = \tau_{e,o}/\tau_{c,o}$, which repre-

sents a ratio of the charging timescale $\tau_{e,o} = \varepsilon_o \chi_o$ to the capillary timescale $\tau_{c,o} = \mu_o a/\gamma$, and the electric Reynolds number[14] $Re_o = \tau_{e,o}/\tau_f$, which represents a ratio of the charging timescale to the flow timescale $\tau_f = a/U$. For the low–conductivity systems and high applied field strengths examined here, these two dimensionless groups and corresponding charge transport mechanisms are of relevance to capture the correct time–dependent field–induced drop configurations. We also discuss the consequences of these two forms of charge transport in our previous publication.[80] In the present work, our computations are implemented to predict the qualitative transient drop shape achieved under the experimental conditions. Note the computations assume a homogeneous drop phase; the numerical predictions for the drop shape will be implemented to evaluate the heterogeneity of the particle–loaded drop.

7.3 Breakup of a squalane drop

We first examine the field–induced breakup of a pure squalane drop suspended in silicone oil via experiment and computation. The material properties for this system and the remainder of the systems examined in this study are listed in table 7.1; the relevant dimensionless groups are listed in table 7.2. Here, the drop is more conductive ($R < 1$) and less viscous ($M < 1$) than the medium. The resulting transient drop deformation for this system (and all systems that follow) is along the electric field; i.e. the drop undergoes a prolate deformation. The applied field is 7.6 kV/cm, which is approximately the critical field strength to induce breakup of the pure squalane drop in our experiment.

Phase	ε_r	$1/\chi$ (S/m)	μ (Pa s)	a (mm)	γ (mN/m)
medium–silicone oil	2.8	2.0×10^{-12}	4.80	–	–
drop–squalane (pure)	2.1	2.1×10^{-12}	0.03	0.6	4.6
drop–squalane (30 pph–no CB)	2.1	2.2×10^{-10}	0.03	0.7	5.2
drop–squalane (30 pph–with CB)	2.1	2.6×10^{-10}	0.03	0.6	1.4
drop–squalane (2 pph–with CB)	2.1	2.3×10^{-10}	0.03	0.6	1.5

Table 7.1: Material properties of a squalane drop suspended in silicone oil. Here, ε_r denotes the relative permittivity and "CB" denotes carbon black.

Phase	Ca	Sa	Re	S	M	R
medium–silicone oil	1.7	21.1	36.6	–	–	–
drop–squalane (pure)	1.3	2.6×10^3	3.4×10^3	0.75	0.01	0.97
drop–squalane (30 pph–no CB)	0.2	22.4	3.6	0.75	0.01	0.01
drop–squalane (30 pph–with CB)	0.6	6.5	4.1	0.75	0.01	0.01
drop–squalane (2 pph–with CB)	0.5	7.2	3.5	0.75	0.01	0.01

Table 7.2: Dimensionless groups that describe a squalane drop suspended in silicone oil. Here, "CB" denotes carbon black.

The time–dependent drop shape for this system is displayed in figure 7.1(a). In this figure (and all figures that follow), the applied electric field is directed from left to right. The change in the shape of the drop is quantified through changes in the dimensionless drop major semi–axis L/a. Here, L represents half of the length of the drop parallel to the applied field; it is initially equal to the spherical drop radius a. The open circles denote the experimental measurement, while the solid curve results from boundary integral computations conducted at the conditions of the experiment. The experiment shows that the squalane drop forms pointed ends and achieves breakup via tipstreaming at the end nearest to the left electrode; the measurement is illustrated until this point in time ($t^* = 14.1$ s). The inset next to the experimental curve in figure 7.1(a) displays the asymmetric drop breakup at this point in time; the inset below shows the eventual breakup through tipstreaming from both

pointed ends of the drop.

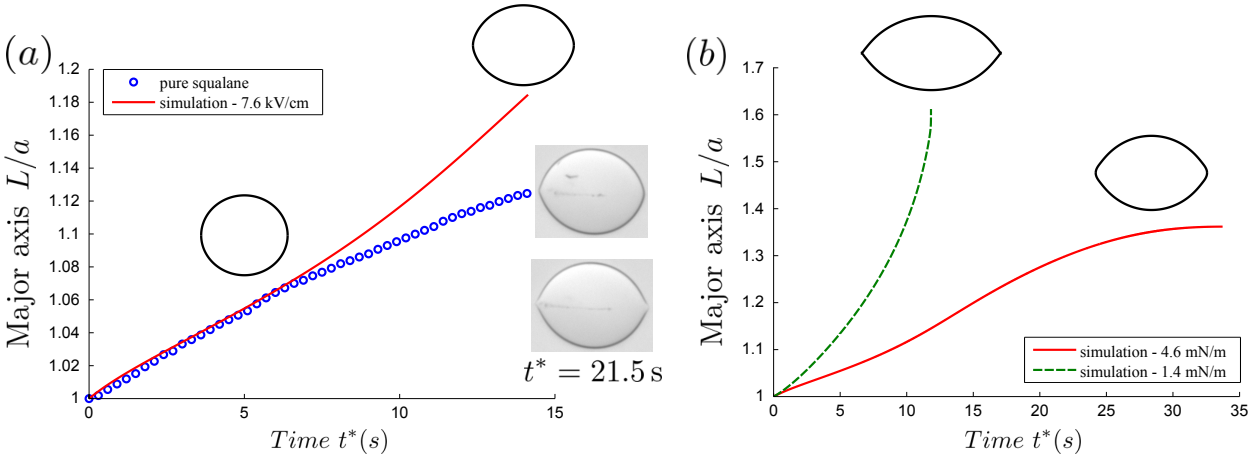

Figure 7.1: (a) Experiment and computation illustrating the time–dependent dimensionless major semi–axis of a pure squalane drop suspended in silicone oil at an electric field strength $E_\infty = 7.6\,\mathrm{kV/cm}$. The material properties for this system are listed in table 7.1, while the relevant dimensionless groups are listed in table 7.2. (b) Computations for the time–dependent dimensionless major semi–axis of a pure squalane drop suspended in silicone oil at an electric field strength $E_\infty = 7.6\,\mathrm{kV/cm}$ and two different values for the interfacial tension γ.

The computational curve is illustrated until $t^* = 14.1\,\mathrm{s}$ for proper comparison against the experimental measurement; the insets above this curve display the time–dependent drop shape at $t^* = 5\,\mathrm{s}$ and the end of the experimental curve, respectively. The solid curve in figure 7.1(b) is a continuation of the solid curve in figure 7.1(a). Although the experiment indicates that the squalane drop undergoes breakup at this electric field strength, the solid curve in figure 7.1(b) suggests that the drop achieves a steady prolate configuration that exceeds the maximum aspect ratio measured in the experiment. This steady–state shape is non–spheroidal; the drop forms pointed ends without undergoing actual breakup. We believe that this stable non–spheroidal conformation is difficult to achieve experimentally due to its high sensitivity

to non–uniformities in the applied electric field. Thus, the discrepancy between the experiment and computation arises as the squalane drop undergoes breakup in the experiment while the computation predicts a steady drop shape.

The dashed curve in figure 7.1(b) shows the effect of a varying interfacial tension on the shape development of the pure squalane drop at the same applied field strength. Here, we have chosen the lowest interfacial tension from the experimental systems that will be analyzed in this study, all of which are listed in table 7.1. This system corresponds to a millimeter–sized drop of squalane with a concentration of 3.3 g/L carbon black and 30 pph OLOA surfactant suspended in silicone oil. As illustrated by the dashed curve in figure 7.1(b), lowering the interfacial tension from that of pure squalane in silicone oil yields drop breakup in our computation. Although lowering the interfacial tension has increased the electric capillary number from $Ca_o = 1.7$ to $Ca_o = 5.6$ to yield drop breakup at a fixed field strength, the general qualitative time–dependent shape of the drop remains relatively unchanged; i.e. the drop still forms pointed ends. Furthermore, this drop shape does not resemble the transient shapes and breakup modes of the particle–loaded drops presented in the proceeding sections. Since the systems to be analyzed are characterized by different drop conductivities and interfacial tensions, we postulate that the differing transient deformation and breakup processes between a pure squalane drop and a squalane drop with carbon black particles and OLOA surfactant occur mainly due to a change in drop conductivity, not interfacial tension. We elaborate on these differing time–dependent processes in the next section.

7.4 Breakup of a drop containing a stable colloidal suspension

The breakup of a drop containing a stable suspension of carbon black particles is quantified experimentally. Here, the amount of added surfactant (30 pph OLOA) is enough to provide stabilization of the suspension through electrostatic repulsion between the particles. As a basis for comparison, we examine the breakup of a drop containing an equivalent amount of surfactant with no carbon black. The time–dependent major semi–axis of the drops containing a fixed amount of surfactant with and without carbon black is depicted by the open circles and open squares in figure 7.2(a). Here, the applied field is $E_\infty = 2.5\,\mathrm{kV/cm}$, which is much lower than the electric field required to achieve the breakup of a pure squalane drop $E_\infty = 7.6\,\mathrm{kV/cm}$.

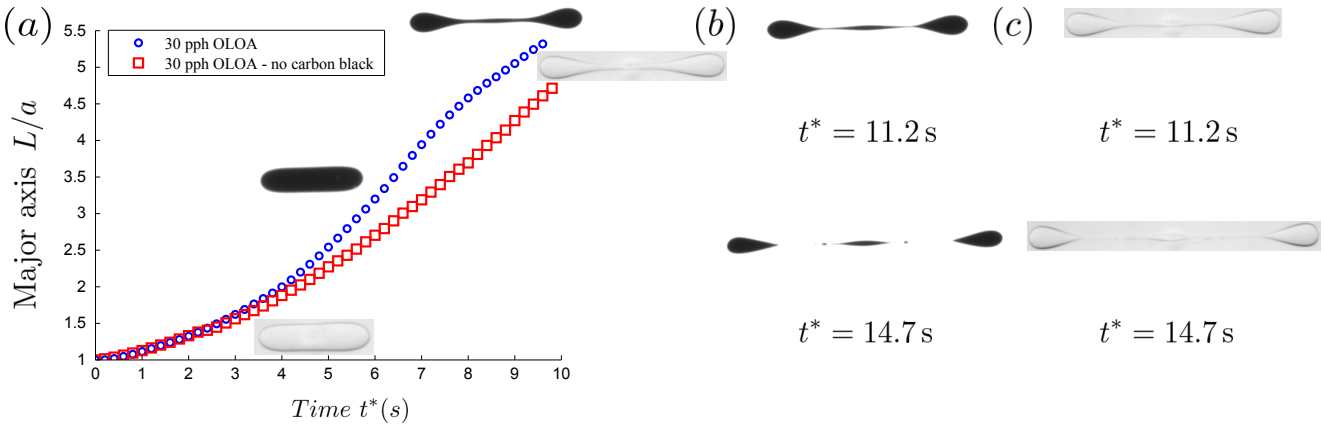

Figure 7.2: (a) Experiments illustrating the time–dependent dimensionless major semi–axis of a squalane drop containing 3.3 g/L carbon black and 30 pph OLOA surfactant, and a drop containing the equivalent amount of surfactant and no carbon black. Here, the drops are suspended in silicone oil and the applied field strength $E_\infty = 2.5\,\mathrm{kV/cm}$. The material properties for this system are listed in table 7.1, while the relevant dimensionless groups are listed in table 7.2. (b), (c) Electric field–induced drop breakup of the systems described in figure 7.2(a).

Figure 7.2 shows that at early times $t^* \leq 4\,\mathrm{s}$, the two experimental curves overlap. As time progresses, the two curves deviate from one another until the onset of drop breakup is achieved; the two experiments are illustrated until this point in time ($t^* = 9.7\,\mathrm{s}$). The insets for each curve display the shapes of the drop at $t^* = 5\,\mathrm{s}$ and the end of the measurement, respectively. Figures 7.2(b) and 7.2(c) illustrate the breakup process of the drop containing carbon black particles stabilized by surfactant and the drop containing surfactant only. As shown in table 7.1, the two material properties that change from those pertaining to figure 7.1 are the drop conductivity and interfacial tension. As stated in the previous section, changing the interfacial tension from that of pure squalane against silicone oil (4.6 mN/m) to that of squalane containing a colloidal suspension stabilized by 30 pph OLOA against silicone oil (1.4 mN/m) does not appreciably vary the time–dependent shape and breakup mode of a pure squalane drop. Thus, we attribute the change in breakup mode from figure 7.1 to figure 7.2 due to a change of two orders of magnitude in the conductivity of the drop (note that the viscosity ratio M remains unchanged). Due to the fact that the drop conductivity has increased by two orders of magnitude relative to figure 7.1 (see table 7.1), the mismatch in conductivity between the two phases is accentuated for the system illustrated in figure 7.2 (see table 7.2). This in turn provides a substantial decrease in the field strength required to promote drop breakup. Furthermore, instead of achieving drop breakup via tipstreaming from pointed ends, the drop now breaks up through the formation of two bulbous ends connected by a thin midsection.

The two curves that quantify the normalized drop major semi–axis in figure 7.2(a) and the images shown in figure 7.2(b) and 7.2(c) suggest that the

development of the drop shape, the onset of drop breakup, and the actual breakup process of a drop with surfactant and carbon black is qualitatively similar to that of a drop with surfactant alone. This is due to the fact that the carbon black particles are stabilized by 30 pph OLOA, which in turn yields homogeneous drop breakup that resembles the breakup of a drop with no carbon black and the equivalent amount of surfactant, which simply provides an increase in the conductivity of the inner phase. Although these two systems display similar qualitative behavior, we highlight the slight deviation between the two curves in figure 7.2(a). At times $t^* > 5\,\mathrm{s}$, the measurement for the system with carbon black and 30 pph OLOA displays a change in both slope and concavity, finally ending with a breakup conformation that slightly exceeds the measurement for the drop with surfactant only. Since the conductivity does not vary appreciably from one drop system to another, we attribute the slightly larger aspect ratio of the drop with carbon black and surfactant as the drop approaches the onset of breakup due to a decrease in interfacial tension between the fluids. We suggest that this may occur due to an adsorption of carbon black particles to the oil–oil interface as flows within the drop develop and the surface continually deforms.

We aim to model the drop breakup and uncover the occurring charge transport dynamics of the carbon black system stabilized by 30 pph OLOA through our boundary integral computations. The results of our computations for the time–dependent drop shape are plotted against the experimental measurement in figure 7.3. Here, the solid line results from a computation that accounts for both interfacial charge relaxation and charge convection, while the dashed curve results from a computation that only accounts for charge relaxation, respectively. The inset at $t^* = 5\,\mathrm{s}$ displays a spheroidal drop shape that all

of the illustrated curves share in common. The solid curve follows the experimental measurement in comparison to the dashed curve, which suggests that interfacial charge convection by the field–induced fluid flow is relevant. This is expected due to the large electrical Reynolds numbers of the drop $Re_i = 4.1$ and medium $Re_o = 36.6$, respectively. Hence, we expect the solid curve to closely follow the experimental measurement. However, as we have shown in our previous work, systems with high electrical Reynolds numbers display shocks in the surface charge distribution of a drop due to the interfacial charge convection mechanism.[80] For the system we studied in that work, the charge shock occurred near the equator due to charge convection from the poles towards the equator of the oblate drop. In the current work, a rapid variation in the surface charge density is observed near the poles due to the convection of charge from the equator towards the poles of the drop. This shock in the interfacial charge density distribution renders our computations difficult to yield a steady–state deformation. Although the computation that accounts for surface charge convection is only able to reach $t^* = 4.5\,\mathrm{s}$, the computation that does not account for charge convection (while only accounting for charge relaxation) predicts a shape during the onset of drop breakup that qualitatively follows that measured in the experiment, as observed in the insets at the end of the computational and experimental curves, respectively. This suggests that the dynamics of the particle–loaded drop are akin to a homogeneous drop, which we believe is due to the stability of the carbon black suspension inside of the drop within the timescale of the experiment.

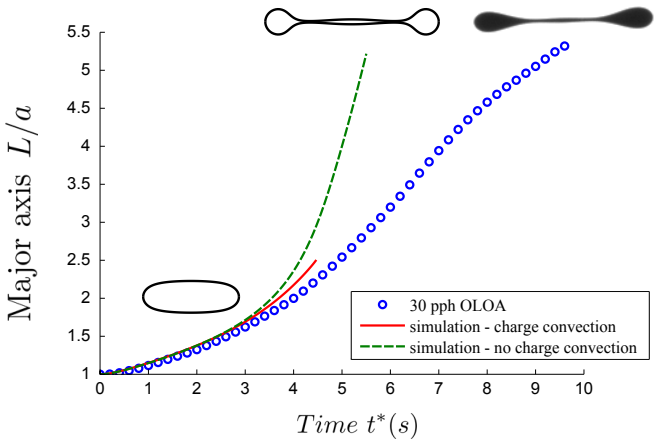

Figure 7.3: (a) Experiment and computations illustrating the time–dependent dimensionless major semi–axis of a squalane drop containing 3.3 g/L carbon black and 30 pph OLOA surfactant. Here, the drop is suspended in silicone oil and the applied field strength $E_\infty = 2.5\,\mathrm{kV/cm}$. The material properties for this system are listed in table 7.1, while the relevant dimensionless groups are listed in table 7.2.

7.5 Breakup of a drop containing an unstable colloidal suspensions

The field–induced breakup of a drop containing 3.3 g/L carbon black with 2 pph added OLOA surfactant is examined at the same field strength applied in the previous section. Note that although table 7.1 suggests that the electrical conductivity of the fluid is similar to that of squalane with carbon black stabilized by 30 pph OLOA, we believe that this is an artifact of electrical percolation across the cell implemented to conduct the electrochemical impedance spectroscopy measurements; the particle–free conductivity of the system is expected to exhibit a much lower value, as the concentration of added dispersant is presumed to yield no electrostatic stabilization. The time–dependent drop shape for this system is depicted by the open squares in figure 7.4. The experimental measurement for the 30 pph system is presented as a basis for comparison. The insets for the 2 pph system show the drop shapes for each

experiment at times $t^* = 5\,\mathrm{s}$ and $t^* = 7.9\,\mathrm{s}$, respectively.

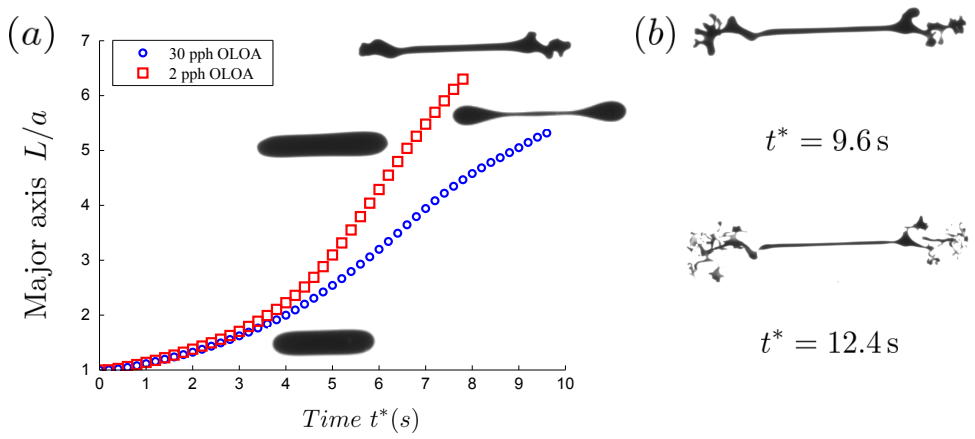

Figure 7.4: (a) Experiments illustrating the time–dependent dimensionless major semi–axis of a squalane drop containing 3.3 g/L carbon black and 30 pph OLOA surfactant, and a drop containing the equivalent amount of carbon black and 2 pph OLOA. Here, the drops are suspended in silicone oil and the applied field strength $E_\infty = 2.5\,\mathrm{kV/cm}$. The material properties for this system are listed in table 7.1, while the relevant dimensionless groups are listed in table 7.2. (b) Electric field–induced drop breakup of the systems described in figure $4(a)$.

At early times $t^* \leq 4\,\mathrm{s}$, the measurements for 2 pph OLOA and 30 pph OLOA overlap. Here, the lower concentration of added surfactant provides short–term steric stabilization of the colloidal suspension. As soon as the 2 pph sample undergoes the sonication process, the carbon black particles begin to flocculate. The aggregation time is within the timescale of the experimental measurement (minutes); hence, the drop shape corresponding to the 2 pph sample eventually deviates from the curve describing the 30 pph system and achieves a radically different breakup mode. Here, the extremities of the drop, which are attached by a thin midsection, yield asymmetric lobes that form fingers that extend into each electrode and eventually disintegrate. We believe that this unstable drop breakup mechanism occurs due to the formation of carbon black aggregates during the timescale of the experiment. Inhomogeneities

within the drop arise due to the sedimentation of these colloidal clusters towards the bottom of the drop (into the page for the images presented in figure 7.4). The drop in turn displays an inhomogeneous breakup conformation due to the action of the applied field on the formed clusters.

When the 2 pph system is placed in the cell for a prolonged amount of time before an electric field of the same magnitude is applied, the transient drop configuration is given by the open squares in figure 7.5. A time of 11 minutes is chosen before applying the field because that is the time elapsed for the squalane drop to rise from the bottom of the cell towards the middle of the two $5\,\mathrm{cm} \times 5\,\mathrm{cm}$ electrodes, where the field is presumed to be uniform. Keeping the drop suspended for this amount of time allows for the carbon black particles to further flocculate and form aggregates that will sediment towards the bottom of the drop by the time the field is applied. The experimental measurement for the 2 pph system that is subjected to an electric field immediately after the drop is generated is depicted by the open circles as a basis for comparison. Here, the drop shows signs of heterogeneity at time $t^* = 0\,\mathrm{s}$ and attains a non–spheroidal shape at an early stage of the deformation process, as evidenced by the inset for this measurement at $t^* = 3\,\mathrm{s}$. The drop proceeds to extend and achieve breakup through the formation of a continually–thinning midsection with lobes at each end that eventually form fingers that extend towards the electrodes and disintegrate (see figure 7.5(b)). This unstable drop breakup mode, which was also observed for the system corresponding to the measurement depicted by the open circles, now occurs when the drop is relatively less extended. We believe that this is due to the extended period of time during which the drop was suspended and the colloidal suspension was allowed to destabilize under the lack of the applied electric field.

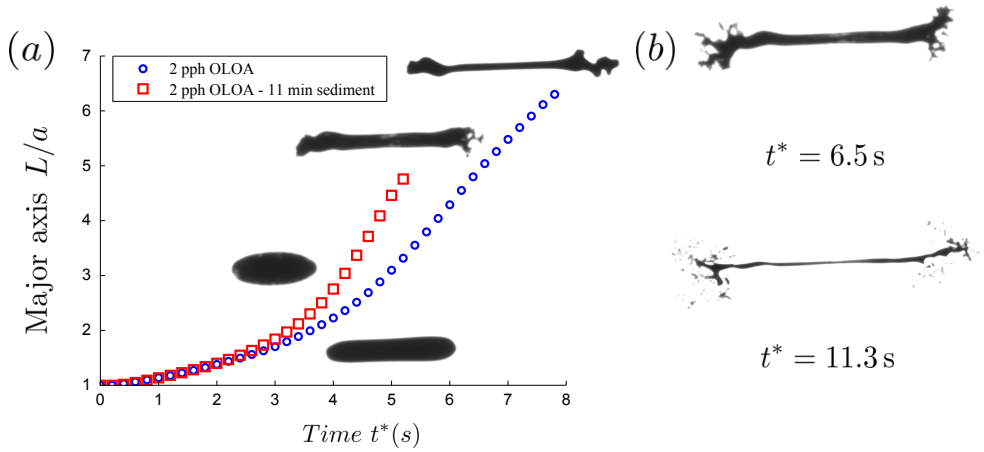

Figure 7.5: (a) Experiments illustrating the time–dependent dimensionless major semi–axis of a squalane drop containing 3.3 g/L carbon black and 2 pph OLOA surfactant. Here, the drops are suspended in silicone oil, and the field strength $E_\infty = 2.5\,\mathrm{kV/cm}$ is applied immediately (open circles) and 11 minutes (open squares) after the drop is generated. The material properties for this system are listed in table 7.1, while the relevant dimensionless groups are listed in table 7.2. (b) Electric field–induced drop breakup of the system described in figure 7.5(a).

7.6 Field–induced destabilization of a drop containing a stable colloidal suspension

The 30 pph system is reexamined at a higher applied field strength of 5.3 kV/cm. The resulting measurement for the development of the dimensionless drop major semi–axis is denoted by the open squares in figure 7.6(a). Here, the drop quickly achieves a highly elongated conformation before reaching the onset of breakup, in comparison to the 30 pph system at a lower field strength $E_\infty = 2.5\,\mathrm{kV/cm}$. A higher electric field entails a higher electric capillary number $Ca = \varepsilon_o E_\infty^2 a/\gamma$, which represents the ratio of electrical stress, given by the scaling $\varepsilon_o E_\infty^2$, to capillary stress, given by the scaling γ/a. The larger drop conformation is due to an increased electrical stress that acts against the capillary stress to further drive the drop away from equilibrium under the higher

applied field. Furthermore, the electric capillary number may be interpreted as a ratio of timescales $Ca = \tau_c/\tau_f$, where $\tau_c = \mu a/\gamma$ denotes the capillary timescale for interface deformation and $\tau_f = a/U$ represents the timescale for the development of fluid flow. Here, the characteristic flow timescale $U \sim E_\infty^2$, which becomes evident when balancing the scaling for electrical stress $\varepsilon_o E_\infty^2$ against the scaling for viscous stress $\mu_o U/a$. In this case, a higher capillary number indicates that a quick flow timescale τ_f yields a fast development of the electric field–induced flow that acts to deform the drop.

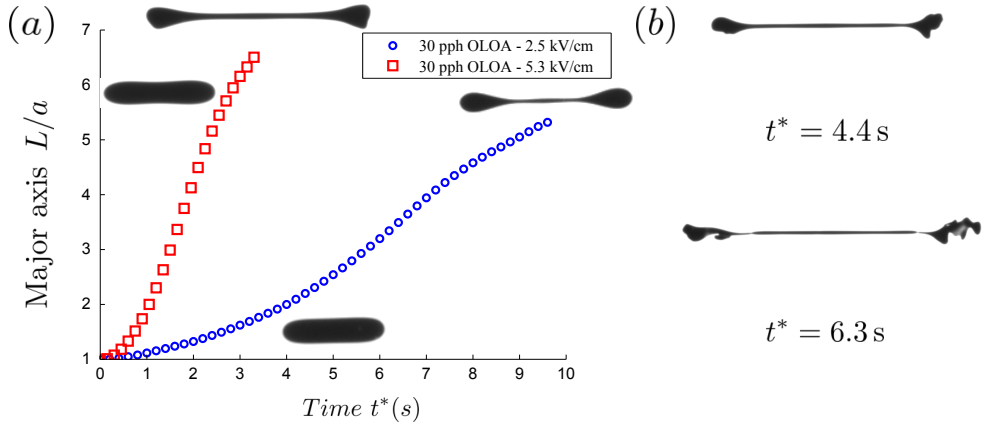

Figure 7.6: (a) Experiments illustrating the time–dependent dimensionless major semi–axis of a squalane drop containing 3.3 g/L carbon black and 30 pph OLOA surfactant. Here, the drops are suspended in silicone oil, and the applied field strengths are $E_\infty = 2.5\,\mathrm{kV/cm}$ and $E_\infty = 5.3\,\mathrm{kV/cm}$, respectively. The material properties for this system are listed in table 7.1, while the relevant dimensionless groups are listed in table 7.2. (b) Electric field–induced drop breakup of the system described in figure 7.6(a).

The breakup process of the drop is shown in figure 7.6(b). Importantly, the lobes depicted in this figure motivate us to recall the breakup of the 2 pph system illustrated in figure 7.4 and figure 7.5. We believe that this high electric field strength has caused aggregation of the stable suspension of carbon black particles. This field–induced destabilization could occur due to the action of

the electric field on the double layer that surrounds each colloid, which served to electrostatically stabilize the suspension. Furthermore, the carbon black particles may be experiencing a dielectrophoretic force, as the electric field experienced by each colloid within the drop is non–uniform. The effect of the non–uniformity of the applied field is further accentuated when the droplet is highly elongated and the two lobes approach the neighboring electrodes.

7.7 Conclusions

We have quantified the breakup of a low–conductivity squalane drop containing carbon black particles and varying amounts of OLOA surfactant. When the amount of surfactant was appreciable (30 parts OLOA per 100 parts carbon black, pph OLOA) for a fixed concentration of 3.3 g/L carbon black, the drop achieved homogeneous breakup under an applied field of $E_\infty = 2.5\,\mathrm{kV/cm}$ via the formation of bulbous ends. The homogeneous breakup of the system with carbon black and and 30 pph OLOA occurred due to the long term electrostatic stabilization[91] of the colloidal particles by the dispersant. Lower concentrations of surfactant (2 pph OLOA) yielded inhomogeneous drop breakup, in which the lobe at each end of the drop formed fingers that extended towards the electrodes and eventually disintegrated. In this system, the lower amount of surfactant provided short term steric stability[91] of the carbon black particles; the colloidal suspension began to flocculate as soon as the drop was generated and the aggregates sedimented towards the bottom of the drop within the timescale of the experiment (minutes). Extending the aggregation time of the suspension before the uniform field was applied yielded the same qualitative drop breakup mode at lower aspect ratios. Finally, we achieved destabilization of a stable colloidal suspension of carbon black and 30 pph OLOA by increasing the previously–applied field strength to $E_\infty = 5.3\,\mathrm{kV/cm}$. Here, the

drop rapidly extended towards a highly elongated two–lobed conformation, after which the two lobes disintegrated in a similar fashion to the sterically–stabilized 2 pph system.

8. Conclusions

We have quantified the importance of surface charge transport on the time–dependent response of a low–conductivity drop exposed to a uniform DC electric field. Here, the response encompasses the transient drop deformation under an applied electric field, drop relaxation upon removal of the applied field, and drop breakup at or above a critical field strength. In chapter 4, we demonstrated that two fluid timescales, the timescale for diffusion of momentum $\tau_m = a^2\rho/\mu$ and the timescale for interfacial charging $\tau_e = \varepsilon\chi$, may yield a nonmonotonic development in the deformation of a weakly conducting drop exposed to a uniform DC electric field. In chapter 5, we extended the theory developed in chapter 4, and demonstrated that modeling the transport of charge towards and along the drop surface is essential to predict the time–dependent field–induced oblate deformation measured in experiments. In chapter 6, we demonstrated that a large fluid interfacial charging timescale τ_e yields fast drop relaxation upon removal of a uniform DC electric field. In chapter 7, we demonstrated that a drop containing a colloidal suspension and varying amounts of surfactant may exhibit radically different field–induced breakup modes depending on the stability of the suspension provided by the added dispersant.

8.1 Impact

If one desires to make use of an electric field to manipulate a low–conductivity drop in a macro– or microscale device for a desired application, it is advantageous to know what conformation the drop will adopt under a certain applied field strength and the timescale under which it will achieve that conformation. Furthermore, it is also useful to be aware of the critical field strength under which the drop will achieve breakup and what shape the drop will acquire during the breakup process. Although there have been numerous publications addressing the steady field–induced deformation of leaky dielectric drops,[21,45–50] our work is the first to consider the effect of surface charge transport on the ability to predict the transient drop deformation and drop relaxation measured in an experiment. Unlike other computational studies,[47,49] our model does not make use of any fitted experimental parameters. If the interfacial charging timescale τ_e and resulting surface charge transport are neglected when predicting the steady oblate (prolate) configuration of a certain experimental system, the theoretical or computational prediction may predict a larger (smaller) drop deformation than that achieved in an experiment. Furthermore, the timescale under which the drop attains its ultimate steady–state deformation will be incorrect, as the dynamics of most low–conductivity systems are dictated by the electrical relaxation timescale τ_e, which is typically on the order of seconds.

As the applied electric field increases, the effects of surface charge transport become more pronounced. At higher field strengths, transient interfacial charging, which we characterized by the Saville number[15] Sa, will yield a longer–lived drop evolution towards steady–state and a quicker drop relaxation towards equilibrium when the field is removed. Surface charge convec-

tion, which we characterized by the electric Reynolds number[14] Re, will yield a more pronounced shock in the surface charge density distribution and resulting interfacial flow profile. Although this form of charge transport has been shown to weaken (strengthen) oblate (prolate) drop deformations,[47,49] thus resulting in larger (smaller) critical field strengths required to achieve drop breakup, we have performed preliminary computations that suggest that charge convection provides a change in the topology of the drop during the breakup process. For prolate drops, we have found surface charge convection to yield tipstreaming at or above a critical electric capillary number Ca. For oblate drops, we expect charge convection to yield drop breakup through equatorial streaming, as observed in the recent experiments performed by the Vlahovska group at Brown University. This is an important finding, as existing theoretical and computational studies capable of quantifying the field–induced response of low–conductivity systems may predict an incorrect drop breakup conformation for a given experiment (e.g. prediction of formation of bulbous ends as opposed to observed tipstreaming). This is a topic currently under investigation.

8.2 Future work

We possess the skills required to advance the field of electrohydrodynamics in a variety of promising directions that would yield a deeper understanding of low–conductivity fluid–fluid systems under electric fields. First, our results from chapter 7 lead our interest to the design of an experimental protocol to assess the stability of a drop containing a colloidal suspension. If one obtains a sample of an oil drop containing an unknown concentration of particles and dispersant, our method would be a quick way to determine whether the suspension is stable or unstable depending on the drop breakup mode achieved

at multiple applied field strengths. We note, however, that this design would require examining a larger parameter space such as additional surfactant concentrations, and different types of colloidal particles and added dispersant. One may also tailor variables such as particle concentration, surfactant concentration, and electric field strength of a given experimental system to obtain a desired drop breakup configuration or to prevent breakup; i.e. for encapsulation of suspensions.

A second area that shows promise is the modeling of the onset of unsteady rotation and three–dimensional flow of oblate drops exposed to high electric fields.[17,18] As stated in chapter 5, there is a critical electric field strength above which an oblate drop will spontaneously rotate in an eventual chaotic fashion.[7] Computationally predicting this onset of drop rotation requires use of a three–dimensional numerical solver for the partial differential governing equations presented in this thesis. Furthermore, a shock–capturing numerical scheme is essential to accurately capture the shocks in the surface charge density profile depicted in chapter 5. Predictions of this critical field strength would help determine conditions under which the drop may or may not spontaneously rotate in a given experiment. Furthermore, the computational predictions would permit an in–depth analysis of chaotic drop rotation and yield potential tailoring of this phenomenon for a desired application, such as fluid mixing.

Lastly, introducing species to the drop interface[6,107] and rendering either of the bulk fluid phases non–Newtonian[108] is a direction the field seems to be gravitating towards. For example, the electric–field–induced response of oil drops containing colloidal particles at the interface has received contin-

ued attention.[6,70,72] Here, the electrohydrodynamic flow sweeps the particles towards the drop surface, where they presumably adsorb. The particles then move along the interface with the direction of the flow, which in turn provides a variety of interesting drop conformations and breakup modes.[70,72] Characterizing the mechanics of these particle–laden interfaces may yield additional insight into the origin of the complex drop dynamics under applied electric fields. We have appropriately characterized the timescales and surface charge transport that yield the field–induced response of a clean fluid interface separating two Newtonian, weakly conducting phases. Thus, additional timescales, such as a surfactant diffusion timescale or a viscoelastic fluid relaxation timescale, may be introduced into the system to examine the additional dynamics that they entail.

Bibliography

[1] S. N. Reznik and E. Zussman. Capillary-dominated electrified jets of a viscous leaky dielectric liquid. *Phys. Rev. E*, 81:026313, 2010.

[2] M. Singh, H. M. Haverinen, P. Dhagat, and G. E. Jabbour. Inkjet printing–process and its applications. *Adv. Mater.*, 22:673–685, 2010.

[3] J. S. Eow, M. Ghadiri, A. O. Sharif, and T. J. Williams. Electrostatic enhancement of coalescence of water droplets in oil: A review of the current understanding. *Chem. Eng. J.*, 84:173–192, 2001.

[4] R. Dimova, N. Bezlyepkina, M. D. Jordö, R. L. Knorr, K. A. Riske, M. Staykova, P. M. Vlahovska, T. Yamamoto, P. Yang, and R. Lipowsky. Vesicles in electric fields: Some novel aspects of membrane behavior. *Soft Matter*, 5:3201–3212, 2009.

[5] S. D. Deshmukh and R. M. Thaokar. Deformation and breakup of a leaky dielectric drop in a quadrupole electric field. *J. Fluid Mech.*, 731:713–733, 2013.

[6] P. Dommersnes, Z. Rozynek, A. Mikkelsen, R. Castberg, K. Kjerstad, K. Hersvik, and J. O. Fossum. Active structuring of colloidal armour on liquid drops. *Nat. Commun.*, 4, 2013.

[7] P. F. Salipante and P. M. Vlahovska. Electrohydrodynamic rotations of a viscous droplet. *Phys. Rev. E*, 88:043003, 2013.

[8] K. P. Sinha, S. Gadkari, and R. M. Thaokar. Electric field induced pearling instability in cylindrical vesicles. *Soft Matter*, 9:7274–7293, 2013.

[9] S. Mhatre, S. Deshmukh, and R. M. Thaokar. Electrocoalescence of a drop pair. *Phys. Fluids*, 27:092106, 2015.

[10] O. Schnitzer and E. Yariv. The Taylor–Melcher leaky dielectric model as a macroscale electrokinetic description. *J. Fluid Mech.*, 773:1–33, 2015.

[11] R. S. Allan and S. G. Mason. Particle behaviour in shear and electric fields. I. Deformation and burst of fluid drops. *Proc. R. Soc. London, Ser. A*, 267:45–61, 1962.

[12] C. T. O'Konski and H. C. Thacher Jr. The distortion of aerosol droplets by an electric field. *J. Phys. Chem.*, 57:955–958, 1953.

[13] G. I. Taylor. Studies in electrohydrodynamics. I. The circulation produced in a drop by electrical field. *Proc. R. Soc. London, Ser. A*, 291:159–166, 1966.

[14] J. R. Melcher and G. I. Taylor. Electrohydrodynamics: A review of the role of interfacial shear stresses. *Annu. Rev. Fluid Mech.*, 1:111–146, 1969.

[15] D. A. Saville. Electrohydrodynamics: The Taylor-Melcher leaky dielectric model. *Annu. Rev. Fluid Mech.*, 29:27–64, 1997.

[16] O. Vizika and D. A. Saville. The electrohydrodynamic deformation of drops suspended in liquids in steady and oscillatory electric fields. *J. Fluid Mech.*, 239:1–21, 1992.

[17] J.-W. Ha and S.-M. Yang. Electrohydrodynamics and electrorotation of a drop with fluid less conductive than that of the ambient fluid. *Phys. Fluids*, 12:764–772, 2000.

[18] P. F. Salipante and P. M. Vlahovska. Electrohydrodynamics of drops in strong uniform dc electric fields. *Phys. Fluids*, 22:112110, 2010.

[19] A. Esmaeeli and P. Sharifi. Transient electrohydrodynamics of a liquid drop. *Phys. Rev. E*, 84:036308, 2011.

[20] H. A Stone. Dynamics of drop deformation and breakup in viscous fluids. *Annu. Rev. Fluid Mech.*, 26:65–102, 1994.

[21] G. Supeene, C. R. Koch, and S. Bhattacharjee. Deformation of a droplet in an electric field: Nonlinear transient response in perfect and leaky dielectric media. *J. Colloid Interface Sci.*, 318:463–476, 2008.

[22] A. Fernández, G. Tryggvason, J. Che, and S. L. Ceccio. The effects of electrostatic forces on the distribution of drops in a channel flow: Two-dimensional oblate drops. *Phys. Fluids*, 17:093302, 2005.

[23] R. J. Haywood, M. Renksizbulut, and G. D. Raithby. Transient deformation of freely-suspended liquid droplets in electrostatic fields. *AIChE J.*, 37:1305–1317, 1991.

[24] H. Paknemat, A. R. Pishevar, and P. Pournaderi. Numerical simulation of drop deformations and breakup modes caused by direct current electric fields. *Phys. Fluids*, 24:102101, 2012.

[25] S. Moriya, K. Adachi, and T. Kotaka. Deformation of droplets suspended in viscous media in an electric field. 1. Rate of deformation. *Langmuir*, 2:155–160, 1986.

[26] T. Nishiwaki, K. Adachi, and T. Kotaka. Deformation of viscous droplets in an electric field: Poly (propylene oxide)/poly (dimethylsiloxane) systems. *Langmuir*, 4:170–175, 1988.

[27] C. Sozou. Electrohydrodynamics of a liquid drop: The time-dependent problem. *Proc. R. Soc. London, Ser. A*, 331:263–272, 1972.

[28] S. Torza, R. G. Cox, and S. G. Mason. Electrohydrodynamic deformation and burst of liquid drops. *Proc. R. Soc. London, Ser. A*, 269:295–319, 1971.

[29] C. Sozou. Electrohydrodynamics of a liquid drop: The development of the flow field. *Proc. R. Soc. London, Ser. A*, 334:343–356, 1973.

[30] X. Xu. *Electrohydrodynamic flow and chaotic mixing inside drops.* PhD thesis, University of California, Santa Barbara, 2007.

[31] J. Zhang, J. D. Zahn, and H. Lin. Transient solution for droplet deformation under electric fields. *Phys. Rev. E*, 87:043008, 2013.

[32] L. G. Leal. *Advanced transport phenomena: Fluid mechanics and convective transport processes.* Cambridge University Press, 2007.

[33] K. J. Hollenbeck. Invlap.m: A Matlab function for numerical inversion of Laplace transforms by the de Hoog algorithm. *Unpublished work*, 1998.

[34] W. B. Russel, D. A. Saville, and W. R. Schowalter. *Colloidal dispersions.* Cambridge University Press, 1992.

[35] H. Sato, N. Kaji, T. Mochizuki, and Y. H. Mori. Behavior of oblately deformed droplets in an immiscible dielectric liquid under a steady and uniform electric field. *Phys. Fluids*, 18:127101, 2006.

[36] X. Chen, S. Mandre, and J. J. Feng. Partial coalescence between a drop and a liquid-liquid interface. *Phys. Fluids*, 18:051705, 2006.

[37] J. Raisin. *Electrocoalescence in water-in-oil emulsions: Towards an efficiency criterion.* PhD thesis, University of Grenoble, 2011.

[38] A. Fernández. Response of an emulsion of leaky dielectric drops immersed in a simple shear flow: Drops less conductive than the suspending fluid. *Phys. Fluids*, 20:043304, 2008.

[39] P. T. Brady, M. Herrmann, and J. M. Lopez. Confined thermocapillary motion of a three-dimensional deformable drop. *Phys. Fluids*, 23:022101, 2011.

[40] R. K. Singh and K. Sarkar. Inertial effects on the dynamics, streamline topology and interfacial stresses due to a drop in shear. *J. Fluid Mech.*, 683:149–171, 2011.

[41] J. M. López-Herrera, P. Riesco-Chueca, and A. M. Gañán-Calvo. Linear stability analysis of axisymmetric perturbations in imperfectly conducting liquid jets. *Phys. Fluids*, 17:034106, 2005.

[42] H. B. Zhang, M. J. Edirisinghe, and S. N. Jayasinghe. Flow behaviour of dielectric liquids in an electric field. *J. Fluid Mech.*, 558:103–111, 2006.

[43] Y. Lu. *Electrohydrodynamic deformation of water drops in oil with an electric field.* PhD thesis, University of Alberta, 2002.

[44] S. A. Orszag and C. M Bender. *Advanced mathematical methods for scientists and engineers I.* McGraw-Hill, 1978.

[45] J. D. Sherwood. Breakup of fluid droplets in electric and magnetic fields. *J. Fluid Mech.*, 188:133–146, 1988.

[46] J. Q. Feng and T. C. Scott. A computational analysis of electrohydrodynamics of a leaky dielectric drop in an electric field. *J. Fluid Mech.*, 311:289–326, 1996.

[47] J. Q. Feng. Electrohydrodynamic behaviour of a drop subjected to a steady uniform electric field at finite electric Reynolds number. *Proc. R. Soc. London, Ser. A*, 455:2245–2269, 1999.

[48] E. Lac and G. M. Homsy. Axisymmetric deformation and stability of a viscous drop in a steady electric field. *J. Fluid Mech.*, 590:239–264, 2007.

[49] A. Fernández. Modeling of electroconvective effects on the interaction between electric fields and low conductive drops. In *ASME 2013 Fluids Engineering Division Summer Meeting*, pages V01CT25A004–V01CT25A004. American Society of Mechanical Engineers, 2013.

[50] Z. Wang, Q. Dong, Y. Zhang, J. Wang, and J. Wen. Numerical study on deformation and interior flow of a droplet suspended in viscous liquid under steady electric fields. *Adv. Mech. Eng.*, 2014:1–12, 2014.

[51] J.-W. Ha and S.-M. Yang. Deformation and breakup of Newtonian and non-Newtonian conducting drops in an electric field. *J. Fluid Mech.*, 405:131–156, 2000.

[52] O. O. Ajayi. A note on Taylor's electrohydrodynamic theory. *Proc. R. Soc. London, Ser. A*, 364:499–507, 1978.

[53] T. Tsukada, T. Katayama, Y. Ito, and M. Hozawa. Theoretical and experimental studies of circulations inside and outside a deformed drop under a uniform electric field. *J. Chem. Eng. Jpn.*, 26:698–703, 1993.

[54] J. Zhang, J. D. Zahn, and H. Lin. Transient solution for droplet deformation under electric fields. *Phys. Rev. E*, 87:043008, 2013.

[55] J. A. Lanauze, L. M. Walker, and A. S. Khair. The influence of inertia and charge relaxation on electrohydrodynamic drop deformation. *Phys. Fluids*, 25:112101, 2013.

[56] M. A. Halim and A. Esmaeeli. Computational studies on the transient electrohydrodynamics of a liquid drop. *FDMP*, 9:435–460, 2013.

[57] D. A. Saville. Electrohydrodynamic stability: Effects of charge relaxation at the interface of a liquid jet. *J. Fluid Mech.*, 48:815–827, 1971.

[58] R. T. Collins, K. Sambath, M. T. Harris, and O. A Basaran. Universal scaling laws for the disintegration of electrified drops. *Proc. Natl. Acad. Sci. USA*, 110:4905–4910, 2013.

[59] J. C. Baygents, N. J. Rivette, and H. A. Stone. Electrohydrodynamic deformation and interaction of drop pairs. *J. Fluid Mech.*, 368:359–375, 1998.

[60] H. A. Stone, J. R. Lister, and M. P. Brenner. Drops with conical ends in electric and magnetic fields. *Proc. R. Soc. London, Ser. A*, 455:329–347, 1999.

[61] C. Pozrikidis. *A practical guide to boundary element methods with the software library BEMLIB.* CRC Press, 2010.

[62] C. Pozrikidis. *Boundary integral and singularity methods for linearized viscous flow.* Cambridge University Press, 1992.

[63] B. A. Yezer, A. S. Khair, P. J. Sides, and D. C. Prieve. Use of electrochemical impedance spectroscopy to determine double-layer capacitance in doped nonpolar liquids. *J. Colloid Interface Sci.*, 449:2–12, 2014.

[64] G. Quincke. Ueber Rotationen im constanten electrischen Felde. *Ann. Phys. (Leipzig)*, 295:417–486, 1896.

[65] T. B. Jones. Quincke rotation of spheres. *IEEE T. Ind. Appl.*, pages 845–849, 1984.

[66] P. M. Vlahovska, R. S. Gracia, S. Aranda-Espinoza, and R. Dimova. Electrohydrodynamic model of vesicle deformation in alternating electric fields. *Biophys. J.*, 96:4789–4803, 2009.

[67] M. M. Sadik, J. Li, J. W. Shan, D. I. Shreiber, and H. Lin. Vesicle deformation and poration under strong DC electric fields. *Phys. Rev. E*, 83:066316, 2011.

[68] J. Seiwert, M. J. Miksis, and P. M. Vlahovska. Stability of biomimetic membranes in DC electric fields. *J. Fluid Mech.*, 706:58–70, 2012.

[69] M. Yu, R. B. Lira, K. A. Riske, R. Dimova, and H. Lin. Ellipsoidal relaxation of deformed vesicles. *Phys. Rev. Lett.*, 115:128303, 2015.

[70] M. Ouriemi and P. M. Vlahovska. Electrohydrodynamics of particle-covered drops. *J. Fluid Mech.*, 751:106–120, 2014.

[71] Z. Rozynek, A. Mikkelsen, P. Dommersnes, and J. O. Fossum. Electroformation of Janus and patchy capsules. *Nat. Commun.*, 5, 2014.

[72] M. Ouriemi and P. M. Vlahovska. Electrohydrodynamic deformation and rotation of a particle-coated drop. *Langmuir*, 2015.

[73] X.-D. Pan and G. H. McKinley. Characteristics of electrorheological responses in an emulsion system. *J. Colloid Interface Sci.*, 195:101–113, 1997.

[74] J.-W. Ha and S.-M. Yang. Rheological responses of oil-in-oil emulsions in an electric field. *J. Rheol.*, 44:235–256, 2000.

[75] P. M. Vlahovska. On the rheology of a dilute emulsion in a uniform electric field. *J. Fluid Mech.*, 670:481–503, 2011.

[76] O. A. Basaran and L. E. Scriven. Axisymmetric shapes and stability of pendant and sessile drops in an electric field. *J. Colloid Interface Sci.*, 140:10–30, 1990.

[77] S. N. Reznik, A. L. Yarin, A. Theron, and E. Zussman. Transient and steady shapes of droplets attached to a surface in a strong electric field. *J. Fluid Mech.*, 516:349–377, 2004.

[78] C. Ferrera, J. M. López-Herrera, M. A. Herrada, J. M. Montanero, and A. J. Acero. Dynamical behavior of electrified pendant drops. *Phys. Fluids*, 25:012104, 2013.

[79] L. T. Corson, C. Tsakonas, B. R. Duffy, N. J. Mottram, I. C. Sage, C. V. Brown, and S. K. Wilson. Deformation of a nearly hemispherical conducting drop due to an electric field: Theory and experiment. *Phys. Fluids*, 26:122106, 2014.

[80] J. A. Lanauze, L. M. Walker, and A. S. Khair. Nonlinear electrohydrodynamics of slightly deformed oblate drops. *J. Fluid Mech.*, 774:245–266, 2015.

[81] H. A Stone, B. J. Bentley, and L. G. Leal. An experimental study of transient effects in the breakup of viscous drops. *J. Fluid Mech.*, 173:131–158, 1986.

[82] H. A. Stone and L. G. Leal. Relaxation and breakup of an initially extended drop in an otherwise quiescent fluid. *J. Fluid Mech.*, 198:399–427, 1989.

[83] H. A. Stone and L. G. Leal. The influence of initial deformation on drop breakup in subcritical time-dependent flows at low Reynolds numbers. *J. Fluid Mech.*, 206:223–263, 1989.

[84] J. R. Lister and H. A. Stone. Capillary breakup of a viscous thread surrounded by another viscous fluid. *Phys. Fluids*, 10:2758–2764, 1998.

[85] O. A. Basaran. Small-scale free surface flows with breakup: Drop formation and emerging applications. *AIChE J.*, 48:1842–1848, 2002.

[86] J.-W. Ha and L. G. Leal. An experimental study of drop deformation and breakup in extensional flow at high capillary number. *Phys. Fluids*, 13:1568–1576, 2001.

[87] Y. Lin, P. Skjetne, and A. Carlson. A phase field model for multiphase electro-hydrodynamic flow. *Int. J. Multiphase Flow*, 45:1–11, 2012.

[88] O. Leon, E. Rogel, G. Torres, and A. Lucas. Electrophoretic mobility and stabilization of asphaltenes in low conductivity media. *Pet. Sci. Technol.*, 18:913–927, 2000.

[89] S. A. Jones, G. P. Martin, and M. B. Brown. Manipulation of beclomethasone–hydrofluoroalkane interactions using biocompatible macromolecules. *J. Pharm. Sci.*, 95:1060–1074, 2006.

[90] B. Comiskey, J. D. Albert, H. Yoshizawa, and J. Jacobson. An electrophoretic ink for all-printed reflective electronic displays. *Nature*, 394:253–255, 1998.

[91] R. J. Pugh, T. Matsunaga, and F. M. Fowkes. The dispersibility and stability of carbon black in media of low dielectric constant. 1. Electrostatic and steric contributions to colloidal stability. *Colloids Surf. A*, 7:183–207, 1983.

[92] M. E. Parent, J. Yang, Y. Jeon, M. F. Toney, Z.-L. Zhou, and D. Henze. Influence of surfactant structure on reverse micelle size and charge for nonpolar electrophoretic inks. *Langmuir*, 27:11845–11851, 2011.

[93] I. D. Morrison. Electrical charges in nonaqueous media. *Colloids Surf. A*, 71:1–37, 1993.

[94] M. F. Hsu, E. R. Dufresne, and D. A. Weitz. Charge stabilization in nonpolar solvents. *Langmuir*, 21:4881–4887, 2005.

[95] S. Poovarodom and J. C. Berg. Effect of particle and surfactant acid–base properties on charging of colloids in apolar media. *J. Colloid Interface Sci.*, 346:370–377, 2010.

[96] M. M. Gacek and J. C. Berg. Investigation of surfactant mediated acid–base charging of mineral oxide particles dispersed in apolar systems. *Langmuir*, 28:17841–17845, 2012.

[97] S.-R. Yeh, M. Seul, and B. I. Shraiman. Assembly of ordered colloidal aggregrates by electric-field-induced fluid flow. *Nature*, 386:57–59, 1997.

[98] P. J. Sides. Electrohydrodynamic particle aggregation on an electrode driven by an alternating electric field normal to it. *Langmuir*, 17:5791–5800, 2001.

[99] W. D. Ristenpart, I. A. Aksay, and D. A. Saville. Assembly of colloidal aggregates by electrohydrodynamic flow: Kinetic experiments and scaling analysis. *Phys. Rev. E*, 69:021405, 2004.

[100] V. Oles. Shear-induced aggregation and breakup of polystyrene latex particles. *J. Colloid Interface Sci.*, 154:351–358, 1992.

[101] T. Serra, J. Colomer, and X. Casamitjana. Aggregation and breakup of particles in a shear flow. *J. Colloid Interface Sci.*, 187:466–473, 1997.

[102] V. A. Tolpekin, M. H. G. Duits, D. Van den Ende, and J. Mellema. Aggregation and breakup of colloidal particle aggregates in shear flow, studied with video microscopy. *Langmuir*, 20:2614–2627, 2004.

[103] A. H. L. West, J. R. Melrose, and R. C. Ball. Computer simulations of the breakup of colloid aggregates. *Phys. Rev. E*, 49:4237, 1994.

[104] K. Higashitani and K. Iimura. Two-dimensional simulation of the breakup process of aggregates in shear and elongational flows. *J. Colloid Interface Sci.*, 204:320–327, 1998.

[105] A. Zaccone, M. Soos, M. Lattuada, H. Wu, M. U. Bäbler, and M. Morbidelli. Breakup of dense colloidal aggregates under hydrodynamic stresses. *Phys. Rev. E*, 79:061401, 2009.

[106] P. Calvert. Inkjet printing for materials and devices. *Chem. Mater.*, 13:3299–3305, 2001.

[107] H. Nganguia, Y.-N. Young, P. M. Vlahovska, J. Blawzdziewicz, J. Zhang, and H. Lin. Equilibrium electro-deformation of a surfactant-laden viscous drop. *Phys. Fluids*, 25:092106, 2013.

[108] N. C. Lima and M. A. dÁvila. Numerical simulation of electrohydrodynamic flows of Newtonian and viscoelastic droplets. *J. Non-Newton. Fluid Mech.*, 213:1–14, 2014.